Jet Energy Scale Studies and the Search for the Standard Model Higgs Boson in the Channel $ZH \rightarrow \nu\bar{\nu}b\bar{b}$ at DØ

Lydia Mary Isis Lobo
Imperial College London

A thesis submitted in fulfilment of
the requirements for the degree of
Doctor of Philosophy
of the University of London
and the Diploma of Imperial College

November 2006

Jet Energy Scale Studies and the Search for the
Standard Model Higgs Boson in the
Channel $ZH \rightarrow \nu\bar{\nu}b\bar{b}$ at DØ

Lydia Mary Isis Lobo
Imperial College London
November 2006

ABSTRACT

The DØ experiment is based at the Tevatron, which is currently the world's highest-energy accelerator. The detector comprises three major subsystems: the tracking system, the calorimeter and the muon detector. Jets, seen in the calorimeter, are the most common product of the proton-proton interactions at 2TeV. This thesis is divided into two parts. The first part focuses on jets and describes the derivation of a jet energy scale using $p\overline{p} \rightarrow$(Z + jets) events as a cross-check of the official DØ jet energy scale (Versions 4.2 and 5.1) which is derived using $p\overline{p} \rightarrow \gamma$+jets events. Closure tests were also carried out on the jet energy calibration as a further verification. Jets from b-quarks are commonly produced at DØ, readily identified and are a useful physics tool. These require a special correction in the case where the b-jet decays via a muon and a neutrino. Thus a semileptonic correction was also derived as an addition to the standard energy correction for jets.

The search for the Higgs boson is one of the largest physics programmes at DØ. The second part of this thesis describes a search for the Standard Model Higgs boson in the $ZH \rightarrow \nu\bar{\nu}b\bar{b}$ channel in $52fb^{-1}$ of data. The analysis is based on a sequence of event selection criteria optimised on Monte Carlo event samples that simulate four light Higgs boson masses between 105 GeV and 135GeV and the main backgrounds. For the first time, the data for the analysis are selected using new acoplanarity triggers and the b-quark jets are selected using the DØ neural net b-jet tagging tool. A limit is set for $\sigma(p\bar{p} \rightarrow ZH) \times Br(H \rightarrow b\bar{b})$.

Acknowledgements

> *"Sometimes our light goes out but is blown into flame by another human being. Each of us owes deepest thanks to those who have rekindled this light."* Albert Schweitzer

Life is most interesting, retrospectively, when things don't work or you make mistakes. This journey to completing my thesis has been difficult, tiring, enlightening and rewarding. When I started, I assumed that I was here to learn all about high energy physics and scientific writing. I didn't realise then how much more important would be all the other things I learnt from the people I have been lucky enough to meet and to work with. I know now that a PhD is not just about doing a few years work and then writing it all down. It's about developing an instinct for when things aren't as they seem, learning to ask the right questions and realising that there are no silly questions, and motivating oneself to persist when things are at their most frustrating.

Although I now leave behind science as my daily activity, I will always be a physicist in mind with an immutable scientific disposition. In my heart, I hold dear the many happy memories of the people I've encountered, and feel an enormous sense of gratitude for their help, support and wisdom. Most importantly, I would like to thank Gavin Davies, my supervisor, for his practical guidance, seemingly unlimited patience, and unwavering support. Gavin, you have been a better supervisor than I could ever have hoped for and I have learned more than physics, through

observing your leadership of the DØ Group at Imperial. I would also like to thank Rachel Padman for her fantastic support as my Director of Studies throughout my undergraduate years. I have been incredibly lucky to have had you both as mentors. Thanks also to Trevor Bacon for reading my thesis so meticulously.

My deepest thanks go to my mother and father and to David, who have supported me in every way possible for so long: feeding, watering and sheltering me, providing endless encouragement, showing boundless faith in my abilities and for reading my thesis. I'd also like to thank Grandma, Grandpa and Nana, my grandparents, no longer with us, and my Aunt Moira, for their continuous support throughout my studies.

At Imperial, many thanks must firstly go to Michele Petteni and Tim Scanlon for all their practical help and patience in answering my questions. Without Ray Beuslinck, Kostas Georgiou and Bill Cameron to solve so willingly my frequent computer problems, I wonder if I would have made it through the past few years! At Fermilab too, I had the pleasure to work with some very dedicated people and I'd like to thank Ia Iashvilli for her help and guidance with my work on the jet energy scale, Anna Goussiou for her help with the Jet Energy Scale and eflow, and Jon Hays for his guidance on eflow. I would also like to thank Daniela Bauer, Claus Buzello, Philip Perea, and Amber Jenkins for their ready help whenever I asked. Also, thanks to Paula Brown for her ready smile, advice and help.

Thanks must also go to PPARC for their studentship grant and the Imperial HEP group for the opportunity to be part of the group; together these have enabled me to work in London and Chicago on an international experiment and to meet people from so many different backgrounds.

At both Fermilab and Imperial I have made many friends of whom I have countless fond memories. I will miss the teatime banter in the trailers with often six or more nationalities made all the more amusing by cultural communication differences. Help and a welcome reminder of the UK was always forthcoming from the fermifogies lot: Tamsin, Emily, Anant, Martin G, Dustin, Paul, Matt, James, Ben, Simon, Stephen, Kyle, Nicola, Gavin, Tim, Phil, Amber, Philip and Satish (honorary members). Anatoly, Robert, Raymond and Sarosh, thanks for the trips to Panera, broadening my film appreciation and the extensive commentary on American culture. I will always smile when I think of my house and office mates Amber and Alex - thank you for the calm and making Fermilab feel like home. My time in London would not have been the same without the Imperial bunch. Special thanks to Lisa and Helen H. for all their tea and pearls of PhD wisdom that helped during the more difficult parts. I would also like to thank my old friends, Alex, Bee, Ruth, Lucy, Laura, Debjani, Nick HJ, Nasrin and Michelle - you've known me most of my life, thanks for all your support, advice and cheeriness when the frustrations seemed never-ending. There are many more I'd like to include, but there isn't space, you know who you are - thank you to you too. I wish you all luck, health and happiness in your future endeavours.

Contents

List of Figures

List of Tables

Preface

This thesis describes work that was performed on the DØ experiment from December 2002 to July 2006. This work concentrates on studies carried out on the jet energy calibration of the calorimeter, the derivation of a jet energy correction for b-quark jets, the derivation of an electromagnetic calibration as part of the development of a DØ energy flow algorithm and a search for the Standard Model Higgs boson in the $ZH \rightarrow \nu\bar{\nu}b\bar{b}$ channel.

First, I made significant contributions to DØ as a member of the Jet Energy Scale group. I used $p\overline{p} \rightarrow Z(e\bar{e}) + jets$ events to validate the main jet energy calibration that is used by all the experiment and derived using $p\overline{p} \rightarrow \gamma + jets$ events. This involved deriving a jet energy response using Z+jets events and performing closure tests on these events using the (γ + jets) jet energy scale. The initial code to derive the response was based on code written by an Imperial College PPARC Fellow, Michele Petteni, and was developed to be used with version p14 of the DØ software. This was the first time that DØ had sufficient (Z + jets) data events that it was possible to carry out an independent cross-check of such a fundamental, widely-used calibration. The cross-checks and closure tests that I performed contributed to the release of versions 4.2 and 5.1 of the jet energy scale calibration.

Secondly, as part of the jet energy scale group, I derived a correction specifically for b-quark jets containing a neutrino and a muon from the decay of the b-quark, a *semileptonic* correction. B-quark physics is one of the major efforts of the DØ Collaboration and b-quarks are observed as jets in the calorimeter with particular characteristics. Since, in these decays, the neutrino escapes the detector leaving no trace, and the muon is difficult to detect, I derived scalar and vector corrections to compensate for this. The scalar correction formed part of versions 5.1 and 5.3 of the jet energy scale correction.

Thirdly, my next focus was on deriving a low-energy calibration for the electromagnetic (EM) calorimeter as part of the energy flow group. To improve the measurement of low energy particles, DØ developed an algorithm to combine measurements in the tracking system, which are more accurate at low-momentum, and energy measurements in the calorimeter. My study formed a necessary step in the development of the energy flow algorithm.

Lastly, as part of the Higgs physics group, I undertook a search for the Standard Model Higgs in the $ZH \rightarrow \nu\bar{\nu}b\bar{b}$ channel using, for the first time, data taken with the v13 trigger list that included triggers that select on the topography of events in this channel. My analysis built on the early analysis of this channel using v12 data by Makoto Tomoto. My study, carried out in collaboration with an Michele Petteni, used advanced techniques to optimise this cuts-based analysis including the first use of the DØ neural net b-tagging tool developed by Tim Scanlon and Miruna Anastasoaie.

The thesis is structured as follows:

- Chapter 1 gives a concise account of the Standard Model with a focus on the relevant areas of Higgs physics;
- Chapter 2 outlines the workings of the Tevatron, the Fermilab proton-antiproton accelerator, and the DØ detector setup;
- Chapter 3 describes the jet energy response derived using (Z + jets) events, compares it to the equivalent (γ + jets) response and evaluates closure tests carried out on (Z + jets) events using the (γ + jets) jet energy correction;
- Chapter 4 gives a description of the derivation of the muonic semileptonic correction to b-quark jets and details the EM calibration that was calculated as a component of the development of the energy flow algorithm;
- Chapter 5 details the search for the Standard Model Higgs boson using Run II data taken using trigger list version 13 at DØ. This includes the process

for selecting candidate events, background simulation and estimation, and the optimisation of this selection procedure including the use of the neural net b-tagging tool. The results of this analysis are evaluated and discussed;

- Chapter 6 concludes with a summary and considers the future.

Chapter 1

The Standard Model and the Higgs Boson

1.1 Introduction

From before Democritus first suggested that matter is made of indivisible particles or *atoms* [11] in the fourth century B.C, natural philosophers have been searching for a theory that describes how the matter around us is structured and how it interacts. It was only in the 20th century, when both the mathematical and technological tools became available, that it was possible to start to probe deep inside the atom, eventually revealing the structure of the matter particles (fermions), and the force particles (bosons) that mediate the interactions. The *Standard Model* (SM), for the most part, successfully describes the fundamental particles in terms of an SU(3)×SU(2)×U(1) gauge theory and has been precisely tested. This chapter briefly describes the Standard Model and the symmetries upon which it is based, with a focus on electroweak theory and the Higgs mechanism.

1.2 The Standard Model

1.3 Matter and its Interactions

Particle families The Universe, at the most basic level that it is currently understood, is made up of three ‘generations’ or ‘families’ of particles called fermions which can be subdivided into quarks and leptons. Everyday matter is made from the lightest generation which includes the electron, and the up and down quarks that make up the protons and neutrons in nuclei. This first generation also includes electron neutrinos which are constantly travelling through us, coming mostly from fusion reactions within the Sun. Each particle within this first generation has its own distinct properties. There are two heavier ’generations’ which contain particles in patterns identical to those of the first generation in all ways but their masses. These are not observed in everyday matter, as they are unstable and so are only produced in high-energy environments like the Tevatron accelerator, surviving for only short periods of time after they are created. Some of the properties[1] of these three generations of matter particles are given in Table 1.1.

Leptons (spin = 1/2)			**Quarks** (spin = 1/2)		
Flavour	Mass GeV/c^2	Electric Charge	Flavour	Approx. Mass GeV/c^2	Electric Charge
ν_e electron neutrino	$<1\times10^{-8}$	0	**u** up	0.003	2/3
e electron	0.000511	-1	**d** down	0.006	-1/3
ν_μ muon neutrino	<0.0002	0	**c** charm	1.3	2/3
μ muon	0.106	-1	**s** strange	0.1	-1/3
ν_τ electron neutrino	<0.02	0	**t** top	175	2/3
τ electron	1.7771	-1	**b** bottom	4.3	-1/3

Table 1.1: Summary of some of the properties of the three generations of matter particles. [8]

---

[1] The quark masses quoted here are the ‘bare’ or ‘current’ masses. The ‘constituent’ or ‘effective’ masses are heavier, for example the u-quark is about 0.3 GeV/C^2. Both are model-dependent

Particle Interactions These three generations of particles interact via the four forces, which correspond to the exchange of force carrying bosons: the *electromagnetic* force affects all charged particles, the *strong* binds nuclei together, the *weak* force is responsible for some nuclear reactions like β-decay and the *gravitational* force. The gravitational force is very weak compared to the other three forces, and has a negligible effect in particle physics. All these particles and their interactions, except for gravity, are described in the Standard Model (SM), a good description of which may be found in many well-respected reviews such as [12] and [13]. Table 1.2 describes some of the properties of these forces.

Property	Gravitational	Weak	Electromagnetic	Strong
		(Electroweak)		
Acts on	Mass - Energy	Weak Isospin	Electric Charge	Colour Charge
Particles Experiencing	All	Quarks Leptons	Electrically charged	Quarks Gluons
Particles Mediating	Graviton	W^+,W^-, Z^0	photon (γ)	Gluons
Strength relative to Electromagnetic force	10^{-41}	0.8	1	25

Table 1.2: Summary of some of the properties of the force-mediating particles of the Standard Model. [8]

1.4 Gauge Theories

Symmetries in nature often conceal fascinating fundamental ideas about physics that may be described mathematically, that may be used to classify shapes, patterns and other phenomena. An important area of mathematics, group theory[2], can describe the transformations under which an object is symmetric. Symmetries in physics have important physical consequences summarised in Noether's theorem [14]:

---

[2] A group is a set of objects that is closed, associative, has an identity element and every element has an inverse. The U(1) group is a group of all 1×1 unitary matrices.

"For any continuous symmetry exhibited by a physical law, there is a corresponding continuous observable quantity that is conserved."

The SM is a quantum field theory, described by a *Lagrangian* comprising terms composed of fermion and boson fields. The Lagrangian is invariant under certain transformations, called *gauge transformations* which may be simply thought of as rotations. When a gauge transformation is identically performed at every space-time point and the Lagrangian remains unchanged then it is said to be globally invariant. However, gauge theory is based upon the idea that the Lagrangian is also invariant under local transformations[3]. The gauge theory class of mathematics was developed in 1954 by Yang and Mills [15] and it is this type of mathematics that forms the basis of the Standard Model, providing a framework with which to describe the quantum field theories of the strong, weak and electromagnetic forces.

The idea of gauge invariance of the SM Lagrangian may be most easily understood by first considering a simple global gauge transformation applied to the Dirac Lagrangian, $\mathcal{L}$, which describes free fermion fields:

$$\mathcal{L}_D = \bar{\Psi}(i\gamma^{\mu}\partial_{\mu} - m)\Psi \tag{1.1}$$

where Ψ and $\bar{\Psi}$ are the fermion field and its conjugate respectively, γ^{μ} are the 4×4 gamma matrices and m is the fermion mass. If we now transform the field with the global gauge transformation[4], $\Psi \to e^{-i\omega}\Psi$, $\bar{\Psi} \to e^{i\omega}\bar{\Psi}$, where ω is real and constant and $e^{-i\omega}$ is the U(1) group, then $\mathcal{L}_D$ remains unchanged. This particular manifest invariance can be observed in current conservation or the conservation of electric charge.

The Yang-Mills gauge theory extended this idea of a global symmetry by requiring that Lagrangians must also possess local symmetries. A global transformation means that all points in space-time (x) know about the transformation instantly and it does not take into account that the signal requires time to travel. A more 'realistic' requirement, that also leads to more interesting physics, is to require that gauge

---

[3] A local transformation is a symmetry that could be defined arbitrarily from one position to the next and is dependent on space-time coordinates.

[4] It is called a global transformation because it is not dependent on space-time coordinates.

invariance really is a basic property of nature so requiring that the Lagrangian is invariant under local transformations. This means that the transformation depends on the space-time point and is now written as $\Psi \rightarrow \Psi' = e^{iq\omega(x)}\Psi(x)$. Substituting this into 1.1 leads to an extra term, $\delta\mathcal{L}$ in the Lagrangian :

$$\delta\mathcal{L} = \bar{\Psi}(x)\gamma^{\mu}[\partial_{\mu}\omega(x)]\omega(x)\Psi(x) \tag{1.2}$$

This must be compensated for if the Lagrangian is to be unchanged. In this case, this is done by introducing the electromagnetic force in the form of a real vector gauge field, A_μ, to represent photons with which the fermion field can interact. A_μ transforms as:

$$A_{\mu} \rightarrow A_{\mu}^{'} = A_{\mu} + \frac{1}{e}\partial_{\mu}\omega(x) \tag{1.3}$$

and the term $e\bar{\Psi}\gamma^{\mu}A_{\mu}\Psi$ represents the interactions of the gauge field with the fermion field. The Lagrangian becomes:

$$\mathcal{L} = \bar{\Psi}(i\gamma^{\mu}(\partial_{\mu} + ieA_{\mu}) - m)\Psi \tag{1.4}$$

where e is the fermion charge. We need to include a kinetic energy (K.E.) term for the photon field, which itself must be invariant. So we use the K.E. term:

$$-\frac{1}{4}F_{\mu\nu}F^{\mu\nu} \tag{1.5}$$

where $F_{\mu\nu} = [J_{\mu}A_{\nu}] - [J_{\nu}A_{\mu}]$. Thus we arrive at the Lagrangian density for quantum electrodynamics, QED:

$$\mathcal{L} = -\frac{1}{4}F_{\mu\nu}F^{\mu\nu} + \bar{\Psi}(i\gamma^{\mu}(\partial_{\mu} + ieA_{\mu}) - m)\Psi \tag{1.6}$$

It is not possible to add any mass terms of the form $M^2A_{\mu}A^{\mu}$ as is not gauge invariant. At this point, it is convenient to group the partial derivative and the term explicitly containing the gauge field to define the *covariant derivative*, D_μ:

$$D_{\mu} \equiv \partial_{\mu} + ieA_{\mu} \tag{1.7}$$

so that 1.6 becomes:

$$\mathcal{L}_{\mathcal{QED}} = -\frac{1}{4}F_{\mu\nu}F^{\mu\nu} + \bar{\Psi}(i\gamma^{\mu}D_{\mu} - m)\Psi \tag{1.8}$$

It is this covariant derivative that groups together the interesting terms that describe the interactions of the particle fields and gauge fields, this becoming more apparent when we generalise this idea of symmetry in the next section. The covariant derivative has the property that it transforms in the same way as the particle fields under gauge transformations. Furthermore, the field strength tensor may be expressed in terms of D$_\mu$,

$$F_{\mu\nu} = -\frac{i}{g}[D_\mu, D_\nu] \tag{1.9}$$

where g is the coupling constant which determines the strength of an interaction. In the case of the U(1) symmetry that represents QED, $g = e$, the electronic charge. So, the whole Lagrangian density has been derived from the requirements of local gauge invariance of the U(I) gauge symmetry and the requirements of QFT.

1.4.1 Non-Abelian Gauge Transformations

In a similar fashion to the U(1) symmetry described in the previous section, gauge transformations may be applied to the SU(2) symmetry group which describes the weak force, and the SU(3) group of QCD. A Lagrangian may be constructed for a general gauge theory by considering the arbitrary transformation, SU(n), represented by the matrices $e^{-\omega^a \mathbf{T}^a}$ where there are n^2-1 gauge fields that interact with the particles (unlike the singlets in the U(1) transformation) that transform as follows:

$$\Psi_i \rightarrow \Psi_i' = (e^{-i\omega^a}\mathbf{T}^a)_i^j \Psi_j \tag{1.10}$$

Substituting the transformation in Equation 1.10 into the appropriate Lagrangian, as before, leads to extra terms. As in the Abelian case, these must again be compensated for by the addition of vector gauge fields, W$^a_\mu$. So the covariant derivative becomes:

$$\mathbf{D}_\mu = (\partial_\mu \mathbf{I} + ig\mathbf{T}^a W^a_\mu) \tag{1.11}$$

where $\mathbf{I}$ are the unit matrices of order n. The Lagrangian becomes, after adding in the K.E. term, as before:

$$\mathcal{L} = \bar{\Psi}^i (i\gamma^\mu \mathbf{D}_\mu - m\mathbf{I})_i^j \Psi_j - \frac{1}{4} F^a_{\mu\nu} F_a^{\mu\nu} \tag{1.12}$$

Similarly, the K.E. term is still constructed from the field strengths $F^a_{\mu\nu}$ as in Equation 1.9, but $\mathrm{F}_{\mu\nu}$ is in a more complex form since the generators of the group do not all commute:

$$F^a_{\mu\nu} = \partial_\nu A^a_\mu - \partial_\mu A^a_\nu - g f^{abc} A^b_\nu A^c_\nu \tag{1.13}$$

The last term here, when substituted into the Lagrangian, leads to terms such as $g f^{abc}(\partial_\mu A^a_\nu) A^b_\mu A^c_\nu$ and $\frac{1}{4} g^2 (f^{abc} f^{abe} A^b_\mu) A^c_\nu A^d_\mu A^e_\nu$ which arise because of the properties of non-Abelian transformations and imply that these gauge bosons interact with each other. As before, a mass term is still forbidden as it is not gauge invariant. In the case of the SU(2) weak force, this leads to weak isospin doublets of particles, and three vector gauge bosons. Weak isospin is the equivalent of electric charge for the weak force; see section 1.5 for more details. For the strong force with its SU(3) symmetry, there are then eight gauge bosons (gluons) with six colour triplets of the quarks, where colour is the QCD equivalent of the electric charge in QED.

1.5 Electroweak Theory

Problems with the separate SU(2) and U(1) descriptions of the weak and electromagnetic (EM) forces led Glashow, Weinberg and Salam (GSW) to propose independently between 1961 and 1967 a theory that unified these interactions into one *electroweak* theory [16], [17], [18]. This unification was suggested before the W and Z bosons had been discovered, and their theory successfully predicted the existence of the neutral weak current involving the Z^0 boson. GSW had noted the similarities of the weak charged current and EM interactions, and that weak interactions only involve the left-handed particles. They proposed a theory of $\mathrm{SU}(2)_L \otimes \mathrm{U}(1)_Y$ symmetry which interacts with the left-handed and right-handed components of the fermion fields separately.

The weak interaction is described by the $\mathrm{SU}(2)_L$ symmetry with gauge bosons W^a_μ (a=1,2,3), which lead to two charged bosons and one neutral one. However, from experimental observations such as charged pion decay, we know that the coupling strengths of weak interactions are different for left-handed and right-handed particles. In fact, the charged bosons only couple to left-handed fermions and right-handed anti-fermions, and no right-handed neutrinos have been observed. So the fermion field, Ψ, is split into its left and right-handed components, $\Psi = \psi_L + \psi_R$, so that each may be treated separately. The fermion field is now made up of left-handed weak isospin doublets, ψ_L^i, whose weak 'charge', *isospin*, takes the value T=1/2, using the notation of the previous section and the right-handed fermions are isosinglets, ψ_R^i, with T=0:

$$\psi_L^i = \begin{pmatrix} \nu_e \\ e \end{pmatrix}_L ; \begin{pmatrix} \nu_\mu \\ \mu \end{pmatrix}_L ; \begin{pmatrix} \nu_\tau \\ \tau \end{pmatrix}_L ; \begin{pmatrix} u \\ d \end{pmatrix}_L ; \begin{pmatrix} c \\ s \end{pmatrix}_L ; \begin{pmatrix} t \\ b \end{pmatrix}_L \tag{1.14}$$

$$\psi_R^i = \ e_R \ ; \ \mu_R \ ; \ \tau_R \ ; \ u_R \ ; \ d_R \ ; \ c_R \ ; \ s_R ; \ t_R \ ; b_R \tag{1.15}$$

T is the weak equivalent to the EM charge, so that when T=0, there is no weak interaction. No right-handed neutrinos are needed in this model. Recent results show that neutrinos oscillate [19], [20], implying a non-zero neutrino mass. Extensions to the SM, including right-handed neutrinos have been postulated [21]. The U(1) symmetry of the EM interactions is included indirectly by adding a field, B_μ with a $U(1)_Y$ symmetry to the weak Lagrangian where the generator, **Y**, is not the electric charge but hypercharge. The B_μ field will interact with both the left-handed and right-handed quarks and leptons. This then mixes with the W^0 field to form the Z^μ and A^μ fields. The fermion doublets are assigned a hypercharge, Y=-1 and the singlets, Y=-2. Taking the two symmetries together, left-handed components transform as:

$$\psi_L \rightarrow \psi_L' = e^{i\alpha(x).\mathbf{T}+i\beta(x)\mathbf{Y}}\psi_L \tag{1.16}$$

and the right-handed components transform as

$$\psi_R \rightarrow \psi_R' = e^{i\beta(x)\mathbf{Y}}\psi_R \tag{1.17}$$

The interaction terms in the Lagrangian become:

$$\mathcal{L}_{interaction} = \psi^i(i\gamma^\mu\underbrace{(\partial_\mu\mathbf{I} + ig\mathbf{T}^a W_\mu^a + i'\frac{\mathbf{Y}}{2}B_\mu)}_{\text{covariant derivative, } \mathbf{D}_\mu})_i^j\Psi_j \tag{1.18}$$

The EM interaction is hidden in this Lagrangian as a mixing between W_μ^3 and B_μ that leads to the physically identifiable Z^0 and γ bosons via the weak mixing angle,

θ_W. In understanding this mixing, a third quantum number, the third component of the weak isospin, T^3, is used where the T=$\frac{1}{2}$ doublets have T^3=+$\frac{1}{2}$ for the more positive particle in the doublet, and T^3=$-\frac{1}{2}$ for the more negative particle. The right-handed singlets have T^3=0.

$$A^\mu = B^\mu \cos\theta_W + W^{\mu,3}\sin\theta_W \tag{1.19}$$

$$Z^\mu = -B^\mu \sin\theta_W + W^{\mu,3}\cos\theta_W \tag{1.20}$$

The W$^1_\mu$ and W$^2_\mu$ fields and their generators are also mixed to form the observed W$^\pm$ bosons:

$$W^\pm_\mu = \frac{1}{\sqrt{2}}(W^1_\mu \pm iW^2_\mu) \quad \text{and} \quad \mathbf{T}^\pm_\mu = \frac{1}{\sqrt{2}}(\mathbf{T}^1_\mu \mp i\mathbf{T}^2_\mu) \tag{1.21}$$

Substituting the inverses of Equations 1.19, 1.20 and 1.21 into the electroweak Lagrangian, and leaving out the K.E. terms to focus on the interaction terms, after grouping the W$^\pm$, A$_\mu$ and Z$_\mu$ fields, the interaction Lagrangian becomes:

$$\mathcal{L}_{interaction} = \bar{\Psi}\gamma^\mu g(\mathbf{T}^+_\mu W_\mu + \mathbf{T}^-_\mu W_\mu)\Psi \tag{1.22}$$

$$+ \bar{\Psi}\gamma^\mu(g\mathbf{T}^3\cos\theta_W - g'\frac{\mathbf{Y}}{2}\sin\theta_W)Z_\mu\Psi \tag{1.23}$$

$$+ \bar{\Psi}\gamma^\mu(g\mathbf{T}^3\sin\theta_W - g'\frac{\mathbf{Y}}{2}\cos\theta_W)A_\mu\Psi \tag{1.24}$$

The charged current weak interactions are described by the first term and only involve the left-handed components of Ψ since T=0 for the right-handed components. The second term describes the observed weak neutral currents that may involve either the right-handed or the left-handed particles. This term may be expanded to show this explicitly:

$$\bar{\psi}_L\gamma\mu(g\mathbf{T}^3\cos\theta_W - g'\frac{\mathbf{Y}}{2}\sin\theta_W)Z_\mu\psi_L + \bar{\psi}_R\gamma^\mu g'\frac{\mathbf{Y}}{2}\sin\theta_W Z_\mu\psi_R \tag{1.25}$$

The third term describes the EM interactions and the generator of the U(1)$_{EM}$ symmetry, **Q**, may be identified as **Q**=**T**^{3} + $\frac{\mathbf{Y}}{2}$. The EM interaction term is of the form $\bar{\Psi}e\gamma^\mu A_\mu\Psi$ as identified in the QED Lagrangian in Equation 1.6. Comparing this to the last term allows the constraint

$$g\sin\theta_W = g'\cos\theta_W = e \tag{1.26}$$

to be placed on g,g' and θ_W.

There is, however, a key problem in that the $\mathrm{SU}(2)_L \otimes \mathrm{U}(1)_Y$ symmetry, in itself, does not explain why the two neutral gauge fields, W^3_μ and B_μ, mix or indeed why the $\mathrm{W}^\pm$ and Z^0 bosons have mass but the photon remains massless. Neither does it explain how the fermions acquire mass. Earlier, it was mass terms of the form $\mathrm{m}^2\mathrm{W}_\mu\mathrm{W}^\mu$ that were not allowed in the Lagrangian as they are not gauge-invariant, but now mass terms of the fermion fields of the form $\mathrm{m}\bar{\Psi}\Psi$ cannot be included either. These mix the left-handed and right-handed states which undergo different gauge transformations as in Equations 1.16 and 1.17, so the resultant mass term is no longer invariant.

1.6 The Higgs Mechanism

The Higgs mechanism spontaneously breaks the electroweak symmetry down to a U(1) symmetry, introducing the masses of the W and Z bosons, while allowing the photon to remain massless [22], [23]. It allows the Lagrangian to remain invariant under the U(1) symmetry group, but the vacuum state is not and has a non-zero vacuum expectation value. The Higgs field is itself gauge invariant, and an expansion around its vacuum expectation value produces the couplings to the gauge boson and fermion fields (*Yukawa couplings*). In this way, mass terms for the gauge fields, the gauge bosons and even for the Higgs field itself appear. The mechanism then predicts the existence of the Higgs boson and all of its properties except its mass; to date the Higgs boson has not been observed.

Considering the simplest case of an Abelian U(1) gauge theory with a scalar field, Φ, and the addition of a scalar potential $V(\Phi)$, the Lagrangian may be written as:

$$\mathcal{L} = (D_\mu\Phi)^*(D^\mu\Phi) - \frac{1}{4}F_{\mu\nu}F^{\mu\nu} - V(\Phi) \tag{1.27}$$

where $D_\mu \equiv \partial_\mu + ieA_\mu$. The potential $V(\Phi)$ is given by

$$V(\Phi) = \mu^2\Phi^*\Phi + \lambda|\Phi^*\Phi|^2 \tag{1.28}$$

and can be likened to the $\mathcal{U}$ term for potential energy in the classical Lagrangian $\mathcal{L} = \mathcal{T} - \mathcal{U}$. As long as $V(\Phi)$ is composed of terms of the form $\Phi^*\Phi$ then the

Lagrangian will remain gauge invariant under the U(1) transformation $\Phi \rightarrow e^{-i\omega(x)}\Phi$ and the form of V chosen here is the minimum required to retain the gauge symmetry such that the theory remains renormalisable. Assuming $\lambda > 0$, we will consider the two cases where μ^2 is greater than or less than zero. For $\mu^2 > 0$, the potential V has the shape shown on the left in Figure 1.1; however, for $\mu^2 < 0$, the potential takes on the form on the right in Figure 1.1. In the latter case, the system is not in its ground state at $\Phi = 0$, but has a vacuum expectation value, $v = \sqrt{\mu^2/\lambda}$. The ground state is now at $\Phi = e^{i\theta}v/\sqrt{2}$ where θ can take any value from 0 to 2π. This means that there are infinitely many ground states and the system is still symmetric. The spontaneous symmetry breaking occurs when a choice is made as to which θ represents the true vacuum. Once this decision has been taken, the symmetry is broken. Expanding Φ around its expectation value gives

$$\Phi(x) = \frac{1}{\sqrt{2}}(v + \mathrm{H} + i\phi) = \frac{1}{\sqrt{2}}(v + \mathrm{h})e^{i\frac{\theta(x)}{v}} \tag{1.29}$$

where h will correspond to the physical Higgs field. It is possible to choose the U(1) gauge transformation so that ϕ disappears:

$$A_\mu \rightarrow A_\mu + \frac{1}{ev}\partial_\mu\theta \tag{1.30}$$

and this is called the Unitarity gauge. Substituting Equation 1.29 into 1.28 gives:

$$V(\Phi) = \mu^2H^2 + \mu\sqrt{\lambda}H^2 + \frac{\lambda}{4}(H^4 + 2H^2) + \frac{\mu^4}{4\lambda} \tag{1.31}$$

Then substituting 1.31 into 1.27 leads to:

$$\mathcal{L} = \frac{1}{2}(\partial_\mu h)^2 + \mu^2h^2 + \frac{1}{2}e^2v^2A_\mu^2 + \frac{\mu^4}{4\lambda} - \lambda vh^3 - \frac{\lambda}{4}h^4 + \frac{1}{2}e^2A_\mu^2h - \frac{1}{4}F_{\mu\nu}F^{\mu\nu} \tag{1.32}$$

From this, a scalar field, h, of mass $\sqrt{-2\mu^2}$ and a vector field (A_μ) of mass ev, may be identified. There are also interaction terms which describe the three and four-point interactions of the Higgs field with the vector field ('hhh', '$hhhh$', '$AAhh$' and 'AAh'). There is also the kinetic energy term as seen before. This is the Higgs mechanism and h is the Higgs boson. In this case, used as a simple example of the Higgs mechanism, a mass has been introduced for the photon but gauge invariance is preserved.

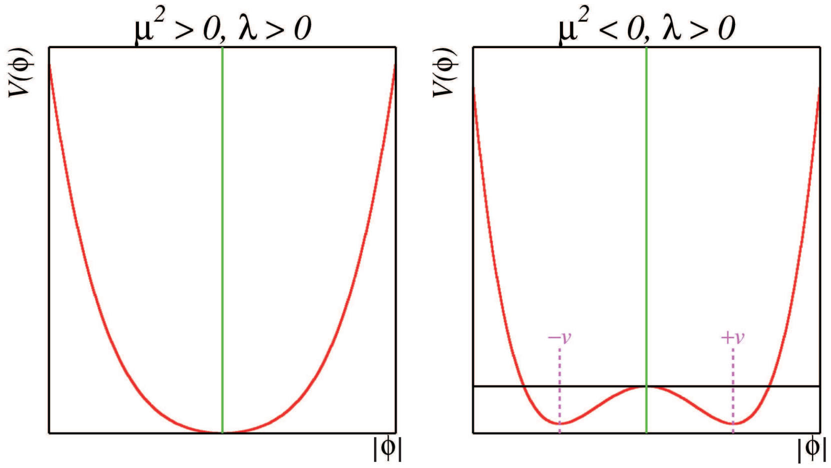

Figure 1.1: The shape of the potential $V(\Phi)$ for different values of μ [1].

This mechanism can be extended to the SU(2)⊗U(1) electroweak symmetry by considering a complex doublet of four scalar fields:

$$\Phi = \begin{pmatrix} \Psi^+ \\ \Psi^0 \end{pmatrix} = \frac{1}{\sqrt{2}} \begin{pmatrix} \psi_1 + i\psi_2 \\ \psi_3 + i\psi_4 \end{pmatrix} \tag{1.33}$$

This form of Ψ was the one originally made by Weinberg in 1967 and is called the *Weinberg-Salam* model. To generate the gauge boson masses, the same Higgs potential, $V(\Psi)$ is used with Ψ_0, the vacuum expectation value where $\psi_1 = \psi_2 = \psi_4 = 0$ and $\psi_3^2 = -\mu^2/\lambda = v$,

$$\psi_0 \equiv \frac{1}{\sqrt{2}} \begin{pmatrix} 0 \\ v \end{pmatrix} \tag{1.34}$$

This has Y=1, T=1/2 and T^3=-1/2. The choice of ψ_0 does break both the SU(2)$_L$ and U(1)$_Y$ symmetries, but ψ_0 is neutral, i.e. Q=0, so the U(1)$_{EM}$ symmetry with generator Q (=T^3 + $\frac{Y}{2}$) is unbroken. Thus the vacuum remains invariant under U(1)$_{EM}$ transformations and the photon is massless. All of the three other combinations of the four electroweak generators break the symmetry resulting in masses for the other gauge bosons. Again, examining the covariant derivative and the kinetic term in the EW Lagrangian will give us information about the interactions with the Higgs field and how the masses of the gauge bosons arise:

$$D_\mu = \partial_\mu + ig\mathbf{W}_\mu^a\mathbf{T}^a + ig'\frac{\mathbf{Y}}{2}B_\mu \tag{1.35}$$

Expanding Ψ around its vacuum expectation value using the unitarity gauge gives:

$$\psi_0 \equiv \frac{1}{\sqrt{2}} \begin{pmatrix} 0 \\ v + H(x) \end{pmatrix} \tag{1.36}$$

with H(x) real. Then again using the unitary gauge and with the substitution $T^{\pm} = (T^1 \pm iT^2)/\sqrt{2}$ and $W^{\pm} = (W^1 \pm iW^2)/\sqrt{2}$, the kinetic term, $(D_\mu\Psi)^*(D_\mu\Psi)$ becomes:

$$(D_\mu\Psi)^*(D_\mu\Psi) = \frac{1}{2}(\partial_\mu H)^2 + \frac{g}{4}(v+H)^2 W^{+\mu}W^{-}_{\mu} + \frac{1}{8}(v+H)(gW^3_\mu - g'B_\mu)^2 \tag{1.37}$$

Once this covariant derivative has been substituted into the Lagrangian as before and the transformation has been made from W^3 and B to Z and A, then the Lagrangian becomes:

$$\mathcal{L} = \frac{1}{2}(\partial_\mu H)^2 + \frac{1}{4}g^2(v+H)^2 + \frac{1}{8}(g^2+g'^2)(v+H)^2 Z_\mu Z^\mu - \frac{1}{4}\mu^2 v^2 + \mu^2 H^2 - \lambda v H^3 - \frac{\lambda}{4}H^4 \tag{1.38}$$

The terms involving v are the mass terms and those involving H describe the interactions of the $\mathbf{W}^a$ and $\mathbf{B}$ gauge fields with the Higgs field. The mass of the W boson can thus be identified as

$$M_W = \frac{1}{2}gv \tag{1.39}$$

The mass of the Z boson is

$$\mathrm{M}_Z = \frac{1}{2}\frac{gv}{\cos\theta_W} \tag{1.40}$$

It can be seen that the ratio of the squares of the W and Z masses, $\rho\cos^2\theta_W$, is a prediction of the Standard Model:

$$\rho = \frac{\mathrm{M}_W^2}{M_Z^2\cos^2\theta_W} \tag{1.41}$$

where $\rho = 1$ in the Standard Model.

Although mass terms of the form m$\bar{\psi}\psi$ were excluded by gauge invariance in the Lagrangian, the same Higgs doublet which generates the W and Z masses can also generate the fermion masses. While an explicit mass term would mix the left-handed and right-handed fermions and is not allowed, an interaction between the left-handed doublet, the Higgs doublet and the right-handed singlet is allowed. Such terms, called *Yukawa* interactions, will generate mass terms for the fermions of the form:

$$G_l[\bar{\phi}_L \Psi \phi_R + \bar{\phi}_R \bar{\Psi} \phi_L] \tag{1.42}$$

where G_l is the Yukawa coupling for leptons. For example, for electrons, this will generate a mass $m_e = G_e v/\sqrt{2}$ and a coupling to the Higgs field proportional to its mass. This will also leave the neutrino massless. The three generations of leptons are added to this model as copies of each other, with different Yukawa couplings so that the masses of the muons and the tau-leptons are correct. Slightly more complex Yukawa terms are needed when including the quark doublets and singlets, to ensure that both the 'up' and 'down' types acquire mass. For further detail see, amongst others, [12] and [24].

1.7 Current Limits on the Higgs Mass

Once the mass of the Higgs is known, all the parameters of the SM Higgs may be calculated, as the mass is the only free parameter. Currently the Higgs mass is not known, but it is possible to put upper and lower bounds on its value from theory, and experimental searches and measurements.

1.7.1 Limits from Theory

Unitarity requirements in WW scattering require that there is an upper bound of 1.2 TeV [25]. Running of the Higgs coupling, λ, with the energy scale, Λ, places tighter limits on the Higgs mass. These theoretical bounds on the Higgs mass with Λ are shown in Figure 1.2. The upper and lower limits are set by requiring that Λ has sensible values and that the Higgs potential minimum is maintained. The upper limit requires that $\lambda(\Lambda) < \infty$ from the idea that radiative loop corrections involving the Higgs self-interactions affect λ and this limit can be expressed as a constraint on the Higgs mass. At the lower limit, $\lambda(\Lambda) > 1$ as this is the requirement for vacuum stability . Assuming that SM Higgs physics is valid from the Planck mass up to $\Lambda \sim 10^{19}$GeV, then the Higgs mass will have to lie in the range 135GeV to 180GeV.

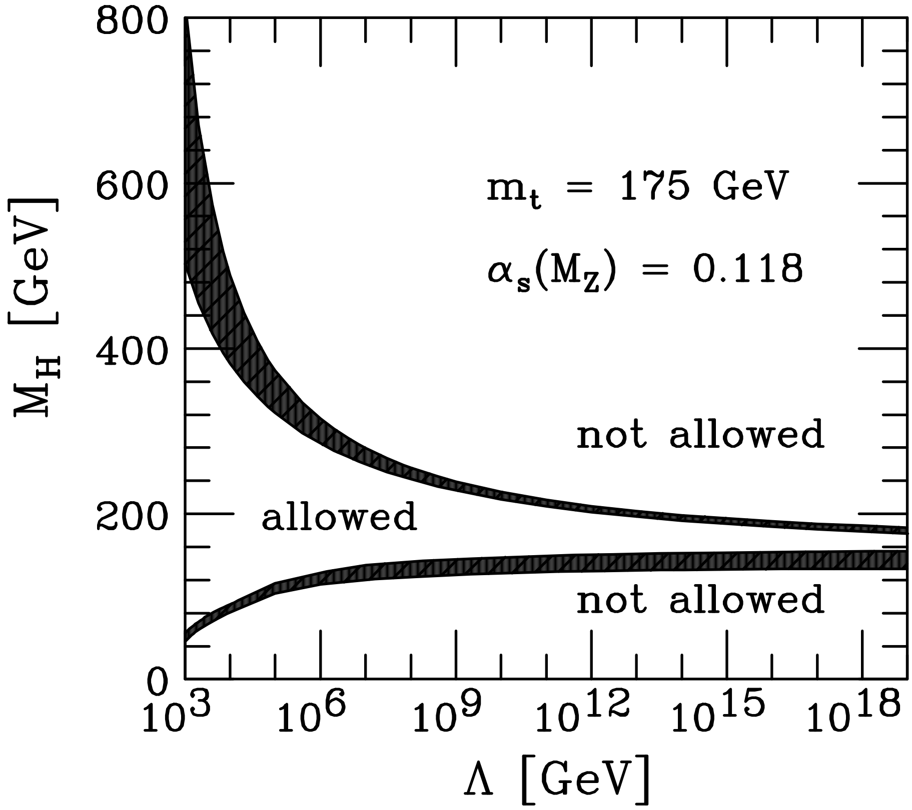

Figure 1.2: Upper and lower theoretical bounds on the Standard Model Higgs mass as a function of the energy scale. [2]

1.7.2 Limits from Indirect Methods

Many electroweak parameters are sensitive to the Higgs mass via higher order loop corrections. For example, predictions of the masses of the W boson and the top quark are related to the Higgs mass via these higher order corrections, leading to a logarithmic dependence of the Higgs mass on the W boson and top quark masses. This dependence is illustrated in Figure 1.3. The same study combined 18 separate input measurements including the width of the W boson and measurements from high-Q^2 interactions to obtain the most stringent constraint on the Higgs mass. Figure 1.4 shows the $\chi^2(m_H) = \chi^2_{min(m_H)} - \chi^2_{min}$ curve [3] as a function of Higgs mass. The preferred value for M_H, corresponding to the minimum of the parabola given by the black line, is 85 GeV, with an experimental uncertainty of +39GeV and -28GeV (at 68% C.L.) The 95% C.L. upper limit on M_H <199GeV.

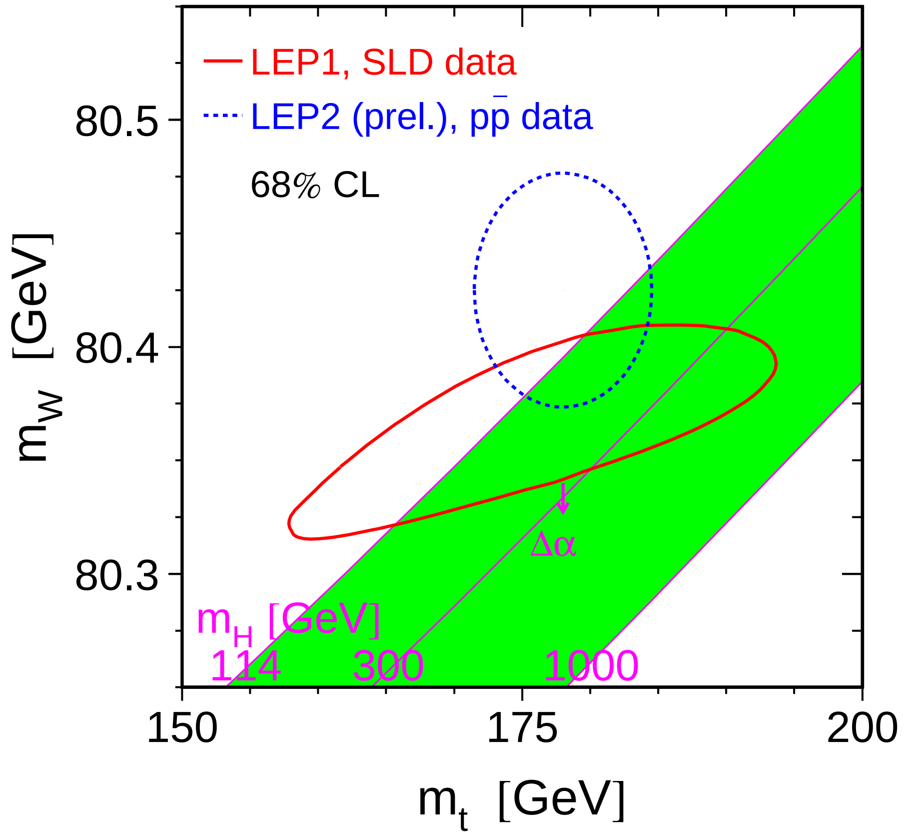

Figure 1.3: Contour curves of 68% probability in the (m_t,m_W) plane. The shaded band shows the SM prediction for the Higgs mass. [3]

1.7.3 Limits from Direct Methods

Direct searches for the Higgs have also been carried out using the production mechanisms and decay modes that combine to give the greatest sensitivity at that particular collider. The most stringent limits on the Higgs mass come from the measurements made at LEP2 [26]. The primary production mechanism expected at LEP was the Higgs-strahlung process, $e^+e^- \rightarrow HZ$, with small contributions from W and Z boson fusion processes . For masses around 115GeV, the Higgs is expected to decay mainly into $b\bar{b}$ pairs, with searches including all possible decay modes for the Z combined. The LEP collaborations performed a search on 2465pb^{-1} of data, from e^+e^-collisions between 189GeV and 209GeV, and have imposed a lower bound

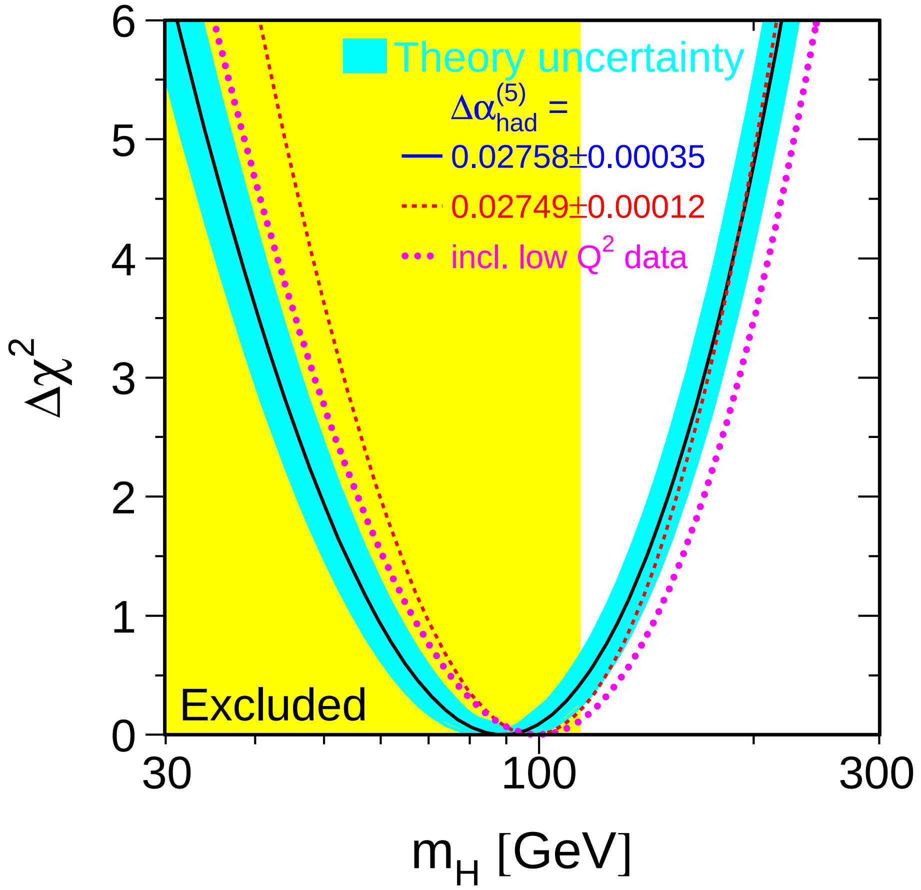

Figure 1.4: $\chi^2(m_H) = \chi^2_{min(m_H)} - \chi^2_{min}$ as a function of m$_H$. The line is the result of the fit using 18 electroweak parameters. [3]

of 114.4GeV on the Higgs mass at the 95% C.L. The likelihood analysis shows some preference for a Higgs boson with a mass of 115.6GeV, with the probability for the background to generate the observed effect of 3.4%. The production mechanisms and decay modes of the light SM Higgs boson are discussed in more detail in Chapter 5.

Prior to LEP2, Higgs searches were also carried out by the CDF collaboration at the Tevatron during Run I [27], though the results are weaker than those of the LEP2 search. The Higgs was searched for in associated production with a W or Z boson, where the Higgs decays to a $b\bar{b}$ pair, in approximately 110 pb^{-1} data taken at a centre-of-mass energy of 1.8 TeV. CDF measured upper limits on $\sigma(p\bar{b}\rightarrow VH)\times BR(H\rightarrow b\bar{b})$ which are substantially higher than those predicted in the Standard Model. With the higher energy collider and the larger dataset available, Higgs searches have returned to the physics agenda at the Tevatron, with ZH being one of the most sensitive production mechanisms due to its large production cross-section and the large branching ratio of $Z \rightarrow \nu\bar{\nu}$.

1.8 Conclusions

The Standard Model currently well-describes the strong, electromagnetic and weak forces and the fundamental particles, the leptons and the quarks, that we observe in high energy physics experiments. It is based on a SU(3)$\otimes$SU(2)$_L\otimes$U(1)$_Y$ symmetry, with the weak and EM forces unified in the electroweak theory. This symmetry itself does not explain the masses of the W and Z quarks, nor why the symmetry is broken such that the photon remains massless.

To generate mass, the Higgs mechanism is introduced whereby the SU(2)$\otimes$U(1)$_Y$ symmetry is spontaneously broken down to the U(1)$_{EM}$ symmetry. This mechanism generates the masses of the gauge bosons and the fermions, but it cannot predict their masses nor the mass of the Higgs boson itself, all of these being just parameters of the theory. Many observables within the electroweak sector are sensitive to the Higgs mass (M$_H$), and by measuring these accurately, constraints may be placed on M$_H$. The predicted Higgs couplings to the gauge bosons and the fermions are proportional to their masses. Since the Higgs is massive, it is only high-energy facilities like the Tevatron and the LHC that will be able to discover the Higgs if it exists in this form. Theory suggests that the Higgs mass is probably between 135GeV and 180GeV [2], but combined results from indirect and direct searches compellingly indicate that the Higgs has a mass greater than 114.4GeV from direct searches. Indirect evidence points to M$_H$ <200GeV.

At the Tevatron, for Higgs with a mass around 130 GeV, the most promising production mechanism is $q\bar{q} \rightarrow VH$ (V is Z/W), and where this is followed by the decay of the Higgs to a $b\bar{b}$ pair and the leptonic decay of V. The final states with the most potential are $l\nu b\bar{b}$, $\nu\bar{\nu}b\bar{b}$, $l\bar{l}b\bar{b}$, and $q\bar{q}b\bar{b}$ with the main backgrounds Wbb and WZ processes. This means that the b-tagging capability, the jet energy resolution, and the $\not{E}_T$ resolution and coverage are the key elements for good discrimination of any possible signal.

Chapter 2

Experimental Apparatus

The Tevatron is the highest energy collider (proton-antiproton, $p\overline{p}$) currently in operation. It runs with a centre of mass energy of $\sqrt{s}$=1.96TeV at the Fermi National Accelerator Laboratory (Fermilab) near Chicago. DØ and CDF are the two large, general-purpose collision-detector experiments that are part of a wide experimental programme that also includes research into neutron physics and medical physics amongst other things. In this chapter, an outline is given of the accelerator complex needed to reach this centre of mass energy, a brief description of the DØ detector apparatus is presented, and an explanation of how particles interact with the detector is given. The main focus of the DØ experiment is Higgs physics, b-quark physics, and high p_T phenomena[1]. The running of the detector is split into two runs: Run I and Run II. The original detector [28] has been upgraded several times since 1992. During Run I, which lasted from 1992 - 1996, significant results included the discovery of the top quark [29], and the measurement of its mass [30],[31]. Run II can be divided into Run IIa and Run IIb; the split was defined by further upgrades to enable the detector to cope with the increased luminosity of the Tevatron. The current DØ detector is described in detail in [32] and the Run IIa/b upgrades are described in [33]. This thesis focuses on studies with the Run IIa detector only, which started in March 2001, after extensive upgrades to the DØ detector.

---

[1] High p_T phenomena: these include top quark physics, W physics and QCD measurements.

2.1 The Tevatron

The Tevatron is the final stage in a system of seven parts shown in Figure 2.1. The system may be thought of as a series of three processes: particle production and pre-acceleration, particle storage, and acceleration to the collision energy of 0.98TeV [34],[35].

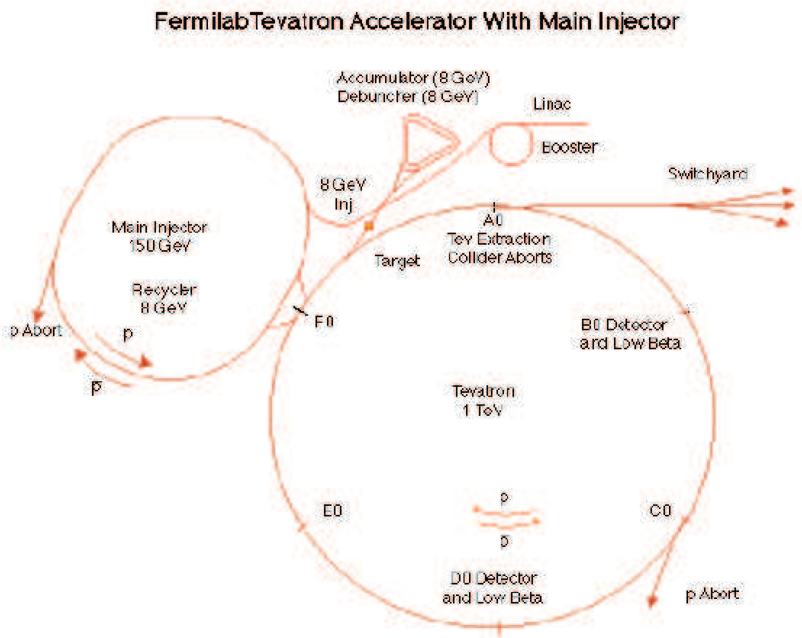

Figure 2.1: The Tevatron Accelerator Complex

2.1.1 Production, storage and pre-acceleration of protons and anti-protons

The first stage in proton production takes place inside a magnetron [36] which produces H^- ions. These are then pre-accelerated by a Cockroft-Walton generator [35] to 750 keV and sent to the Linac. The Linac increases the particle energy to 400 MeV over a distance of 80m. The H^- ions are then led to the Booster which is the first in a series of three synchrotrons. Here, the protons from the Linac are combined with protons already in circulation in the Booster. The final electrons are stripped from the H^- ions by passing the beam through a graphite sheet. Once sufficient protons are accumulated in the Booster, they are sent to the main injector to be further accelerated. Some of the accelerated protons from the main injector are used in the antiproton system which comprises the target station, the debuncher and the accumulator, shown in Figure 2.1. These protons from the main injector are directed onto a Nickel target at 120GeV, producing a shower of secondary particles, some of which are $\bar{p}$. A lithium lens is used to focus the wide beam produced and to remove positively charged particles. Stochastic cooling[2] is then used to reduce the momentum and position spread of the antiprotons in the debuncher and accumulator.

It is very difficult to produce antiprotons and approximately 20 antiprotons are produced for every million protons used in this process. The antiprotons are stored in the accumulator until a sufficient number have been collected to transfer to the main injector and this process, known as a *store*, takes many hours.

2.1.2 Particle Acceleration

The main injector is a circular synchrotron of diameter 1km. It accelerates the protons and antiprotons from the booster and the antiproton source to 150GeV and injects them into the Tevatron. The Tevatron is the final synchrotron in which the protons and antiprotons are accelerated in opposite directions in the same beam pipe. It uses 774 dipole and 216 quadrupole superconducting magnets with fields up to 4T at the temperature of liquid Helium. The Tevatron has a diameter of 2km and increases the energy of the particles to 0.98 TeV. From Figure 2.1, it can be seen that protons travel clockwise around the ring from BØ (CDF) towards DØ (and around and out towards the fixed target experiments via the switchyard). The protons and anti-protons ($p\overline{p}$) are grouped together in bunches, and the Tevatron creates 36 bunches approximately 50 cm long, of both protons and antiprotons from each store, separating them into three groups of 'super bunches'. The bunches are

---

[2] Stochastic cooling: technique to reduce momentum spread in a storage ring for charged particles. Fluctuations in the position of the bunches are detected and a correction (a ”steering pulse” or ”kick”) with the opposite sign is applied. Stochastic refers to the fact that usually not all particles can be corrected at once; they are cooled down in multiple steps. [37]

made to collide at two points on the Tevatron ring with a time spacing between each collision of 396ns; one of the points is labelled DØ , hence the experiment's name.

2.1.3 Tevatron Performance

It is anticipated that the Tevatron will continue running, producing good physics, until a little while after the LHC at CERN comes online in 2007, when Run II will end. The total Run IIa integrated luminosity, from 19th April 2002 to 23 May 2006, as recorded by DØ was $1.18fb^{-1}$. Some of the characteristics of Run II are summarised in Table 2.1.

Run II at the Tevatron was originally planned to deliver $2fb^{-1}$ but studies of the physics potential in 2000 and 2003, most notably potential for finding evidence of the Higgs boson, led to a revised goal of $8fb^{-1}$. The Tevatron underwent extensive upgrades, to gradually increase its peak luminosity to $2 \times 10^{32}cm^{-2}s^{-1}$, more than four times the peak luminosity in Run I, and to decrease the bunch spacing from 396ns to 132ns. The current integrated luminosity has already exceeded the design specifications and it is anticipated that the integrated luminosity to be delivered will be 4.4fb^{-1} and 8.8fb^{-1} over the whole of Run II; Figure 2.2 shows the projected integrated luminosity over the next few years.

	Run II
Centre of mass energy	1.96TeV
Bunch Spacing	396ns
Number of p and $\bar{p}$ bunches	36
Number of protons per bunch	2.7×10^{11}
Number of antiprotons per bunch	4.2×10^{10}
Base integrated luminosity	$4.4fb^{-1}$
Design integrated luminosity	$8.8fb^{-1}$

Table 2.1: Some key operating characteristics of the Tevatron for Run II

2.2 The DØ Detector

The DØ detector is multi-purpose and constructed like the layers of an onion around the interaction point. It can measure precisely the kinematic properties of

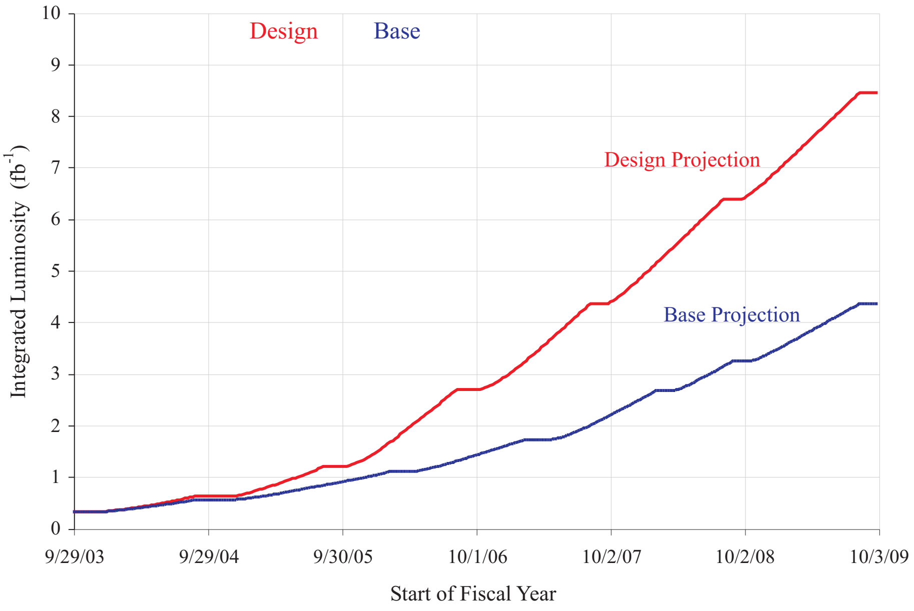

Figure 2.2: Base and design projected integrated luminosity from the Tevatron up to 2009 [4]

the particles passing through it by examining their positions and energies. The detector comprises three major subsystems: at the centre there is a tracking system that includes a 2T solenoid, around this there is a uranium/liquid argon calorimeter, and then surrounding this there is a muon system with a toroid magnet to measure the momenta of muons. Figure 2.3 shows the layout of the detector and these subsystems, the following subsections describe the detector coordinate system and these detector subsystems in more detail. Full details can be found in [32].

2.2.1 The Detector Coordinate System and Units

Both polar and Cartesian coordinates are used to describe particles within the detector. These two sets of coordinates are referred to in two different ways, the first being *physics coordinates* where the origin is set at the point of interaction, and the second is *detector coordinates* where the origin is set to the centre of the DØ detector. All momenta and energies are given in GeV.

Cartesian A right-handed system is used with the z-axis increasing along the proton beam (south). The origin of coordinates is the centre of the detector, with

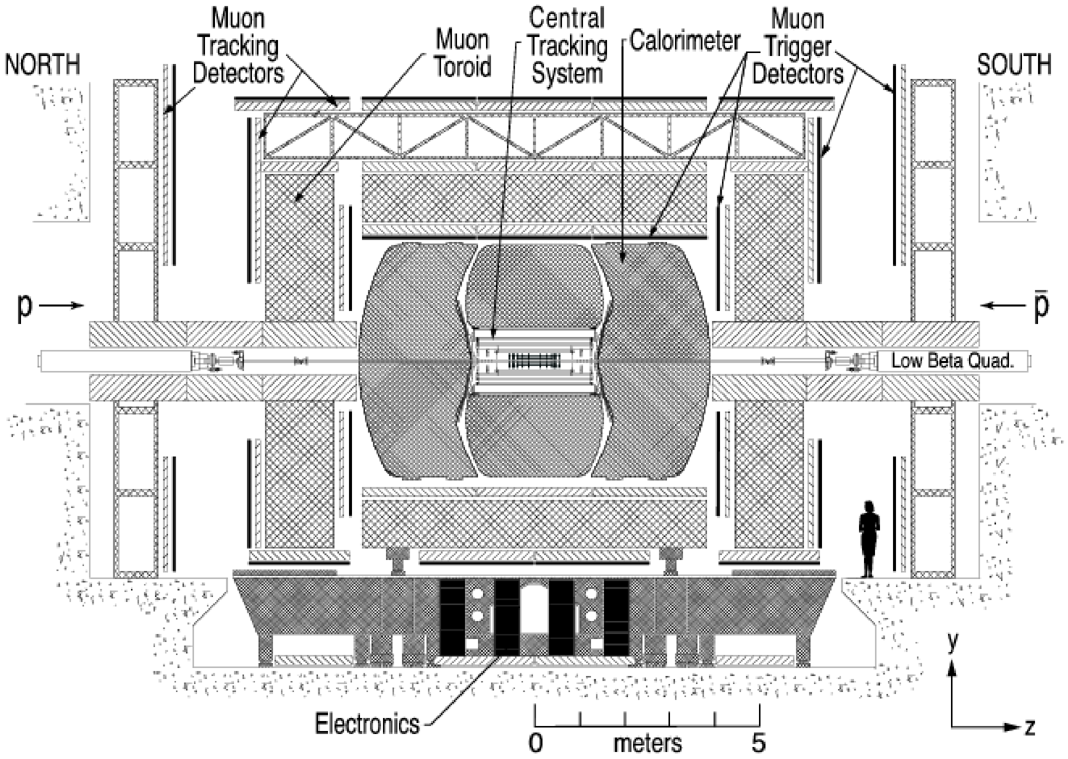

Figure 2.3: The DØ detector

y increasing with height. Positive x points outwards from the centre of the ring (East). Distances in the detector are usually measured in cm.

Polar These are used interchangeably with the Cartesian coordinates, and the transformations are as follows:

$$r = \sqrt{(x^2 + y^2)}$$

$$\phi = \arctan y/x$$

$$\theta = \arccos z/\sqrt{(x^2 + y^2 + z^2)}$$

where:

- r is the perpendicular distance from the z-axis.
- The azimuthal angle, ϕ, is measured in radians from 0 to 2π, with $\phi = 0$ for $x > 0$, $y = 0$ and $0 < \phi < \pi$ for $y > 0$.

- θ is measured in radians from 0 to π, with $\theta = 0$ for $x = y = 0$ and $z > 0$, $\theta = \pi$ for $x = y = 0$ and $z < 0$.

Pseudo-rapidity A quantity called pseudo-rapidity (η) is frequently used instead of θ: $\eta = -\ln \tan \theta/2$. Positive η points South. This is derived from the rapidity, which is Lorentz invariant, given by $y = \frac{1}{2}[\ln(E + p_z)/(E - p_z)]$ where the particle masses are zero, i.e. $\eta \equiv y$ if $m = 0$ ($\equiv \beta = 1$). This is an appropriate transformation of θ as the number of high-energy particles (where $E \gg m$) is approximately constant in η. Furthermore, intervals in η are Lorentz invariant under boosts parallel to the z-axis.

2.2.2 Central Tracking System

Excellent measurement of particle tracks around the interaction point is important for studies of the top and bottom quarks, electroweak interactions, and for searches for new phenomena. The central tracking system is used to measure charged particle paths (*tracks*), calculate momenta, and the position of interaction vertices. It comprises a silicon microstrip tracker (SMT), a scintillating fibre tracker (CFT) and a surrounding solenoid magnet. A schematic view of the central tracking system is shown in Figure 2.4. It is the first part of the detector particles meet after the $p\overline{p}$ collision in the beryllium beam pipe. The signals left in the SMT and CFT by particles travelling through are referred to as hits. The momentum of the particle can be calculated from the radius of curvature of the particle, R, in the field B, as the Lorentz force provides the centripetal force for the circular motion of the particle, giving rise to the relationship $p = eBR$.

Silicon Microstrip Tracker

The SMT provides tracking and vertexing over nearly the full η coverage of the calorimeter and muon systems out to about $|\eta| \sim 4$. Centrally, it comprises six barrels along the beam pipe each with four single-sided or double-sided detector layers. Moving towards large $|z|$, each barrel is capped by a detector disk (*F-disk*) aligned perpendicular to the beam pipe and holding 12 double sided detector wedges.

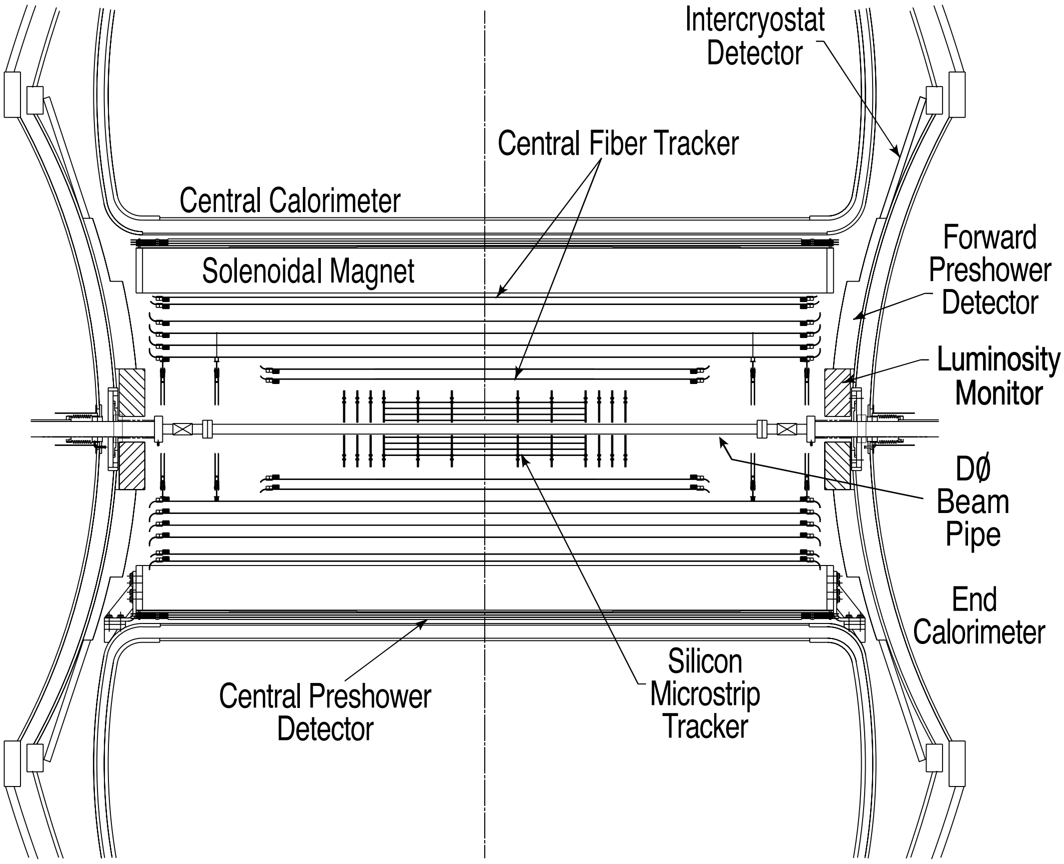

Figure 2.4: Cross-sectional view of the new central tracking system in the x-z plane. Also shown are the locations of the solenoid, the preshower detectors, luminosity monitor, and the calorimeters

There are three more F-disks on each side of the unit at larger $|z|$. There are a further three larger disks (*H-disks*) in both far-forward regions each with 24 single-sided detector wedges mounted back-to-back. The symmetric design of the detector, electronics, and cooling are, in large part, dictated by the accelerator environment and the long length of the interaction region ($\approx$ 25 cm) sets the length scale of the device. With a long interaction region, it is difficult to position detectors such that the tracks are generally perpendicular to detector surfaces for all η. This led to a design of barrel modules interspersed with disks in the centre and assemblies of disks in the forward regions. The barrel detectors primarily measure the $r-\phi$ coordinate and the disk detectors measure $r-z$ as well as $r-\phi$. This allows vertices for particle interactions at high-η to be reconstructed in three dimensions by the disks, and vertices of particle interactions at small η to be measured in the barrels and central fiber tracker. An isometric view of the SMT is shown in Figure 2.5. The barrels and the F-disks have outer radii of about 8 - 10 cm and the H-disks have outer radii of 26 cm. The barrels extend ±38 cm from the centre of the detector. The centres of the H-disks are located approximately 1 m from the interaction point, with the F-disks between 0.13 m and 0.53 m from the interaction point. The detector layers and wedges are made from n-type silicon with active readout strips in which electron-hole pairs are created by the passage of charged particles. The readout strips are arranged parallel to the long edge of the wedges and axially in the barrels[3]. To measure the z-coordinate in the barrels, there is a stereo angle of 2° or 90° between strips on opposite sides in the double-sided layers. Nearly 800,000 readout channels carry signals that have been collected, digitized and readout by 6000 custom-made 'SVXIIe' readout chips The large number of readout chips generates thermal noise and heat that may damage the silicon so ethylene-glycol coolant flows through the supports maintaining the silicon temperature below 5°C.

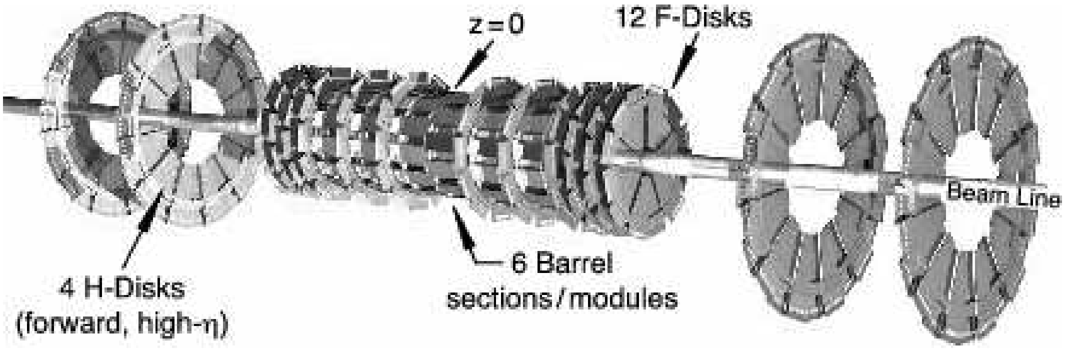

Figure 2.5: The disk and barrel design of the silicon microstrip tracker.

Scintillating Fibre Tracker

The scintillating fibre tracker (CFT) consists of scintillating fibres mounted on eight concentric support cylinders that extend 20 - 52 cm radially from the centre of the beam pipe. The outermost cylinder provides coverage for $|\eta| \lesssim 1.6$. The fibres are arranged in superlayers of axial *doublet* layers and stereo doublet layers at an angle of 3° so as to leave no gaps in the tracking. The scintillating fibres are made of

---

[3] Aligned along the beam pipe

polystyrene, doped with an organic fluorescent dye that emits photons at 530nm when its atoms are excited by incoming charged particles. The photons are trapped within the polystyrene by outer layers of polymethylacrylate and fluoro-acrylic and transmitted via clear fibre waveguides to visible light photon counters (VLPCs) [38] to be read out. The VLPCs are avalanche photodetectors that operate at 9K and are capable of detecting single photons and converting them into thousands of electrons, eventually to be readout by 'SVXIIe' chips. Light is observed only from one end of each fibre, so, at the non-readout end there is a mirrored coating (aluminium) with 90% reflectivity.

Performance and Status

The overall momentum resolution of the tracking system is dependent on the momentum itself :

$$\frac{\sigma_T}{p_T} = \sqrt{0.015^2 + \frac{0.0014{p_T}^2}{GeV/c}} \tag{2.1}$$

The two tracking detectors are together capable of locating the primary interaction vertex with a resolution of $35\mu m$ along the beam line. They can tag b-quark jets[4] with an impact parameter resolution better than $15\mu m$ in $r - \phi$ for particles with transverse momentum greater than 10GeV at $|\eta| = 0$. As of May 2005, 90% of the sensors in the SMT were functional with problems mostly occurring along the readout chain rather than on the silicon itself.

As part of the Run IIb upgrade [33] an additional layer, *Layer 0*, was added to the silicon tracker system. This additional layer is situated at small R (∼1.6cm). This is designed to recover tracking performance and B-identification efficiency losses from radiation damage to the silicon and aging. It will also improve impact parameter resolution. New readout electronics for the central fibre tracker were also added to improve tracking efficiency at high luminosity.

2.2.3 Calorimeter and pre-shower

The DØ calorimeter is designed to measure the energy of electrons, photons and jets, to aid the identification of electrons, photons, jets and muons, and to measure

---

[4] See Section 2.2.8 for further explanation

the transverse energy balance in events. It consists of a central calorimeter (CC), two end calorimeters (EC[5])and an intercryostat detector (ICD) shown in Figure 2.6. The central and end calorimeters are subdivided into three layers: the electromagnetic (EM) layer which is designed to measure electrons, positrons and photons, known collectively as electromagnetic (EM) objects. The fine (FH) and coarse (CH) hadronic layers measure hadronic showers of particles. The CC covers $|\eta| < 1$ and the two end calorimeters extend the coverage to $|\eta| = 4$. Each section is located within its own cryostat to maintain the temperature at about 90K.

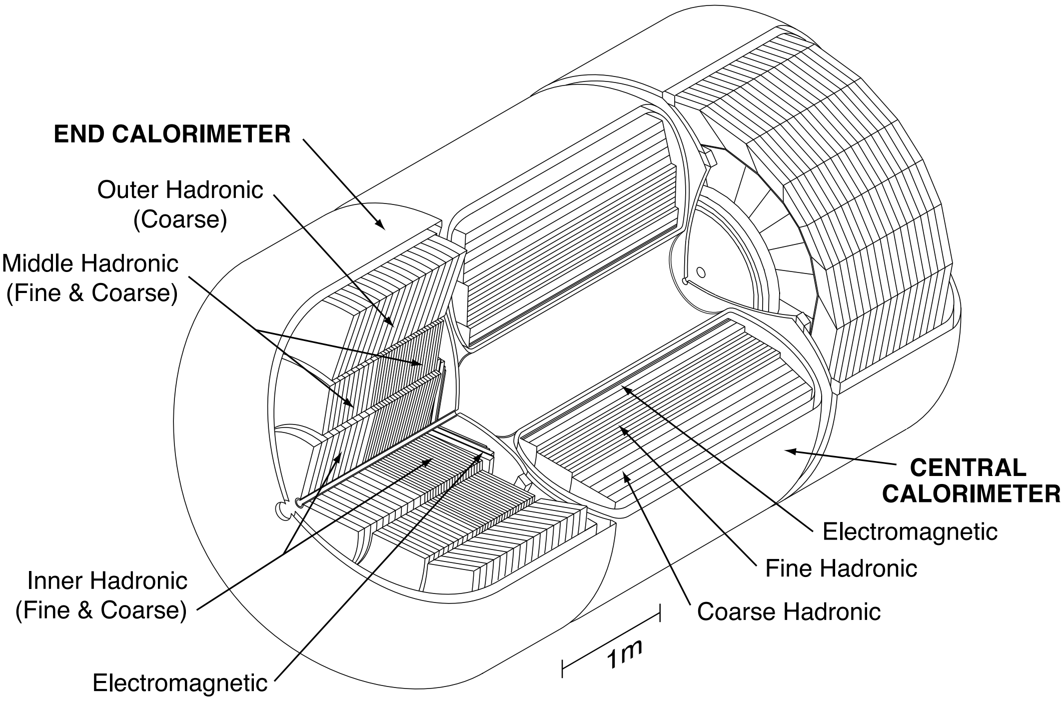

Figure 2.6: Isometric view of the central and two end calorimeters

Within each section, there are layers of readout cells arranged along lines of η, shown in Figure 2.7. These readout cells perform the basic energy measurements of particles in the calorimeter. A single readout cell comprises metal absorber plates to initiate showering interleaved with the active medium of liquid Argon in which there are copper readout pads for collecting the ionisation. Figure 2.8 shows the arrangement of such a readout cell. There is a gap of 2.3 mm between the absorber plates where particles ionise the Argon atoms. There is a 2kV potential across this

---

[5] EC: The EC is further subdivided into the North (ECN) and South (ECS) end caps

gap which causes the electrons to drift towards the signal pads in approximately 450ns. The dimensions of the readout cells, the metal used in the absorber plates (either Uranium or steel) and the thickness of the layers are all dependent on the location of the cell in the calorimeter; these data are summarised in Table 2.2.

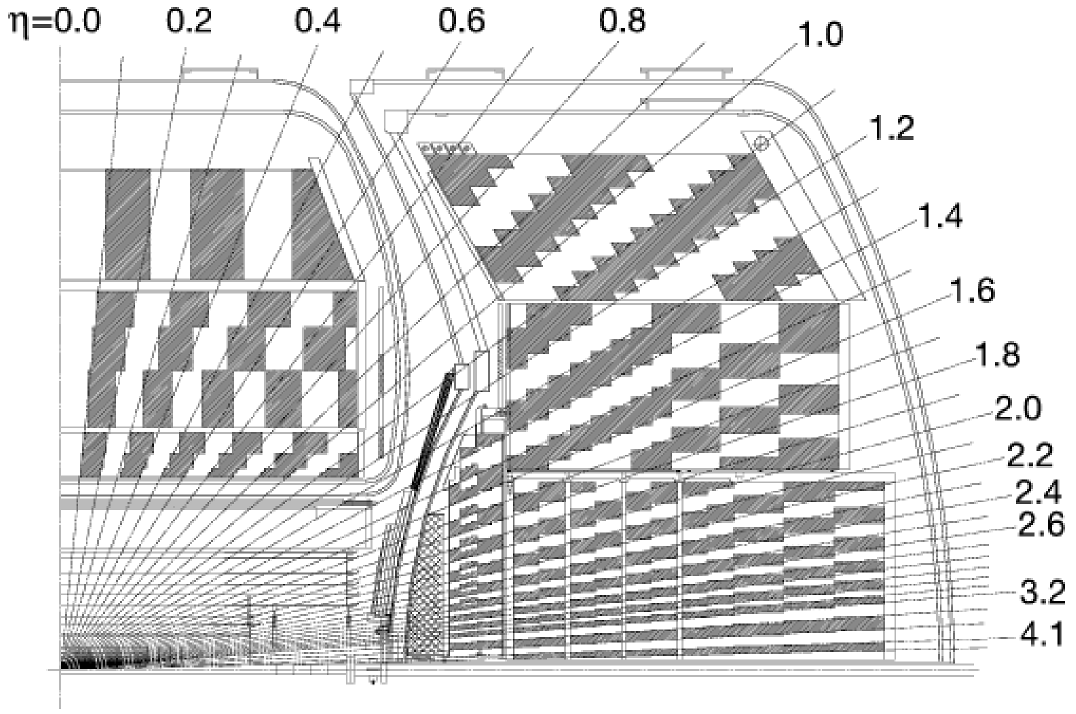

Figure 2.7: Schematic view of a portion of the DØ calorimeters showing the transverse and longitudinal segmentation pattern. The shading pattern indicates groups of cells ganged together for signal readout. The rays mark pseudorapidity intervals from the centre of the detector.

The materials are chosen so that the energy response is the same for EM particles as for hadronic particles so that the calorimeter is *compensating*. The electromagnetic plates in the CC and EC are made from nearly pure depleted uranium and the fine hadronic sections are made from 6mm-thick uranium-niobium (2%) alloy. The readout cells cover transverse areas approximately the size of EM showers (1-2cm) and hadronic showers (10cm), so the hadronic sections are less finely segmented than the EM sections. The segmentation in $\eta - \phi$ space is $\triangle\eta \times \triangle\phi = 0.1 \times 0.1$ except

Layers		Absorber Material	Layer thicknesses	No. of layers	Module dimensions $\triangle\eta \times \triangle\phi$
CC	EM	Uranium	1.4, 2.0, 6.0, 9.8 χ_0	4	0.1×0.1*
	FH	Uranium	1.3, 1.0, 0.76λ_A	3	0.1×0.1
	CH	Copper	3.2λ_A	1	0.1×0.1
EC	EM	Uranium	1.6, 2.6, 7.9, 9.3 χ_0	4	0.1×0.1*
	FH	Uranium/Steel	0.9, 0.9, 0.9, 0.9λ_A	4	0.1×0.1
	CH	Stainless Steel	4.4 - 6.0λ_A	1/3	0.1×0.1

Table 2.2: Table of materials used in the central and end calorimeters and dimensions of these layers. See Section 2.2.8 for explanation of χ_0 and λ_A. (*except 3^{rd} layer: 0.05×0.05)

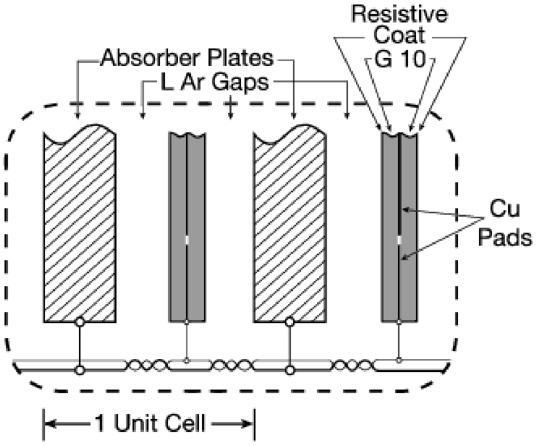

Figure 2.8: Schematic view of the liquid argon gap and signal board unit cell for the calorimeter

in the third EM layer where the $\eta - \phi$ segmentation is twice as fine. EM showers are expected to deposit almost all of their energy in the EM sections and the third EM layer is the most finely grained as this is where the shower maximum occurs. The hadronic showers will deposit most of their energy within the hadronic layers. Only muons are expected to make it through the calorimeter with minimal energy loss, and neutrinos are not expected to deposit energy at all. See Section 2.2.8 for further explanation of the interaction of particles with the detector.

Intercryostat Detector and Massless Gaps Since the calorimeter is divided into three separate sections each contained within its own cryostat, there is incomplete coverage in the pseudo-rapidity region $0.8 < |\eta| < 1.4$ between the systems. To address this problem, there are additional layers of sampling. Within the central and end cryostats, there are single-cell readout structures called *massless gaps*. In the region $1.1 < |\eta| < 1.4$ there is a scintillator sampling detector called the *intercryostat detector* (ICD) which is attached to the exterior surface of the end cryostats and this can be seen in Figure 2.3. The ICD is a series of scintillating tiles approximately 1.3cm thick and enclosed in light-tight aluminium boxes. Each tile covers an area $\triangle\eta \times \triangle\phi \approx 0.3 \times 0.4$ and is further subdivided to match the sampling geometry of the rest of the calorimeter. Although sampling can now take place in the gaps between the calorimeter so that the overall energy resolution is improved, the resolution in the ICD and massless gaps is poorer than that of the main calorimeter sections.

Performance and Status

The calorimeter modules were calibrated using beams of electrons, pions and muons between 10GeV and 150GeV before being installed in the DØ detector [39]. The calorimeter resolution is energy dependent and of the quadratic form:

$$(\frac{\sigma}{E})^2 = C^2 + \frac{S^2}{p} + \frac{N^2}{p^2} \tag{2.2}$$

where p is the beam momentum in GeV/c, C is a constant contribution from systematic errors such as variation in gain between readout modules, S is due to the statistical error in sampling, and N represents energy independent contributions to σ such as electronic and uranium noise. The calorimeter has an EM sampling resolution of S $= 0.157/\sqrt{E}$, constant term of C $= 0.003$ and N $= 0.29$. The hadronic sampling resolution is S $= 0.45/\sqrt{E}$ and the constant term, C, is 0.04. The response of the calorimeter is linear to 0.5%, and the EM/hadronic response ratio is between 1.02 and 1.09 over this range of momenta.

2.2.4 Muon System

Muons from $p\bar{p}$ interactions are minimum ionizing particles (MIPs[6]) and pass through the detector tracker and calorimeter systems with little interaction, thus the DØ muon detector system is the outermost layer of the detector. The muon system is wrapped around the calorimeter and divided into the central muon system, with coverage out to $|\eta| \lesssim 1.0$, and the forward muon system which extends coverage to $|\eta| \backsimeq 2.0$. It provides identification of muons, allowing triggering on them and crude measurements of their momenta and charge. Figures 2.9(a) and 2.9(b) show the arrangement [40].

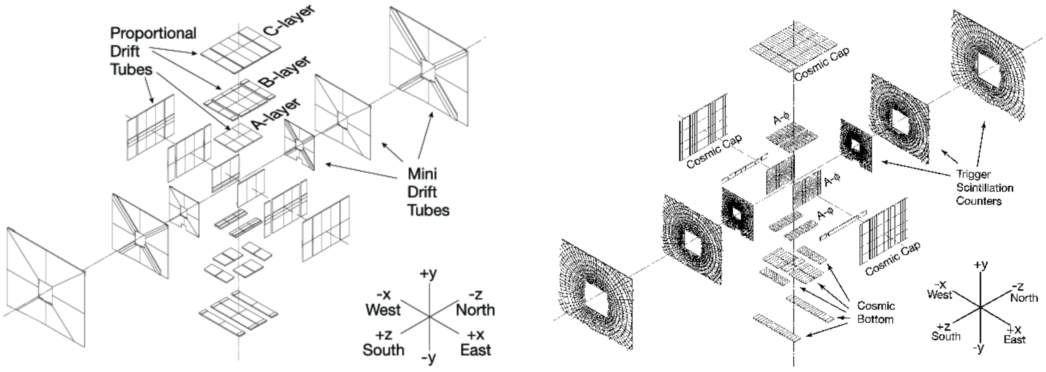

(a) Muon wire chambers

(b) Muon scintillation detectors

Figure 2.9: Exploded view of the muon detectors

Central Muon System

The central muon system comprises a toroidal magnet, drift chambers, cosmic cap and bottom counters, and triggering scintillation counters. There are three layers of proportional drift chambers, approximately $2.8 \times 5.6m^2$ in size and made from rectangular extruded aluminium tubes. There is one layer inside the magnet, and two layers outside. These PDTs provide position resolutions between 10 and 50 cm. The innermost layer is covered with scintillation counters providing a fast detector

---

[6] Cosmic muons and fast electrons are both examples of MIPs as they have low mass and high energy. The energy loss through ionization for a MIP per unit path length is typically a few MeV cm^{-1} material.

for triggering on and identifying muons, to compensate for the 750ns drift time of the PDTs. Cosmic cap and bottom counters (scintillators) are installed on the top, sides and bottom of the outer layer of the central muon PDTs. They provide a fast timing signal to associate a muon in a PDT with the appropriate bunch crossing and discriminate against the cosmic ray background.

Toroidal Magnets The stand-alone muon-system momentum measurement allows for a low p_T cut-off in the Level 1 muon trigger, cleaner matching with central detector tracks and rejection of π/K decays and improves momentum resolution for high momentum muons. The central toroid is a square annulus, 109 cm thick whose innermost surface is 318 cm from the beam line, and is constructed in three parts. There is a centre-bottom section, which provides a base for the calorimeters and central tracking detectors. There are also two c-shaped sections located at $454 \leqslant |z| \leqslant 610$ cm. The toroid coils carry a current of 1500A resulting in an internal field of about 1.8T.

Central Muon Drift Chambers These are made from rectangular extruded aluminium tubes filled with a mixture of argon, methane and CF_4 to reduce drift time. These are arranged in three layers (A, B and C), with A closest to the interaction region. Each layer has three decks of cells, with the exception of the A-layer, which has four decks, with 24 cells, each 10.1cm across, per deck. There is an anode wire at the centre of each cell to collect the ionisation, and these are ganged together in pairs within a deck and readout by electronics located at one end of each chamber. Cathode pads are located above and below the wires to provide information on the hit position along the wire. The multi-layer nature of the chambers allows each layer to reconstruct track segments. There are no drift tubes at the bottom of the muon system in the A-layer as this is where the support structure for the calorimeter lies. For each PDT hit, the following information is recorded: the electron drift time, the difference, $\triangle T$, in the arrival time of the signal pulse at the end of the hit cell's wire and at the end of the readout partner's wire, and the charge deposition on the inner and outer pads. Both $\triangle T$ and the charge deposition are used to determine the hit position along the wire. The $\triangle T$ measurement error depends on whether the muon passes through the cell close to or far from the electronics - the closer to the electronics, the better the resolution.

Scintillation Counters These provide a fast detector for triggering on and identifying muons and for rejecting out-of-time backscatter from the forward direction. In-time scintillation counter hits are matched with tracks in the CFT and the Level 1 trigger for high-p_T single muon and low-p_T di-muon triggers. The counters also provide the time stamp for low-p_T muons that do not penetrate the toroid and so do not reach the cosmic cap or bottom counters.

Forward Muon System

This forward muon system consists of four major parts: the end toroidal magnets, three layers of MDTs for muon track reconstruction, three layers of scintillation counters for triggering on events with muons and shielding around the beam pipe. This part of the muon system receives more radiation and so MDTs were chosen for their short electron drift time ($<$ 132 ns), good coordinate resolution ($<$ 1mm), radiation hardness, high segmentation and low occupancy. Similarly to the central muon system, the MDTs are arranged in three layers (A, B and C), with A closest to the interaction region inside the magnet. The tubes are also arranged in three planes in layers B and C, and in four layers in A, with the tubes mounted along the magnetic field lines. The maximum tube length is 5830 mm in layer C. The MDT system uses a CF_4-CH_4 (90%-10%) gas mixture, and the MDTs themselves are made from extruded aluminium with stainless steel covers.

Trigger Scintillation Counters The muon trigger scintillation counters are mounted inside and outside of the toroidal magnet. Each layer is divided into octants containing about 96 counters. The design was optimised to provide good time resolution and amplitude uniformity for background rejection, high muon detection efficiency, and reasonable cost for the 5000 counters.

	α	β	γ
Central	0.3621±0.0376	3.089±0.2048	0.0314±0.00297
Forward	0.2108±0.0101	1.785±0.1557	0.00575±0.00048

Table 2.3: Momentum resolution parameters for the central and forward muon detectors. [9]

Shielding Scattered proton and antiproton fragments that interact with the end of the calorimeter or with the beam pipe, p and $\bar{p}$ fragments interacting with the Tevatron low-beta quadrupole magnets[7] to produce hits in the B and C layers of the forward muon system, and beam halo interactions from the tunnel all contribute to non-muon background in the muon system. The shielding, consisting of layers of iron, polyethylene and lead in a steel structure, helps to reduce these backgrounds and helps to reduce any radiation damage to the detector.

Performance and Status

The momentum (p) resolution of the muon detector can be parameterised as [9]:

$$\frac{\sigma(1/p)}{(1/p)} = \frac{\alpha \times (p - \beta)}{p} \oplus \gamma p \tag{2.3}$$

where α is the contribution from multiple scattering, β represents the energy lost in the detector material before the muon system, and γ is the contribution from the finite position resolution of the muon chambers. The values of these parameters are listed in Table 2.2.4. Since the forward and central systems are different, they are treated separately. Table 2.2.4 summarizes the values of these parameters.

The stand-alone momentum resolution of the forward muon system is approximately 20% for muons with a momentum below 40 GeV. The overall momentum resolution is defined by the central tracking system for muons with momentum up to approximately 100 GeV. The forward muon system improves the resolution for higher momentum muons and is particularly important for tracks with $|1.6| \lesssim \eta \lesssim |2.0|$, i.e. those which do not go through all layers of the CFT.

---

[7] These magnets focus the beam to create collisions of high luminosity. Low beta magnets are installed at BØ and DØ .[41]

2.2.5 The Forward Proton Detector

This measures protons scattered at small angles (∼1 mrad) that do not interact with the main DØ detector. A forward proton detector is necessary for access to the full kinematics of the scattered particle. It consists of a series of momentum spectrometers that use the accelerator magnets in conjunction with position detectors along the beam line. The position detectors operate a few millimetres away from the beam and have to be moved out of the beamline during injection of protons or antiprotons into the accelerator. The forward proton detector is not used in the work described in this thesis.

2.2.6 Luminosity Monitor

The luminosity monitor (LM) is designed to determine the Tevatron luminosity at the DØ interaction region. This is accomplished by detecting inelastic $p\bar{p}$ collisions with a dedicated detector. The LM also measures beam halo rates and makes fast measurements of the z-coordinate of the interaction vertex. The LM consists of two arrays of 24 plastic scintillation counters with PMT readout located at z = ± 140cm, and covers $2.7 < |\eta| < 4.4$. The luminosity is measured from the average number of inelastic collisions per beam crossing detected by the LM:

$$L = \frac{1}{\sigma_{p\bar{p},eff}} \frac{dN}{dt}(p\bar{p}) \tag{2.4}$$

where $\sigma_{p\bar{p},eff}$ is the effective cross-section for the LM that takes into account the acceptance and efficiency of the LM detector [42], [43]. The effective cross-section is derived as 60.7 ± 2.4 mb [44]. Over-counting from multiple $p\bar{p}$ interactions is taken into account by measuring the number of beam crossings with no collisions and using Poisson statistics to determine $\bar{N}_{LM}$. To distinguish $p\bar{p}$ interactions from the beam halo backgrounds, precise time-of-flight measurements are made of particles traveling at small angles with respect to the beams to estimate the z-coordinate of the interaction vertex. Beam halo particles traveling in the $\pm\hat{z}$ direction will have $z_0 \backsimeq \pm$ 140cm and are eliminated by a $|z|$ <100 cm requirement. The luminosity block is the fundamental unit of time for the luminosity measurement, and these are numbered monotonically. These are incremented every 60s or sooner depending upon various detector or Tevatron functions. This time period is short enough so that the instantaneous luminosity is constant during each luminosity block.

Performance and Status The overall efficiency for the detector is measured at 90.9 ± 1.8 %, with an error on integrated luminosities of 6.5% [45].

2.2.7 Trigger System and Data Acquisition System

At the Tevatron, $p\overline{p}$ collisions occur at a rate of 2.5MHz and it is not feasible to record and store events at this rate. Since most of the interactions are $p\overline{p}$ inelastic collisions and are not of interest, a triggering system has been developed to select the interesting physics events to be recorded. In addition to the luminosity monitor, there are three separate levels in the trigger system with each succeeding level examining fewer events but in greater detail and with more complexity. These levels are named Level 1, Level 2 and Level 3 and are shown as part of an overview of the trigger and data acquisition system in Figure 2.10. The luminosity monitor, sometimes referred to as *L0*, provides the first stage in rate reduction by rejecting events in which no hard $p\overline{p}$ interaction has taken place, thus reducing the L1 rate to that shown in Figure 2.10.

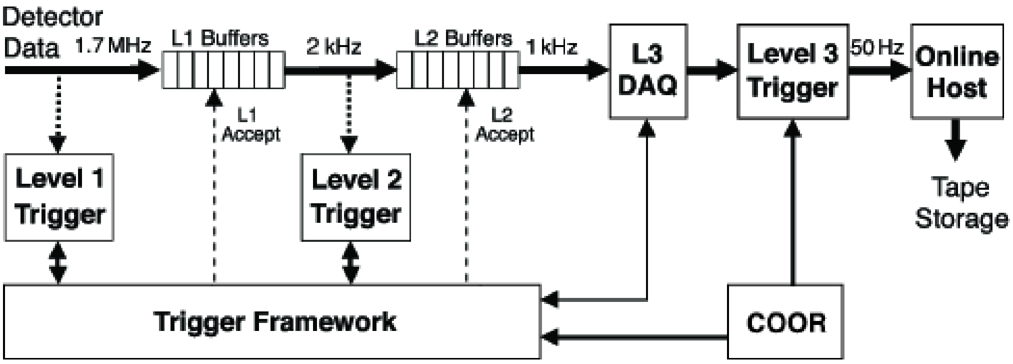

Figure 2.10: Overview of the DØ trigger and data acquisition systems

Level 1 The first stage, Level 1 (L1), is a collation of hardware triggers that are each based upon information from individual detector subsystems, with the exception of the muon trigger, which also needs information from the L1 track trigger. The L1 trigger examines every event. The individual triggers examine detector information and must pass this information to the *trigger framework (TFW)* within $3.5\mu s$ so that the decision whether or not to pass the event may be made. Figure 2.11 shows a block diagram of the L1 and L2 trigger systems and the flow of trigger related data.

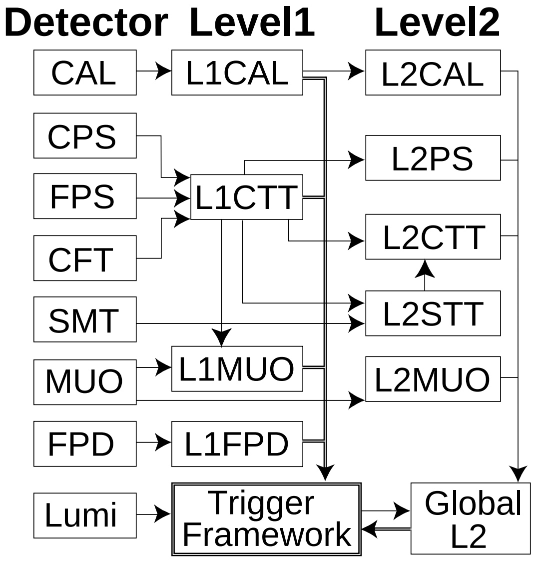

Figure 2.11: Block diagram of the DØ L1 and L2 trigger systems. The arrows show the flow of trigger related data

Level 2 If the TFW accepts an event, then it is digitized and sent to the L2 triggers. The system collects data from the front ends of the L1 trigger system in the first stage. In a second stage, it combines information across detectors to make very basic physics objects (see Section 2.2.8) . The buffers in L1 and L2 may store 32 and 16 events respectively, in order to minimize dead time. L2 has a maximum deadtime of 5% and a latency[8] of 100 μs . In contrast to L1, almost all of the processing in L2 is done by programmable processor boards.

---

[8] latency: time taken to make a decision

Level 3 The Level 3 trigger provides additional rejection of events to enrich the physics samples and to reduce the rate of events to be stored on tape to 50Hz for offline analysis. The accept rate is limited by the capabilities of and cost of data storage and offline computing. L3 is entirely software-based, reads out information from the entire detector and is run on a dedicated PC farm. Software tools build on the basic physics objects of L2 and decisions are using these objects and the relationships between them such as invariant mass. The filtering software can be changed as physics objectives or the operating parameters of the experiment change. The list of filters and their criteria is known as a trigger list and is assigned a version number.

2.2.8 Object Identification

This section briefly describes how different particles interact with the DØ detector. It also explains how they are measured, calibrated, and the terminology associated with them. It also describes certain detector objects that describe particle properties and are useful in analyses.

Electrons and photons

Electrons and positrons lose energy primarily through ionisation and bremsstrahlung [8]. Bremsstrahlung is the radiation emitted by a charged particle when accelerated transversely when passing through the field of atomic nuclei. This results in a shower of electron-positron pairs and photons. The photons themselves produce electron-positron pairs which further shower in the fields of the nuclei. For electrons above the critical energy of $E \approx 610 MeV/(1.2+Z)$ (where Z is the atomic number of the material), bremsstrahlung is the dominant process. Similarly, a shower is produced if the primary particle is a photon. A radiation length, χ_0, can be defined, over which the electron's energy will be reduced by a factor of 1/e [8]:

$$\chi_0 = \frac{716\mathrm{gcm}^{-2}A}{Z(Z+1)\ln(287/\sqrt{Z})} \tag{2.5}$$

The reconstruction of electrons and other EM objects starts in the calorimeter with clusters of energy deposits in cells in the EM layers (E_{EM}), and the first hadronic layer (E_{had}). A cluster is defined to be a group of 3×3 towers with energy greater than 500MeV [46]. The primary method to reconstruct electrons proceeds with a simple cone algorithm, with R=0.2, which is then applied to the seed-towers with $E_T > 1.5$GeV. At this point, photons and electrons may be differentiated since electrons are expected to interact with the tracking system, and photons are not. An electron track, which must have $p_T > 1.5$GeV, should point in the same direction as the electron's EM shower, and have a momentum that matches the energy of the shower. This is measured using a χ^2 match quantity [47]:

$$\chi^2_{spatial} = (\frac{\delta\phi}{\sigma_\phi})^2 + (\frac{\delta z}{\sigma_z})^2 + (\frac{E_T/p_T - 1}{\sigma_{E_T/p_T}})^2 \tag{2.6}$$

Electrons require a χ^2 probability of greater than 10^{-2}. The track now associated with the electron provides the θ and ϕ coordinates, and its total energy is taken from the calorimeter measurements; combining them gives the momentum. Without a track match, these coordinates are reconstructed from the primary vertex and the object's position within the third EM layer. Several additional variables are useful in characterising electrons and photons with high efficiency :

- **Isolation ($\mathbf{f}_{Iso}$)** Electrons and photons (and the showers they produce) are usually isolated from other particles in the calorimeter, unlike hadrons which are usually in jets of particles. The measure of this isolation, the *isolation fraction*, dependent on the total energy within the cone from all layers used, E_{tot}, is given by:

  $$f_{iso} = \frac{E_{tot}(R < 0.4) - E_{EM}(R < 0.2)}{E_{tot}(R < 0.2)} \tag{2.7}$$

  where R defines the size of the cone.

- **EM fraction, $\mathbf{f}_{EM}$** This uses the measurement of the energy deposited in the first hadronic layer, with the energy deposited in the EM layers to calculate the fraction of energy deposited in the EM calorimeter: EMF = E_{EM}/E_{tot}.

- **Coarse Hadronic Fraction, f$_{CH}$** In a similar way to f$_{EM}$, the coarse hadronic fraction is the fraction of energy deposited in the coarse hadronic layers.

- **Hot Fraction** This is the ratio of the transverse energies of the calorimeter tower with the highest energy, to the tower with the second highest energy. This cut, along with the following two variables, n90 and f90, are used to eliminate hot cells in the calorimeter that have been misidentified as EM objects.

- **n90** This is the total number of towers that make up 90% of the EM shower energy.

- **f90** Similar to n90, this is the fraction of the number of cells comprising 90% of the EM object energy.

- **HMatrix (*HMx8*)** This measures how similar the shower is to an electron shower. There are eight correlated observables used in this shower shape analysis that include EM energy fractions, the total EM energy, vertex z-position and transverse shower width in ϕ and z. The 8×8 covariance matrix is a measure of the shower similarity. The HMatrix is the inverse of this covariance matrix. It is calculated for each tower in η [48].

The offline electron reconstruction efficiencies in data, calculated from $Z \rightarrow e^+e^-$ events in the CC is 84.1% ± 0.9%, and in the EC, 91.5% ± 1.3% [49]. Other types of reconstructed electrons that are less commonly used are the road and SEM electrons, and these are described in Section 4.3.

There are several sources of background which may be mistakenly identified as electrons [50]

- π_0 showers which overlap with a track from a charged particle.

- Photons which convert to e^+e^-pairs.

- $\pi^\pm$ which undergo charge exchange in the detector material.

- Fluctuations of hadronic shower shapes.

Muon Quality	**Tight**	**Medium**	**Loose**	
A layer wire	> 2 hits	> 2 hits	> 2 hits	-
A layer scintillator	1 hit	1 hit	1 hit	-
BC layer wire	> 3 hits	> 2 hits	-	> 2 hits
BC layer scintillator	> 1 hit	> 1 hit	-	> 1 hit
Central Track Match	A and BC segments matched	A or BC segments or no match	A matched only	BC matched only
Efficiency for muon in central system	0.599 ± 0.005	0.774 ± 0.005	0.897 ± 0.003	

Table 2.4: Selection criteria for tight, medium and loose muons

Muons

Muons interact very little with the detector and have much greater penetrating power [8] because of their higher mass

When reconstructing muons, DØ makes use of the muon detector and the central tracker, and to a small extent, the calorimeter [51]. The muon system provides unambiguous muon identification and an approximate momentum measurement. The tracking system provides a more accurate momentum measurement and finds muon tracks efficiently. The best quality muons, *global* muons, come from muons detected in the muon detector and then matched to a track from the central tracker. Muons detected in the muon detector only are called *local* muons. The calorimeter provides confirmation of a muon through detection of its MIP signature.

Additional requirements on muons are that they are within $|\eta|$ <2, that the time between the beam crossing and an A layer hit is <10ns (<15ns for a BC layer hit), the p_T >4GeV, and that the distance of closest approach in z with the primary vertex is <5cm. The selection criteria for DØ 'tight', 'medium' and 'loose' muons are listed in Table 2.4.

Jets and hadrons

In hard $p\overline{p}$ collisions, final state partons are produced which hadronise into collimated streams of particles, labelled *jets*. These are composed predominantly of photons, pions and kaons and they are detected when the particles deposit energy in the calorimeter cells. Jets are then reconstructed from these energy deposits using the D0Run II jet cone algorithm [52], [53]. To relate the measured jet energy back to the energy of the final state partons, a *jet energy scale* is derived to correct for the distortions to the measured energy by various detector and physics effects.

Hadrons interact with the nuclei of the detector. A length scale, the *interaction length*[8], similar to the radiation length of electrons, is given approximately by:

$$\lambda_I \approx 35A^{\frac{1}{3}}gcm^{-2} \tag{2.8}$$

Hadrons produce showers of hadronic particles, mostly pions and nucleons, which in turn interact with the nuclei of the detector producing a cascade. These showers are measured as *jets* within the calorimeter; clustering algorithms group the cells with energy deposits from the EM and hadronic layers. Most jets at DØ are reconstructed using the Run II Cone algorithm [54] Cones have their origins at an interaction point and extend outwards containing the jet particles. They have a fixed $\triangle R$ in $\eta - \phi$ space. The cone jet corresponds to a "stable" orientation of the cone around energy clusters in the calorimeter. A seed-based algorithm is applied which uses seeds and midpoints of seeds as starting points for finding these stable cones. The seeds are preclusters of calorimeter towers, instead of single (out of 5000) towers, which reduce the time taken to find all stable cones. The Run II cone algorithm is divided into three stages: clustering, addition of midpoints, and merging-splitting. The clustering stage is based on the Simple Cone Algorithm and it forms the preclusters of towers which are used to form *protojets*. Following this, protojets are also searched for around the midpoints of any two already existing protojets if they are more than $\triangle R_{cone}$ (usually R=0.5) apart. Lastly, as protojets often share items (clusters) of energy, cones are merged or split according to how the clusters are shared. This is to avoid double counting of energy. If a protojet shares one or more items with another protojet and these represent 50% or more of the energy of the other jet, then the shared clusters are assigned to that other jet, and the first jet is removed. If the fraction of shared energy is smaller than 50% of either jet, then the two jets are split and the items are assigned to the nearest jets.

The jet algorithm is not perfect, for example some of the energy of the jet may lie outside the cone, the cone may contain energy from calorimeter noise etc. So a correction is made for these effects and an overall calorimeter response to jets is derived. Together, along with a number of other, smaller corrections, make up the jet energy scale which is discussed in detail in Chapter 3. The jet energy resolution is similar in form to the calorimeter resolution and is measured from (γ + jets) and dijet data [55]:

$$\left(\frac{\sigma_{E_T}}{E_T}\right)^2 = \frac{N}{E_T} \oplus \frac{S}{\sqrt{E_T}} \oplus C \tag{2.9}$$

where C is a correction for the jet energy scale, S is a correction for jet energy that ends up outside the jet cone, and N is due to instrumental noise and other detector effects. The efficiency of both identifying and reconstructing a jet depends on the calorimeter region and is as high as 99% in the central region, and as low as 95% in the ICR, and is 98% in the end caps.

Detector Objects

$\not\!\!E_T$, p_T and neutrinos Since energy must be conserved in the collisions inside the detector, any missing energy is a sign of neutrinos or other non-interacting particles. We often use only the components of energy and momenta perpendicular to the z-axis because it is difficult to measure accurately the components of these quantities when the particles escape down the beam-pipe in the z-direction. So it is the missing transverse energy that we use to measure non-interacting particles. The missing transverse energy, $\not\!\!E_T$, is the negative magnitude of the vector sum of the calorimeter tower transverse energies and is defined as:

$$\not\!\!E_T = -(\sum_i (E_{xi}), \sum_i (E_{yi})) \tag{2.10}$$

where E_{xi} and E_{yi} are defined the x and y components of the tower energies within $|\eta| < 4.5$. Before the $\not\!\!E_T$ can be used in an analysis, it must be adjusted to account for the corrections that are applied to the other physics objects in the event [56]: noisy cells in the coarse hadron calorimeter, the EM scale, the jet energy scale, and for muons detected only in the muon system. Where jets are concerned, the scalar hadronic transverse energy, H_T, is sometimes used. This is the scalar sum of the p_T of the good jets in an event. Also used is the missing H_T, $\not{H}_T$, which is the negative magnitude of the vector sum of the jet transverse energies.

Tracks and Vertices

Reconstructed tracks and vertices are an essential part in the identification of all of the physics objects in an event [57], [58]:

Object	Track Requirements
Electrons	Require a track and that its momentum is matched to the calorimeter energy
Photons	Require the absence of a track
Muons	Require the matching tracks in the central tracker and the muon system. Their momentum is measured by combining these
Taus	These are jets with one or three tracks
B-quarks	Identified by a displaced vertex from the beam line

Furthermore, tracks provide the vertex point for quark and gluon jets so their direction can be determined more precisely. The correct identification of the vertex (or vertices) is essential for calculating the missing transverse energy associated with neutrinos.

Within the tracking system, DØ currently uses the AATrack tracking algorithm to reconstruct the trajectories of charged particles from the hits they leave in the SMT and CFT, combining the 2D and 3D position information from both of them [59] [60]. It starts by constructing track hypotheses from three SMT hits and extrapolating these hypotheses out from the centre of the detector through the CFT. Any further tracking hits close to the hypotheses are matched to the track using a χ^2 cut. The track hypotheses are then ordered according to the number of hits and other quality criteria, and considered in turn to see if they share too many hits with other tracks. Those sharing above a certain number are eliminated, and the rest are declared tracks. A more detailed explanation of the tracking can be found in reference [61]. Once tracks have been found, they are extrapolated through the detector and linked to physics objects using the Global Tracking algorithm, [60]. The tracking efficiency depends on the location of the track within the tracking system and the p_T of the particle. For a track with p_T above 10GeV, the efficiency is between 96% and 99%, with a fake rate of around 2%. For tracks below 10GeV, the efficiency is approximately 92% with a fake rate of about 1% [62].

At DØ vertex detection depends on track identification, and there are two types of vertices that are constructed in each event: a primary vertex, and secondary vertices. The primary vertex is the main interaction point of the collision and must lie along the beam line within $|z| < 60cm$. It is reconstructed from good quality tracks only with an average efficiency of 98%, measured on multijet data. The primary vertex may be located to within $15\mu m$ in x,y and to within $30\mu m$ in z.

The B-meson has a relatively long lifetime so it may travel far enough before decaying that its decay vertex may be resolved by the tracking system. This decay vertex is called the secondary vertex and is found using the secondary vertex tagger (SVT) algorithm [63], [64]. The identification of jets originating from b-quarks is called b-tagging and there are several other algorithms for identifying b-jets by assigning a probability to the jet that came from a b-quark. This process is described in more detail in Chapter 5.

DØ Software and Terminology

DØ analysis and processing software versions are referred to by their release number in the format pXX, or pXX.XX.XX, for example p14, p16.07.00 [65]. A change in release version marks major changes to the software, or introduction of new algorithms or a new set of reprocessing. Any specific corrections for problems discovered, such as bugs in the software, or corrections for hardware problems may be named in the same fashion, or be referred to by the package name, such as d0correct [66]. Most of the analysis at DØ is carried out on data stored in the thumbnail format [67] which requires about 10kb per event.

The trigger system uses a single version of the trigger list at any one time.

These trigger lists are updated to take into account changing physics programmes, increasing luminosity and the aging of the detector. These are labelled v12, v13 etc [68].

2.2.9 Overall Current Detector Performance and Status

The DØ Run II daily data taking efficiency is shown in Figure 2.12(a), and Figure 2.12(b) shows the luminosity delivered to and recorded by DØ to date. Since the start of Run II, DØ has recorded 1.3fb^{-1} data, and has operated at a daily efficiency around 85% for most of Run II. The increased luminosities of Run IIb required upgrades to the silicon tracker and the trigger system and in 2002 upgrade programmes were approved. The upgrades were installed at the end of 2005 and the Run IIb detector upgrades are described in detail in [33]. The trigger system upgrades included a replacement L1 Calorimeter module, a new module that uses both tracking and calorimeter information, more L2 modules and processors, and additional L3 processors and online storage. An additional layer, *Layer 0*, was also added to the silicon tracker at about 1.6cm from the beam line, as mentioned earlier in the chapter.

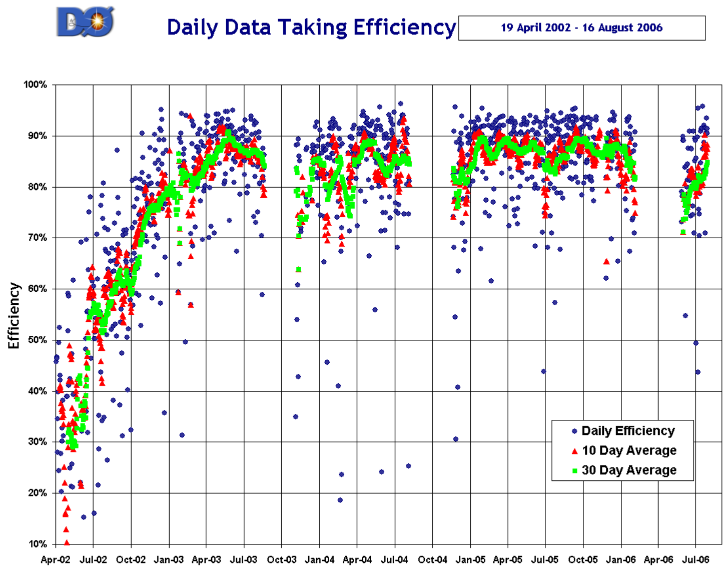

(a) Daily data taking efficiency

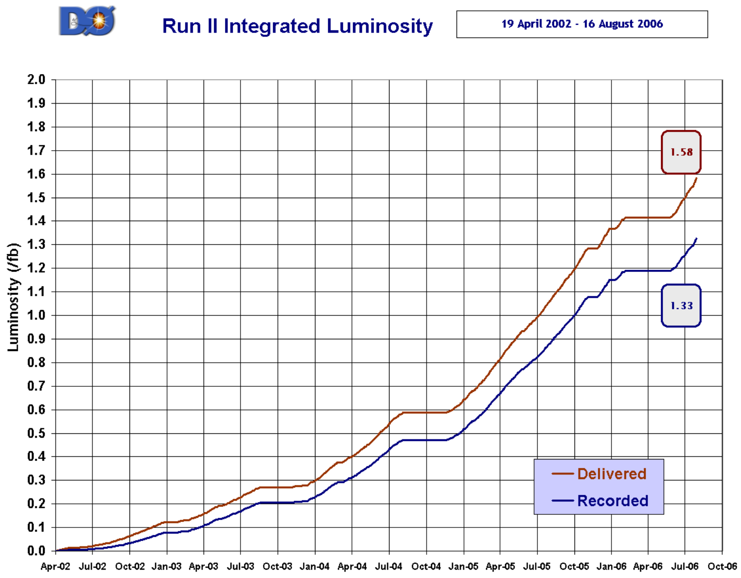

(b) Integrated luminosity delivered and recorded

Figure 2.12: The DØ detector performance for Run II

Chapter 3

The Jet Energy Scale

3.1 Introduction

Almost all physics programmes at DØ involve jets so it is important that their characteristics are well understood and that their energies and other properties are accurately measured. For example, the Tevatron is the only collider where top quarks are produced directly and currently the errors from the jet energy scale dominate the error in the top mass measurement [69]. The Jet Energy Scale (JES) is a calibration that allows the energies of reconstructed collider jets to be related back to those of the final state particle jets[1], on average.

In Run I, the jet energy scale was based on transverse energy conservation in (γ + jets) events. Now, in Run II, with the larger datasets, the jet energy scale can be derived using Z(e^+e^-)+jets events. In this chapter, the calorimeter response to jets is derived using p14 MC and Pass 2[2] data events and compared to the official response from (γ + jets) events. This formed part of the verification of version 4.2 [70] of the official DØ JES. Before the (Z + jets) response was calculated, some

---

[1] The *particle* level jet energy is defined as the jet energy found from final state partons using a cone algorithm as described in Chapter 2. Particle jets cannot be seen in data, but they can be defined in Monte Carlo samples.

[2] Pass 2 denotes the version of data reprocessing and the corrections applied. See `http://www-d0.fnal.gov/Run2Physics/cs/skimming/pass2.html`.

other, independent corrections were made to the jets using v4.2 of the jet energy scale (see Section 3.3.2 for more detail). Closure tests are also performed on the (γ + jets) JES versions 4.2 (and 5.1) using (Z + jets) events. The closure tests using JES v4.2 are shown in this chapter. This work was carried out in 2003 and 2004 when DØ had collected only about 140pb^{-1} of data.

3.2 The Jet Energy Scale

Before measurement, the jet energy is affected primarily by the calorimeter response to different particles. Although EM and hadronic particles interact with the calorimeter though different physics processes, the calorimeter response is nearly compensating. The jet energy is also distorted by energy losses in uninstrumented regions, uranium decays leaving energy deposits in the argon, spectator interactions, and reconstruction effects from the cone algorithm. The response for (γ + jets) events is obtained by using the Missing E$_T$ Projection Fraction Method (MPFM) which was first used in Run I and is described in [71]. Since the topology of (Z + jets) events is similar to that of (γ + jets) events, the same procedure can be used. The JES is implemented in a software package, *jetcorr* [72], which calculates the jet corrections 'on the fly' during an analysis and also provides statistical and systematic errors for the jet energies.

The factors affecting jet energies are summarized in Equation 3.1. This shows the relationship of the measured energy of the jet in the calorimeter (E_{jet}^{meas}) to the particle jet energy (E_{jet}^{ptl}) as a function of several variables including luminosity, L, and jet η:

$$E_{jet}^{ptl} = \frac{E_{jet}^{meas} - E_o(R,\eta,L)}{R_{jet}(R,\eta,L)R_{cone}(R,\eta,L)} \tag{3.1}$$

Where:

- E_o is the offset energy. This is any energy measured as part of the jet not due to the hard interaction itself.

- R_{jet} is the calorimeter response to the hadronic jet known as the *jet energy* *response* and this is derived in the next section.

- R_{cone} is the fraction of the particle jet energy that is contained within the jet reconstruction cone. This is corrected for by the *showering* correction.

Offset Correction The offset correction, $E_o(R, \eta, \mathcal{L})$, includes any energy that does not come directly from the hard interaction itself, such as uranium noise, remains of previous bunch crossings (*pile-up* energy), additional interactions, and the underlying physics event[3]. This is dependent on the luminosity, $\mathcal{L}$, and increases with the jet cone size, R. E_o is also dependent on the physics η. The total offset energy correction can be considered as the sum:

$$\begin{aligned} E_o &= (1 + \langle E_{ZB} \rangle) E_{ue} + E_{noise} + E_{pile} \\ &= E_{ue} + \langle N_{ZB} \rangle E_{ue} + E_{noise} + E_{pile} \end{aligned} \tag{3.2}$$

where $\langle N_{ZB} \rangle$ is the average number of hard core interactions in a zero-bias event, E_{ue} is the energy from the underlying physics event, $\langle N_{ZB} \rangle E_{ue}$ is the energy associated with additional $p\overline{p}$ interactions, E_{noise} represents the noise from uranium decay, and E_{pile} is the pile-up energy. $\langle N_{ZB} \rangle$ may be calculated from the probability, which follows a Poisson distribution, of a hard core collision at a given luminosity.

Showering Correction The showering correction compensates for the fraction of jet energy that falls outside the reconstruction cone as the particles interact with the calorimeter. This also corrects for energy that originates from outside the cone, but that ends up inside, perhaps bent by the magnetic field. The showering correction is derived from both MC and data using jet energy density profiles. It is not possible to directly determine the instrumental showering contribution because energy left outside the cone that is part of the jet may also be associated with gluon emission or fragmentation at the particle level (*physics out-of-cone*). This contribution must be determined from Monte Carlo events using information about the particles within

---

[3] Underlying physics event: defined as the energy coming from spectators to the hard proton interaction.

the jet. The final showering corrections used in the JES corrections are the difference between the total showering and physics out-of-cone showering contribution.

There are three stages to the showering correction calculation:

- The jet energy density is calculated in rings of 0.1 in the $\eta \times \phi$ plane around the jet direction as a function of the radial distance from the jet direction.
- Subtraction of a baseline energy density due to energy associated to the noise and underlying event activities.
- The out-of-cone showering corrections are derived by computing the amount of energy outside the cone R = 0.5 or 0.7.

Figure 3.1 shows the showering profile for central calorimeter jets for R=0.5 in the data after offset and baseline energy subtraction. Systematic errors are estimated by looking at the difference between the correction derived using photon+jet samples and dijet samples.

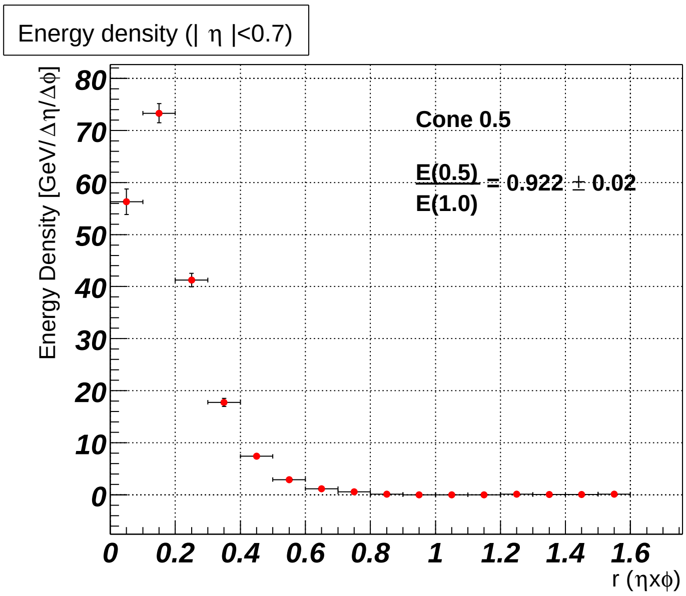

Figure 3.1: Showering profile for central calorimeter jets of R=0.5 in the data, after offset and baseline energy subtraction

3.3 Jet Response

3.3.1 Missing E_T Projection Fraction Method

The jet energy response (R_{jet}) is derived using (γ + jets) or (Z + jets) data and Monte Carlo events where there is one photon balanced in p_T by one or more jets, relying on the much more accurately-calibrated measurement of the photon and electron energy scales, the fact that we can measure jet direction very well, and that in a perfect calorimeter there should be no missing energy perpendicular to the $p\overline{p}$ collision direction. Any non-zero missing transverse energy would usually indicate the presence of a neutrino or a muon which has not deposited its energy in the calorimeter. Instead, as the calorimeter response is imperfect, a non-zero $\not\!\!E_T$ measures the overall imbalance of transverse energy in the calorimeter due to different responses to photons and jets. This can be used to measure the response, R_{recoil}, relative to the precisely calibrated photon response, which is assumed to be close to the particle level response. Here, R_{recoil} is the calorimeter response to *jets* and includes already the showering and offset energy corrections. If there is only a single photon (or Z boson) and a single jet in the event, and if there were no energy distortions from showering or offset energies, then R_{recoil} is exactly $E_{T,jet}^{meas}/E_{T,jet}^{particle}$. For events in which the photons are back-to-back[4], then $R_{recoil} \approx R_{jet}$. In ($\gamma$ + jets) events, the photon ($\overrightarrow{E}_{T\gamma}$)[5] and recoil transverse energies ($\overrightarrow{E}_{T,recoil}$) satisfy:

$$\overrightarrow{E}_{T,\gamma} + \overrightarrow{E}_{T,recoil} = 0 \qquad (3.3)$$

However, in reality, the responses are both less than unity, and the resulting deficit in E_T is the measured $\not\!\!E_T$:

$$\overrightarrow{E}_{T,\gamma}^{meas} + \overrightarrow{E}_{T,recoil}^{meas} = -\overrightarrow{\not\!\!E_T}^{meas} \qquad (3.4)$$

where $\overrightarrow{E}_{T,\gamma}^{meas} = R_{em}\overrightarrow{E}_{T,\gamma}$ and $\overrightarrow{E}_{T,recoil}^{meas} = R_{recoil}\overrightarrow{E}_{T,recoil}$.

---

[4] back-to-back: where the azimuthal angle between the objects is π

[5] Since the MPFM is the same for both (γ + jets) and (Z + jets) events, in this section, γ is used interchangeably with Z

The EM scale is used to correct $\overrightarrow{E}^{meas}_{T,\gamma}$ and so Equation 3.4 becomes:

$$\overrightarrow{E}_{T,\gamma} + R_{recoil}\overrightarrow{E}_{T,recoil} = -\overrightarrow{\not{E}_T} \tag{3.5}$$

$$\overrightarrow{E}_{T,\gamma} + R_{recoil}\hat{n}_{T,\gamma}\overrightarrow{E}_{T,recoil} = -\hat{n}_T\overrightarrow{\not{E}_T} \tag{3.6}$$

$$1 + R_{recoil}\frac{\hat{n}_{T,\gamma}\overrightarrow{E}_{T,recoil}}{\overrightarrow{E}_{T,\gamma}} = -\frac{\hat{n}_T\overrightarrow{\not{E}_T}}{E_{T,\gamma}} \tag{3.7}$$

where $\hat{n}_{T,\gamma} = \overrightarrow{E}_{T,\gamma}/|\overrightarrow{E}_{T,\gamma}|$ so that Equation 3.3 can be rewritten as:

$$R_{recoil} = 1 + \frac{\overrightarrow{\not{E}_T}\cdot\hat{n}_{T,\gamma}}{E_{T,\gamma}} \tag{3.8}$$

The topology of (Z + jets) events (where the Z decays to an e^+e^-pair) is similar to that of (γ + jets) events, the missing E_T projection fraction method may thus be used to derive the response, substituting $\overrightarrow{E}_{T,Z}$ for $\overrightarrow{E}_{T\gamma}$ in Equations 3.3 to 3.8.

The Energy Estimator, E′

The response is dependent on the jet energy, not its transverse component because the EM-hadronic response ratio and the particle composition of the jets are energy dependent. However, it is difficult to measure directly R_{jet} as a function of E^{meas}_{jet} as E^{meas}_{jet} is biased by many things including trigger and reconstruction effects, event topology, and energy resolutions for photons/electrons and jets. Instead, the response may be binned in the better-measured quantity, the *energy estimator*, E′:

$$E' = E_{T\gamma}\cdot\cosh(\eta) \tag{3.9}$$

where $E_{T\gamma}$ includes the electromagnetic scale correction. This helps reduce the biases and energy smearing effects as both the $E_{T\gamma}$ and the jet η can be measured more precisely than E^{meas}_{jet}. Figures 3.2(a) and 3.2(b) show the $E' \rightarrow E^{meas}_{jet}$ mapping for data and MC event samples respectively, divided into the three calorimeter regions, CC, EC, and ICR. The mapping of actual jet energy to E′ varies between the three regions.

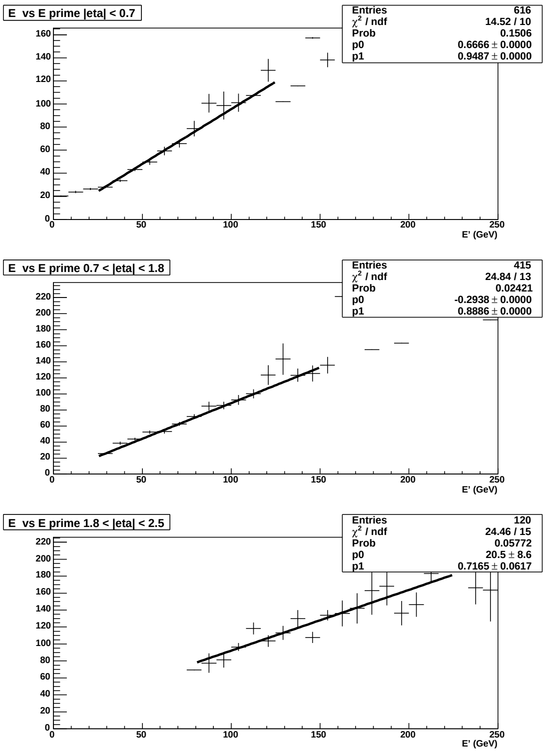

(a) Data

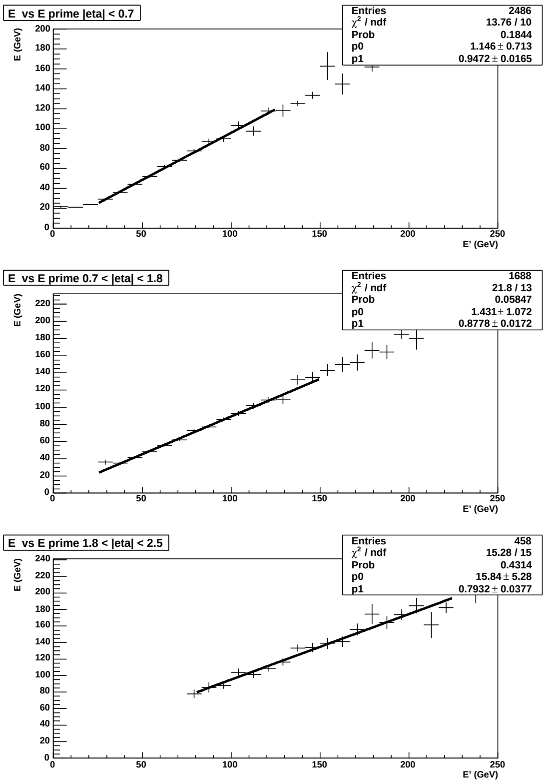

(b) Monte Carlo

Figure 3.2: (Z + jets) E-E′ mappings, top to bottom: CC, ICR, EC.

Event Samples and Selection

The calorimeter response to jets in Z(e^+e^-) + jets events was calculated with Monte Carlo and Pass 2 data, using software version p14 [73], and d0correct[6] v8.0 [66]. For data, 15 million Pass 2 events were used, skimmed so that each event contains two EM objects with p_T >7GeV. Closure tests were performed on the jet energy scale given in the v6.0 JetCorr package. A good run list was used to eliminate bad events which may contain information from noisy or malfunctioning subdetectors. For the Monte Carlo studies, 289,000 inclusive Z+jet(s) plate[7] events generated by Pythia (v.6.155 [74]), with a kinematical cut on the Z mass of 60GeV $< m_Z <$130GeV were used.

The response is measured from simulated and data event samples that have been selected using a set of criteria designed to pick 'true' (Z + jets) events but remove systematic biases and unwanted backgrounds. The cuts are applied in three stages. Firstly, general event cuts are applied to choose 'clean' events, secondly cuts are applied to remove backgrounds, and lastly cuts are applied to ensure that the event has the correct topology. For a detailed explanation of the selection criteria used in this section, refer to Section 2.2.8. The following criteria were applied to both data and Monte Carlo events, and the cutflow tables are given in Table 3.1.

General Cuts Since the Z boson in each event is reconstructed from two electrons[8] emitted back-to-back in the Z rest frame, each event must have:

- Two EM objects, both of which must be identified as an EM object with a track match.
- The EM objects must have opposite charge signs to ensure that it is an e^+e^-pair.

---

[6] This is a software package that carries out all the post processing (corrections, certifications) for EM, muon, jet and $\not\!\!E_T$ objects.

[7] Plate MC events are those where the calorimeter has been simulated as a series of uranium and argon plates.

[8] In this section *electron* is used interchangeably with positron, unless specified otherwise

Furthermore, events must be fully within the fiducial regions of the calorimeter. To avoid problems associated with measuring jet energies at low E_T (*low-E_T bias*), only events with E_T >25GeV are used. Lastly, primary vertices at large distances from the detector centre can distort E_T measurements so it is required that the primary vertex must be within $|z|$ <50cm and that it must have at least 5 tracks associated with it.

Background cuts The official p14 recommended object-quality selection cuts[9] from the EM Object [75] and Jet Identification Working Groups [76] were applied to ensure that a good sample of electrons and jets was collected:

Electrons

- $f_{EM} > 0.9$
- $f_{Iso} < 0.15$
- HMx8 < 20

Jets

- $0.05 < f_{EM} < 0.9$
- $f_{CH} < 0.4$
- Hot fraction < 10.0
- n90 > 1.0
- f90(= n90/number of towers):

f90 < (0.8 - 0.5×f_{CH})or f_{CH} <0.1

The jets were reconstructed with the cone algorithm as described in Section 2.2.8, using R=0.5 cones, and with v1.2 of the recommended cuts. The electrons were simple cone electrons, corrected using the p14 electron energy scale[10]. The background is made up of instrumental backgrounds where highly EM jets are mistaken for electron showers, and physics backgrounds from other similar decay channels. To eliminate instrumental backgrounds, a cut is placed on the electrons to ensure they are well-isolated from both other EM objects and highly electromagnetic jets (mostly π^0 jets). Jets with a high EM component bias the measurement of R_{jet} and they may be identified and rejected using a cut on the HMatrix value for the EM object. This cut removes many events but discriminates well between

---

[9] For definitions of physics and detector objects please refer to Chapter 2.

[10] This EM scale correction is also included in the $\not\!\!E_T$ in each event.

EM showers from electrons and highly EM jets. The jet must be within the CC ($\eta < 0.8$) or the EC ($1.8 < \eta < 2.5$).

Topology and Multiple Interaction Cuts The derivation of R_{recoil} in Section 3.3.1 was based on a two-body process involving a single photon (or Z boson) recoiling against a single jet. However, when measuring R_{jet} , events may contain more than one jet, as well as energy clusters which never get reconstructed as jets. These variations in topology contribute a systematic error to the measurement of R_{jet} [71]. A cut was placed on each event requiring that the azimuthal angle between the Z boson and the leading jet ($\triangle\phi$) is greater than 3.0 radians. This is motivated by the equivalent $\triangle\phi$ cut used in the (γ + jets) derived response. However, the variation in response for (Z + jets) events with $2.8 < \triangle\phi < 3.1$ is examined later. In addition to multiple jets in an event, there may be multiple interaction vertices, although usually only the 'primary' vertex will produce high-E_T objects. On average, if a jet has been incorrectly allocated to the wrong interaction vertex, it will have a higher η than it should do. This will make its value of E$'$ higher and its E_T lower. This increases the measured $\not{E}_T$ in the direction of the jet and so the value of R_{jet} for the event is lowered. This effect is dependent on luminosity, but is not investigated in this response calculation. To remove this effect, it is required that in each event there is only one 'primary' vertex.

Physics Background Cuts The physics backgrounds to (Z + jets) events include Drell-Yan, (γ + jets) , and W$\rightarrow e\nu$ events. In the case of (γ + jets) events, and most Drell-Yan events, the dielectron invariant mass will not be that of the Z boson and so a cut is placed on the dielectron mass of $82.6\text{GeV} < m_{ee} < 102.6\text{GeV}$. Background events with a neutrino will have a high $\not{E}_T$ in the direction of the neutrino and may be eliminated both through the general $\not{E}_T$ cut, requiring track matches, and requiring both EM objects in each event to be reconstructed by the calorimeter.

Selection Criteria	**Monte Carlo # events remaining**	**Data # events remaining**
Total number of events	289,000	14,893,480
Vertex event selection	174,366	9,278,022
EM selection	124,347	3,566,156
$\|\eta\| < 2.5$	113,221	3,373,623
EM objects in the fiducial region	165,049	5,527,559
Number of events after em p_T cut	78,183	54,180
Number after m_{ee} cut	66,428	16,606
Number of leading jets after jet selection	10,542	2923
Topology cuts ($\Delta\phi$ (Z, leading jet))	1581	1131
Events in the CC	620	452
Events in the EC	222	148

Table 3.1: Number of data and MC events passing the selection criteria

Selection Criteria Results

Table 3.1 shows the initial numbers of MC and data events used and the numbers remaining after the selection criteria have been applied.

3.3.2 Jet Response Calculation

The Missing Transverse Energy Correction

The $\not{E}_T$ in the event is defined as the negative vector sum of the calorimeter cell energies (i) in x and y:

$$\not{E}_T = -(\sum_i E_{x_i}, \sum_i E_{y_i}) \tag{3.10}$$

The p_T of the Z boson is the vector sum of the E_T of the electron and the positron. However, the cell-by-cell information from the calorimeter is not stored after each event and so any corrections (e.g. for EM energy scale, showering and offset energy) to the reconstructed objects must be recalculated. Given that the energy corrections are not calculated for calorimeter cells but for the reconstructed physics objects , the recalculated corrected $\not{E}_T$, $\not{E}_T^{corr}$, is calculated by vector subtraction of an amount equal to the correction to the objects:

$$\not{E}_T^{corr} = \not{E}_T + \sum_{obj} (p_{T_{obj}}^{meas} - p_{T_{obj}}^{corr}) \tag{3.11}$$

Now the $\not{E}_T$ is dependent on the method used to reconstruct the physics objects and on the way that their energy components are calculated.

Energy Dependence of the Response for both Data and MC

Before the response was calculated, the EM objects for the EM energy scale, and the showering and offset energy corrections only were made to the jets using version 4.2 of the official jet energy scale. The response was binned in E′ and this is shown in Figure 3.3 for MC in the EC. Figures A.2, A.1 and A.3 show the equivalent plots for MC (CC) and data (CC and EC).

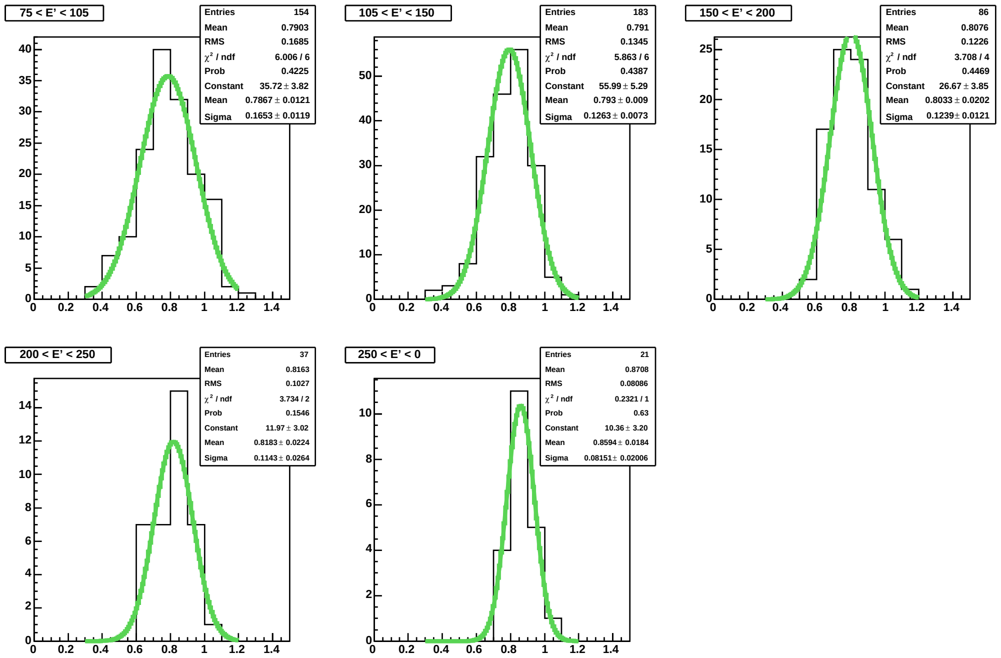

Figure 3.3: Monte Carlo response for the EC, binned in E′ for 75GeV<E′ <105GeV (top left) to E′ >250GeV (bottom right).

The response histograms were fitted with Gaussian functions, the mean and sigma of each fit giving the R_{jet} and the error on R_{jet} respectively. Using the appropriate $E' - E_{jet}$ mapping (Figures 3.2(a) and 3.2(b)), the average response is mapped to E, and plotted against both E' and E_{jet} in Figures 3.4(a) and 3.4(b). There is a low-E_T bias that can be seen in the curve at low E′ of the E-E′ mapping in the CC in all response plots and this is discussed later in this section. A quadratic logarithmic function of the following form is fitted to the response:

$$R_{jet} = a + b\log(\frac{E_{det}}{E_0}) + c\log^2(\frac{E_{det}}{E_0}) \tag{3.12}$$

This form was used in Run I and is motivated by consideration for the variation of the particle content of jets with energy.

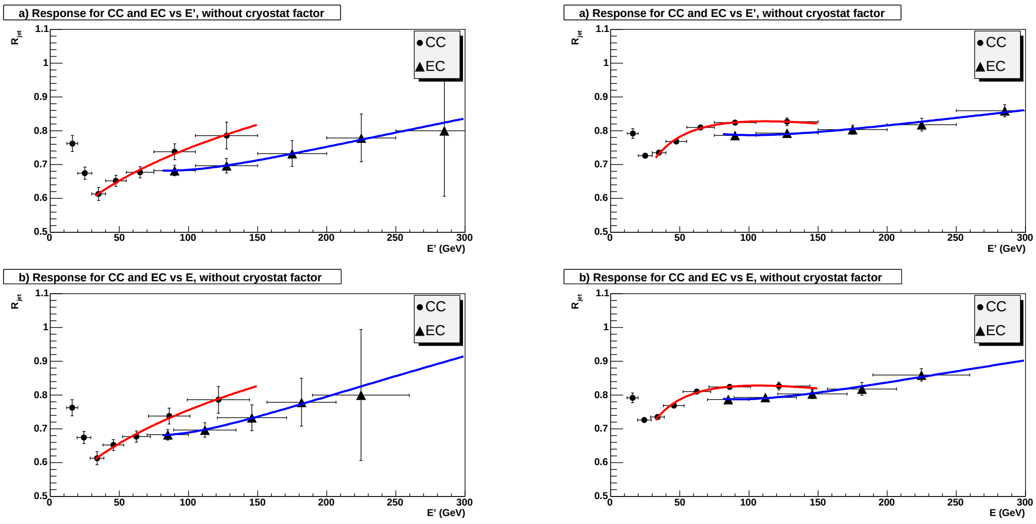

(a) Data

(b) Monte Carlo

Figure 3.4: Response ($\Delta\phi \geq 3.0$) with a quadratic log fit as motivated in the text, before cryostat factor correction against a) E′(upper) and b) E (lower)

It can be seen that the response to jets is different in the CC and the EC, with a large variation over the ICR (corresponding to the overlap region). In order that the binned response histograms in the CC may be combined with the binned response histograms in the EC, a cryostat factor is calculated to scale the EC response to that of the CC.

The Cryostat Factor The intercryostat region of the calorimeter (0.8< $|\eta|$ <1.6) is poorly covered by calorimeter instrumentation and is non-uniform, meaning that much particle energy is lost into support structures, cryostat walls and module endplates. Furthermore, there is no EM calorimetry in the range 1.2< $|\eta|$ <1.4 and the total thickness falls from about 20 interaction lengths to approximately 6. The cryostat factor is defined as the ratio of the response to jets in the EC to that in the CC:

$$F_{cry} = \frac{R_{EC}}{R_{CC}} \tag{3.13}$$

The CC and the EC are similarly constructed, so the data that overlap in E′ between the CC and the EC are used to calculate this factor. F_{cry} is calculated as a simple ratio of the response in the overlapping bins in the energy range 60GeV< E' <180GeV. The cryostat factor is plotted in Figure 3.5 for data (left) and Monte Carlo (right). Normally, in data only, one would calculate this factor separately for the north and south EC regions, as is done in the (γ + jets) jet energy scale, but there are insufficient statistics to do this for (Z + jets) events. For MC, the ECN and ECS are not modelled separately and so F_{cry} is the same for both regions.

The response after the cryostat factor has been applied is given in Figures 3.6(a) and 3.6(b).

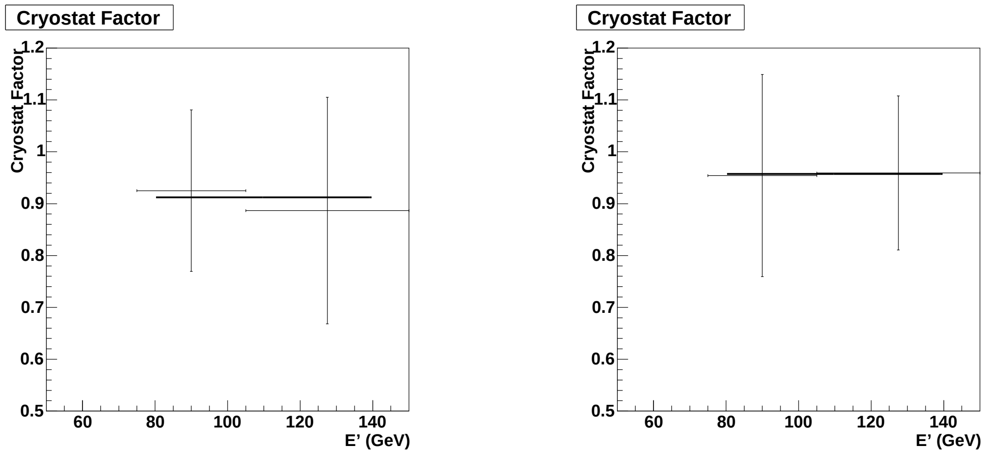

(a) Data

(b) Monte Carlo

Figure 3.5: Cryostat Factor

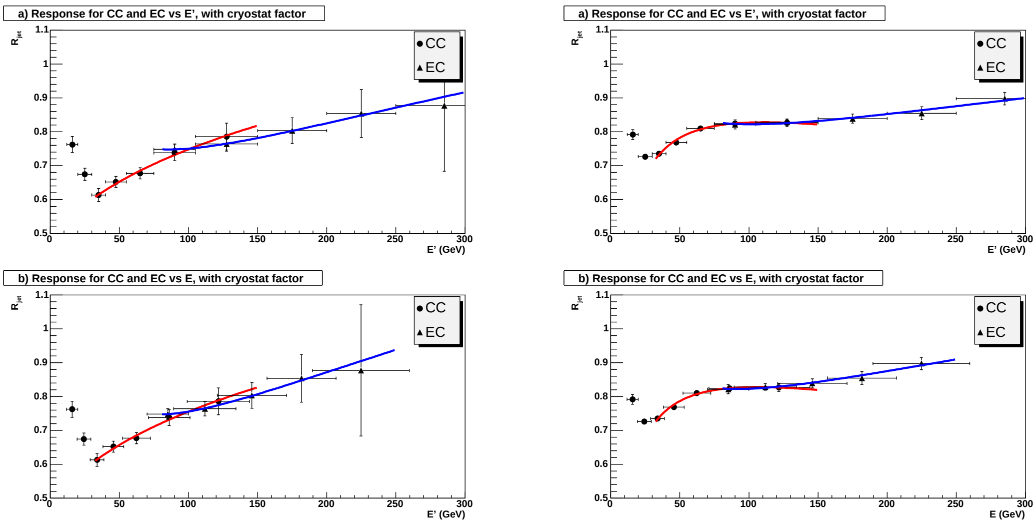

(a) Data (b) Monte Carlo

Figure 3.6: Response ($\Delta\phi \geq 3.0$) with a quadratic log fit as motivated in the text, after cryostat factor correction against a) E′ (upper) and b) E (lower)

The Low E_T Bias

At low energies ($E_{jet} < 25GeV$), the response to jets becomes difficult to measure due to a combination of the 8GeV threshold on jet reconstruction and the rapidly worsening (towards low energies) jet resolution. The measured response is biased when the energies of low-energy jets, which fluctuate more, fluctuate below the minimum E_T requirement. This means that low-energy jets are often not reconstructed, biasing the average E_T of low energy jets artificially high. This, in turn, shifts the average $\not\!\!E_T$ to lower values giving a response biased to higher values. It is possible to derive a response for the low energy region by measuring the calorimeter response to energy deposits as a whole; this method was used in Run I [71]. This method eliminates the need to require a reconstructed jet in the event. The effect of the bias is then the ratio:

$$R_{bias} = \frac{R_{jet(\geq 1jet)}}{R_{jet(nojetrequired)}}. \tag{3.14}$$

$\Delta\phi$ cut	Response a	Response b	Response c
2.8	0.759 ± 0.016	0.137 ± 0.101	-0.028 ± 0.142
2.9	0.763 ± 0.017	0.139 ± 0.107	-0.029 ± 0.148
3.0	0.758 ± 0.018	0.237 ± 0.113	0.124 ± 0.158
3.1	0.787 ± 0.029	0.270 ± 0.188	0.112 ± 0.245

Table 3.2: Data: variation of response with $\Delta\phi$ cut where a, b and c are constants of Equation 3.12.

$\Delta\phi$ cut	Response a	Response b	Response c
2.8	0.839 ± 0.007	0.077 ± 0.045	-0.031 ± 0.064
2.9	0.840 ± 0.008	0.073 ± 0.046	-0.036 ± 0.066
3.0	0.836 ± 0.008	0.047 ± 0.050	-0.071 ± 0.071
3.1	0.838 ± 0.011	0.049 ± 0.065	-0.145 ± 0.092

Table 3.3: Monte Carlo: variation of response with $\Delta\phi$ cut where a, b and c are constants of Equation 3.12.

Variation of response with $\Delta\phi$ cut

Placing a tight cut on the ϕ angle between the reconstructed Z boson and the leading jet helps to ensure that events are really only (Z + jets) back-to-back events. However, this cut removes many events from an already small sample so the variation of the response with the loosening and tightening of this cut was investigated. The response for the CC in data and Monte Carlo events are shown in Figures 3.7 and 3.8 respectively. It can be seen that for data there is an increase in the response of approximately 4% as the $\Delta\phi$ cut is varied from 2.8 to 3.1 which is within the statistical errors. For Monte Carlo, there is similarly little discernible variation. The responses are summarized in Tables 3.2 and 3.3, with the variables a,b and c as defined in Equation 3.12.

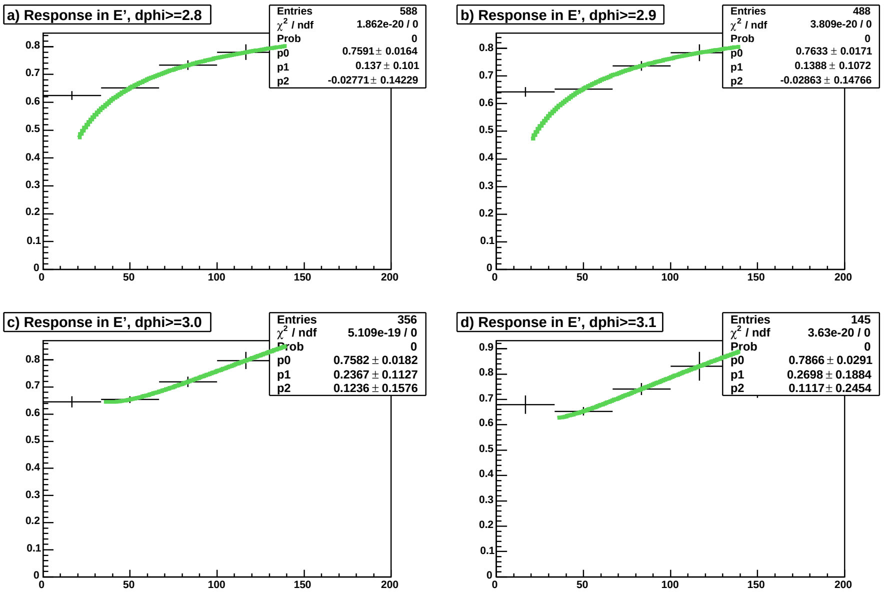

Figure 3.7: Data response with a quadratic log fit, for various $\Delta\phi$ cuts: $a)\Delta\phi \geq 2.8, b)\Delta\phi \geq 2.9, c)\Delta\phi \geq 3.0, d)\Delta\phi \geq 3.1$ after cryostat factor correction.

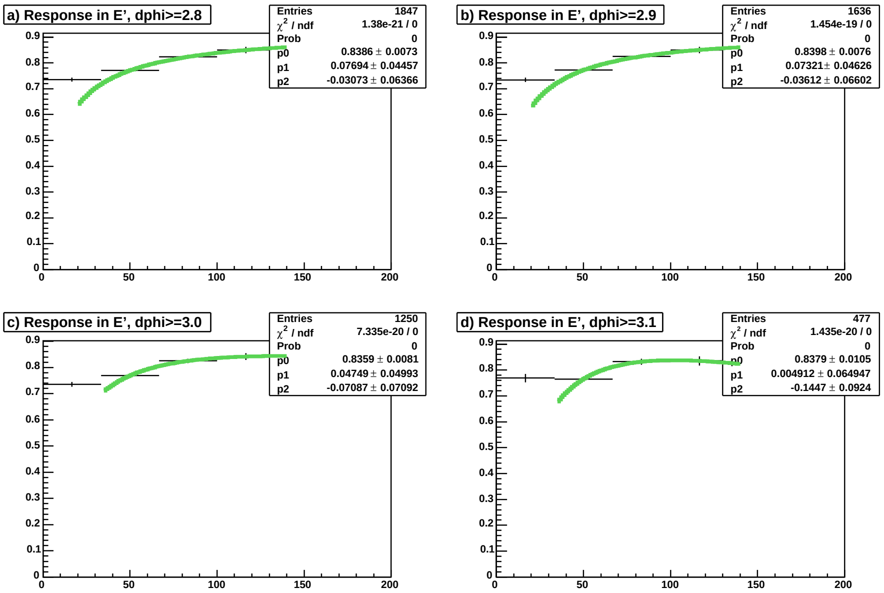

Figure 3.8: Monte Carlo response with a quadratic log fit, for various $\Delta\phi$ cuts: $a)\Delta\phi \geq 2.8, b)\Delta\phi \geq 2.9, c)\Delta\phi \geq 3.0, d)\Delta\phi \geq 3.1$ after cryostat factor correction.

Errors and Uncertainties

The response histograms, binned as a function of E′, were fitted with gaussian functions. The mean of each gaussian was used as the value of the response at the midpoint of the E′ bin. The RMS of the Gaussian fits were taken to be good estimates of the errors in the values of the response. The errors from the overlapping response bins were combined in quadrature to obtain the error on the values of the cryostat factor.

3.3.3 Closure Tests

The response and the jet energy scale from (Z + jets) are not needed to derive the jet energy scale for the calorimeter. This can be done entirely using (γ + jets) events. Z+jets events can then be used to perform closure tests on the (γ + jets) jet energy scale correction. The jet-Z p_T difference is calculated before the jet energy has been corrected and again after the jet energy has been corrected using the jet energy scale correction package versions 4.2 and 5.1 for the data and the Monte Carlo event samples, and the following plots are for version 5.1. An approximate relative response, R_{approx}, is given by:

$$R_{approx} = (p_{T,Z} - p_{T,jet})/p_{T,Z} \tag{3.15}$$

R_{approx} is calculated for events broken down into calorimeter regions, and before and after JES corrections. For a correctly-calculated jet energy scale correction, the mean of the R_{approx} histograms should move close to zero after the jet energy scale is applied. Figures 3.9 and 3.10 show these histograms for Monte Carlo for all detector regions as well as for the CC, ICR and the EC separately. Figures 3.11 and 3.12 show the equivalent histograms for data. It can be seen that after the jet energy correction has been applied, the distributions indeed move close to zero and so the (γ + jets) jet energy scale was again validated, contributing to the release of the jet energy scale code package, JetCorr. Jets in the EC have higher energies resulting in fewer events in the region and so, as expected, the correction is poorer there due to the larger resulting statistical errors.

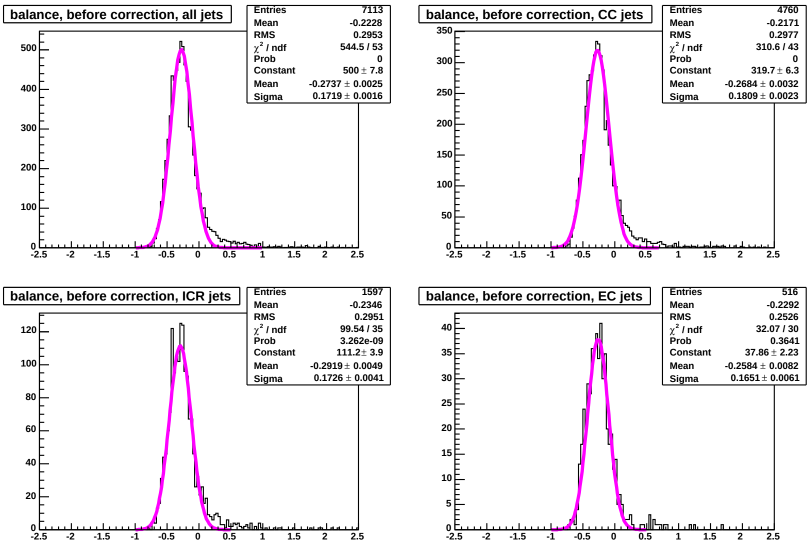

Figure 3.9: Monte Carlo closure tests: histograms of R_{approx} for jets before JetCorr corrections for all regions (top left), and broken down into the CC (top right), ICR (bottom left) and EC (bottom right).

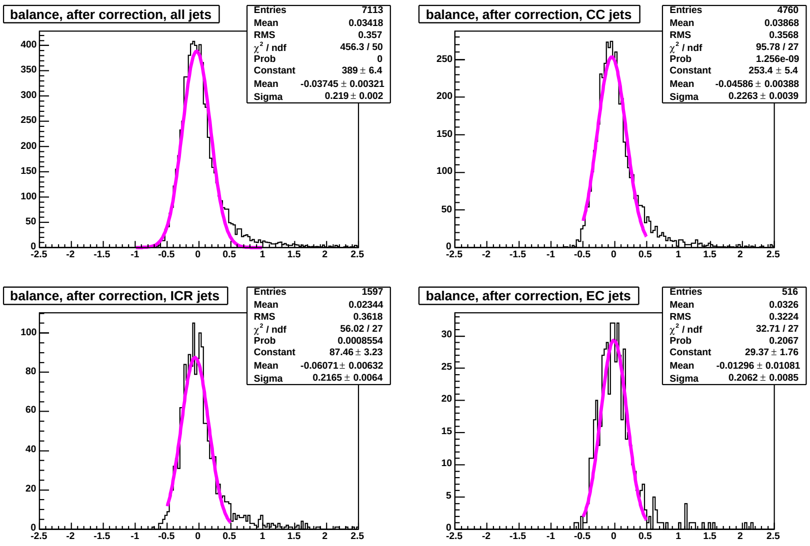

Figure 3.10: Monte Carlo closure tests: histograms of R_{approx} for jets after JetCorr corrections for all regions (top left), and broken down the CC (top right), ICR (bottom left) and EC (bottom right).

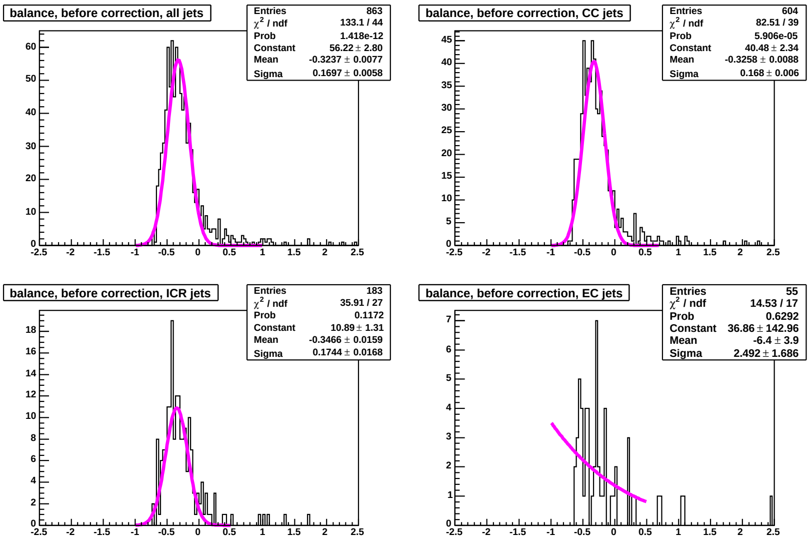

Figure 3.11: Data closure tests: R_{approx} for jets before JetCorr corrections for all regions (top left), and broken down into the CC (top right), ICR (bottom left) and EC (bottom right). Note the inability to fit satisfactorily a gaussian curve to the data in the EC (bottom right) due to the low statistics as noted earlier in this subsection.

3.4 Discussion

Figures 3.3, A.2, A.1, and A.3 show that the Gaussian fit to the binned responses describes well the distributions; only in the histograms with relatively high statistics is there a small tail evident at high jet energy. In general, there is a lack of statistics at high E′ and in the EC for both the MC and the data. The lack of statistics in the EC and at high energy in the CC means that it is difficult to constrain the quadratic log fit to the response function at high energy, but also that the cryostat factor has large errors of approximately 40%, and that it is not possible to separate values in data for F_{cryo} for the north and south EC regions of the calorimeter. Furthermore, the large error in F_{cryo} means that it is not possible to make a good comparison between the two regions. The plotted data and MC responses, after the cryostat factor correction, Figures 3.6(a) and 3.6(b), show that the response decreases at low

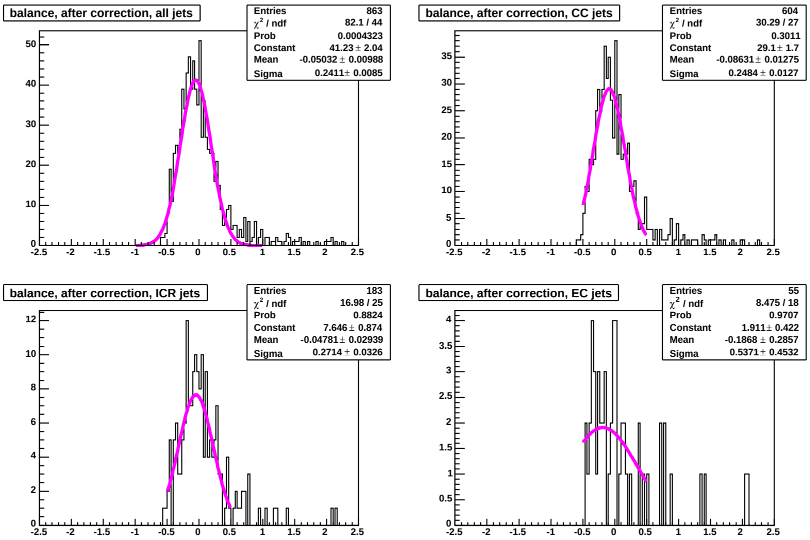

Figure 3.12: Data closure tests: R_{approx} for jets after JetCorr corrections for all regions (top left), and broken down into the CC (top right), ICR (bottom left) and EC (bottom right).

energy due to the worsening jet resolution, as expected. The low E_T bias is evident in the sudden increase in the response for jet energies below 25GeV, but this is more obvious in the data response than the MC response.

Figure 4.14 shows the (γ + jets) response (v4.2 JES) for MC and data[11]. Table 3.4 compares the response parameters for both data and MC for (Z + jets) and (γ + jets) samples. The responses in data and MC for both (Z + jets) and (γ + jets) samples are similar in shape and size, and agree slightly better in MC than in data. Clearly, there are not enough statistics remaining in the (Z + jets) event samples after selection to make a precise verification of the (γ + jets) response. Comparing F_{cryo} derived from (Z + jets) and (γ + jets) events in Table 3.4, it can be seen that F_{cryo} agrees well, within errors, for both MC and data. [12]

---

[11] See equation 3.12 for definition of a, b and c

[12] Note: The cryostat factor for data is an average of the cryostat factors of the separate north (0.9426 ± 0.0028) and south (0.9118 ± 0.0026) EC regions. These are combined for comparison with the (Z + jets) cryostat factor where there aren't sufficient statistics to derive separate cryostat factors. This separation of cryostat factors does not apply to MC as the calorimeter is modelled

Sample	Event	a	b	c	F_{cryo}
Data	(Z + jets)	0.758 ± 0.018	0.237 ± 0.113	0.124 ± 0.158	0.912 ± 0.130
Data	(γ + jets)	0.805 ± 0.001	0.071 ± 0.006	-0.003 ± 0.003	0.948 ± 0.006
Monte Carlo	(Z + jets)	0.836 ± 0.008	0.0474 ± 0.050	-0.071 ± 0.071	0.957 ± 0.118
Monte Carlo	(γ + jets)	0.847 ± 0.002	0.0644 ± 0.002	-0.007 ± 0.003	0.956 ± 0.003

Table 3.4: Comparison of (Z + jets) and (γ + jets) response parameters, and cryostat factors in data and Monte Carlo (Z + jets) and (γ + jets) event samples.

Deriving the response using (Z + jets) events is a valid way to verify the (γ + jets) response. All available p14 data were used, and even though (Z + jets) events could not be used to derive the full correction, it was possible to carry out valid closure tests.

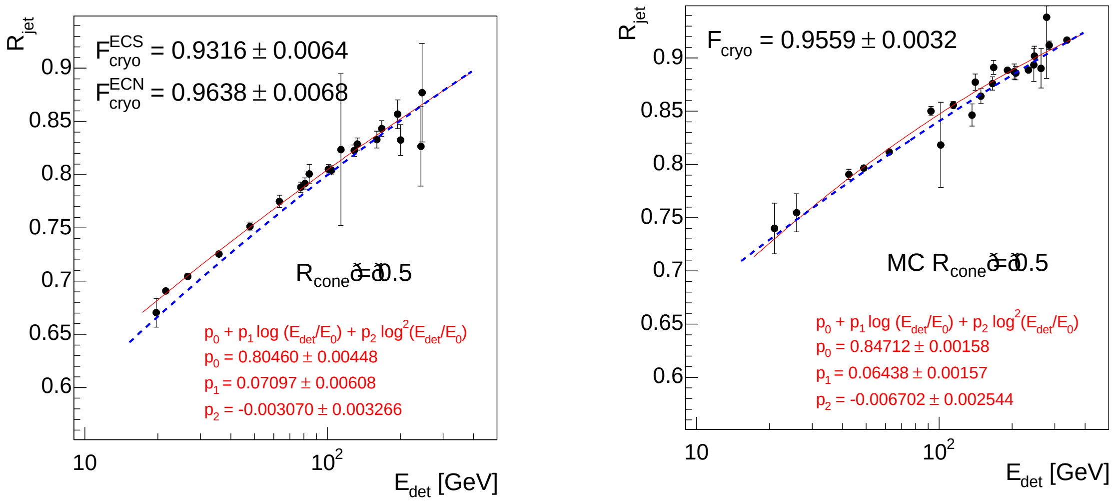

(a) Data

(b) Monte Carlo

Figure 3.13: Response plot for (γ + jets) events. Solid lines represent the response from R=0.5 jets, and the dashed lines represent the response from R=0.7 jets. [5]

---

as being uniform.

3.5 Conclusion

As part of the certification of version 4.2 of the (γ + jets) official jet energy response, the response was calculated for data and MC for p14 (Z + jets) events, using the missing E_T projection fraction method. Closure tests on (Z + jets) events, using versions 4.2 and 5.1 of the (γ + jets) jet energy scale were performed, contributing to the release of the jet energy scale. Both the (Z + jets) response and the closure tests verified the (γ + jets) response, providing a valid check of the response before it was implemented as part of the jet energy scale at DØ. The (Z + jets) and (γ + jets) response agreed well within errors and no discernible variation of the (Z + jets) response with the variation of the back-to-back requirement of the Z boson and the leading jet was found. Despite using all available data and MC, the lack of statistics meant that (Z + jets) events could not be used to derive the full jet energy correction or be used for a precision verification of the (γ + jets) response. However, approximately $1fb^{-1}$ data are now available for use with a new collaboration-wide analysis format; it is now possible to derive a response for (Z + jets) events with a precision comparable to the (γ + jets) response.

Chapter 4

The Calorimeter Response to Semileptonic Decays and Energy Flow

4.1 Introduction

Many physics processes of interest at DØ involve b-jets. For example, one of the best ways to detect a light, standard model Higgs boson is via its decay to a $b\bar{b}$ pair; DØ has a large b-physics programme, but many other physics programmes involve b-jets. Therefore, it is important that DØ has both a good jet energy scale that is appropriate to its physics programmes, and that it improves the jet energy resolution using all available techniques. In the first part of this chapter, an improvement to the jet energy scale is calculated specifically for certain commonly-used b-jets. In the second part of this chapter, an electromagnetic scale for calorimeter clusters is derived as part of the implementation of a new algorithm to improve jet energy resolution using the tracking system together with the calorimeter.

B-jets have different characteristics to light quark jets since $m_b \gg m_q$; b-jets have different decay kinematics and harder fragmentation leading to a different jet energy scale. Approximately 10% of the time [8] the b-jet contains a lepton and a neutrino from the *direct* semileptonic decay of the original B–hadron ($b \rightarrow l\nu$). Alternatively, the B–hadron may decay via a charm-hadron, and then the c-quark itself may decay semileptonically approximately 20% of the time [8], this process is denoted as a *cascade* decay ($b \rightarrow c \rightarrow l\nu$). In both cascade and direct decays the measured jet energy will not include the energy of the escaping neutrino, but will include the energy of the lepton depending on whether it is an electron or a muon. If the lepton is an electron, all its energy will be contained within the calorimeter, but, for a muon, only a small amount of energy is deposited (typically on the order of 2 GeV). Thus for semileptonic decays, the energy of the b-jet has to be corrected for the energy of the neutrino, and for muonic semileptonic decays, the muon energy measured in the muon detector must also be added back into the jet energy. A correction may be made as part of the jet energy scale for the special case of muonic semileptonic decays. A scalar, Monte Carlo based, semileptonic correction to b-jets is derived in the first part of this chapter using $t\bar{t}$ events, and this was incorporated into versions 5.1 and 5.3 of the DØ JES [70]. The v5.1 corrections use p14 data and Monte Carlo. In this chapter, the muonic semileptonic correction is addressed, as part of the official jet energy scale version 5.1. A vector semileptonic correction is also considered. The effects of the semileptonic correction on the dijet mass resolution in $Z \rightarrow b\bar{b}$ and $H \rightarrow b\bar{b}$ MC events are evaluated.

At DØ, it is possible to improve the jet energy resolution and reduce the systematic error of jet energy measurements by combining the energy measured by the calorimeter with the momentum measured in the tracking system. Since the tracker has better momentum resolution than the calorimeter at low energy, it may be used to compensate for the poor low-energy measurements of the calorimeter. The energy flow (*eflow*) algorithm [77] reconstructs the flow of energy in an event, combining information from the subdetectors to create eflow particles from tracks in the tracker through to calorimeter cells. These well-understood eflow particles are used to reconstruct more complex physics objects such as jets, and event properties. In this chapter, as a necessary part of the possible implementation of an eflow algorithm, an electromagnetic scale is derived for calorimeter cell clusters, using low-momentum tracks.

4.2 Semileptonic Decays: Muons

4.2.1 Definition of the Semileptonic Correction

To measure correctly the jet energy for muonic b-jets, a correction must be calculated to compensate for the undetectable neutrino but this is not straightforward. In addition, the muon energy must be added to the jet energy. The muonic semileptonic correction is derived for direct and cascade decays using the method prescribed originally in the p13 certification of the jet energy scale [78]. The correction factor is defined as:

$$C = \frac{E_\mu^{MC} + E_\nu^{MC}}{E_\mu^{meas}} \tag{4.1}$$

where E_μ^{MC} and E_ν^{MC} refer to the generator-level muon and neutrino energies respectively, and E_μ^{meas} to the reconstructed energy of the muon. The correction factor was parameterised as a function of the reconstructed muon energy. A second-order dependence of the correction on the b-jet energy and on p_T^{rel} was also investigated, where p_T^{rel} is the p_T of the muon with respect to the combined muon-b-jet axis. The p_T^{rel} can be a powerful discriminator of b-jets from charm and light jets [79]. A fit to the correction factor using the functional form in Equation 4.2 was made.

$$C_{fit} = p_0 + e^{(p_1 + p_2 \cdot E_\mu^{meas})} \tag{4.2}$$

Event Selection

The event selection is divided into three main parts in addition to general event cuts: the generator level selection, the reconstructed jet selection and the reconstructed muon selection. The correction factor is derived from 88,000, p14.02.00, Pythia-generated [74] plate[1] $t\bar{t} \rightarrow Wb(l\nu)Wb(l\nu)$ Monte Carlo events, corrected with v.5.1 of the official DØ jet energy scale.

General Event Cuts As in the derivation of the jet response, it was required that the primary vertex z-coordinate must have $|z| <$50cm and that the primary vertex must have at least two associated tracks.

---

[1] Plate MC events are those where the calorimeter has been simulated as a series of uranium and argon plates.

Generator-Level Selection Cuts The selection at the generator level aimed to identify events in which either of the two b-jets contained a semileptonic decay, either direct or cascade. The generator level selection consisted of the following steps:

1. b-quarks from the decay of the top were selected and their decay chains inspected to see if they contained an oppositely signed muon and a neutrino, originating from the same generator level vertex.
2. If the parent of the muon and neutrino was a B-meson then the decay was flagged as direct.
3. If the parent was a C-meson and the parent of the C-meson was a B-meson then the decay was flagged as cascade.
4. If one or both b-quarks from the top quarks satisfied the above requirements the event was passed.

The above selection allowed the unambiguous identification of events containing semileptonic decays of interest and the unambiguous selection of the generator level muon, neutrino and b-quark. In the case of both b-quarks decaying semileptonically, the two decays were treated independently and hence event rejection should be understood in terms of either decay.

Muon Selection Reconstructed muons passing the medium identification (*good muons*) requirements as defined in Section 2.2.8 were used. If the $\triangle$R in $\eta \times \phi$ space between the generator-level and reconstructed muons was less than 0.2 then they were considered matched. If more than one reconstructed muon was matched to the same generator-level muon, the event was rejected.

Jet Selection The jets were reconstructed using the Run II cone algorithm with a cone size of 0.5. The jets were selected using the standard jet-ID for p14, as used in the (Z + jets) response event selection. The jet was matched to the b-jet by requiring that the $\triangle$R between the jet and the b-quark was less than the 0.5 (the cone size of the jet). If it was possible to match more than one jet to the b-quark, the event was rejected. The b-jet was subsequently corrected using version 5.1 of the jet energy scale.

Cutflow Table 4.1 shows the number of events remaining after the event selection cuts, for cascade and direct decays and for p_T^{rel} greater and less than 1 GeV. Figure 4.1 shows the $\triangle$R distribution between all good muons and the generator-level muons, between all jets passing the selection cuts and the generator-level b-quark and between the selected muon and b-jet. As expected, in all three plots there are sharp peaks around zero, with small numbers of events stretching out to larger δR in the left and middle plots where the reconstructed objects are compared to the generator objects. These insignificant numbers of events highlighting biases or errors in the DØ reconstruction software that are not discussed here. All plots seem consistent with each other as expected and show that the event selection was valid.

Direct	5548	$p_T^{rel} > 1$GeV	3443
		$p_T^{rel} < 1$GeV	2103
Cascade	841	$p_T^{rel} > 1$GeV	155
		$p_T^{rel} < 1$GeV	686

Table 4.1: Number of selected events for cascade and direct decays, with $p_T^{rel} >$ 1GeV and $p_T^{rel} <$ 1GeV.

Figure 4.2 displays the generator-level muon energy as a function of the reconstructed muon energy, with a solid line corresponding to $y = x$ shown for comparison. The response is seen to be linear over the whole range and the two appear highly-correlated with little spread, as expected.

Calculating the Correction Factor

The correction factor, C, was calculated by binning C in intervals of 4GeV of reconstructed muon energy, from 0GeV to 96GeV. An example histogram is shown in Figure 4.3.

Two possible ways to calculate the correction factor per muon energy bin were considered: using the mean of the correction factor in that bin or using the median value. Figure 4.4 shows the correction factor obtained using the median and the

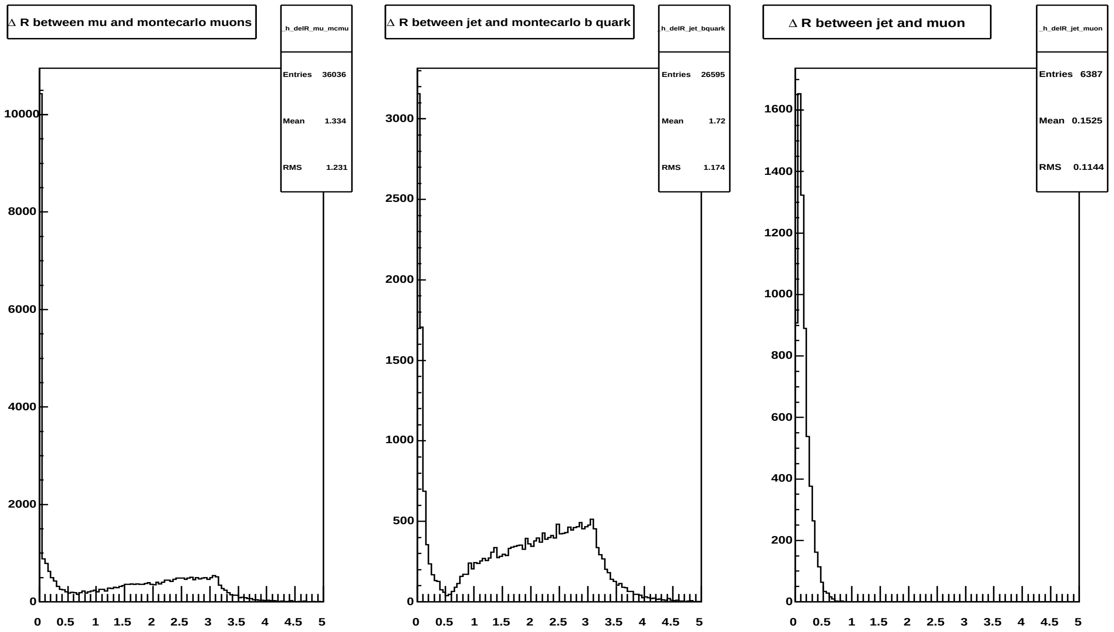

Figure 4.1: △R plots between the main objects in the event. $\triangle R$(reconstructed muon, generator muon), (left). $\triangle R$(reconstructed jet, generator b-quark), (middle). $\triangle R$(reconstructed jet, reconstructed muon), (end).

mean. Overlaid is the scatter plot of the correction values against the reconstructed muon energy and the correction factor derived using the generator level median values. The similarity between the two indicates that there is little reconstruction bias for this sample and that the muon energy is well-calibrated. Figure 4.4 shows that the mean generally lies above the typical values of the correction factor, whereas the median is more representative of the distribution. This is also illustrated in the highly non-Gaussian distributions in the histograms of the correction factor binned in muon energy. A consequence of the non-Gaussian nature of the correction factor per muon energy bin is that the mean is more sensitive to points which lie in the tail at the high end of the distribution. To avoid using a correction factor which can vary significantly based on the effect of a few points, and to use a correction which is more representative of the "typical" correction, the median value was used. It was assumed that the error on the mean would be indicative of the error of the median.

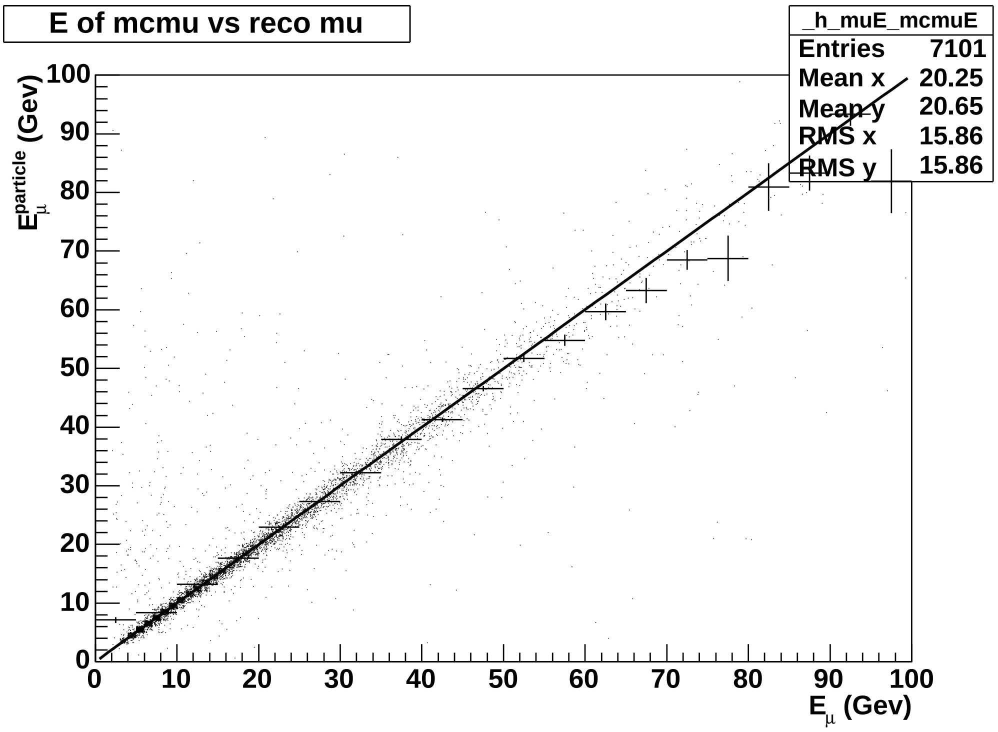

Figure 4.2: Generator level muon energy, $(E^{particle})_{\mu}$, as a function of reconstructed muon energy, E_{μ}^{reco}. Solid line corresponds to y=x. The points show the scatter of data points, while the cross-hairs represent the midpoints of the same data points, binned.

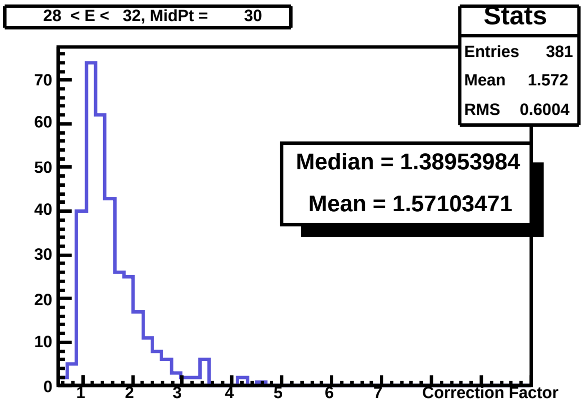

Figure 4.3: Typical correction factor distribution (Muon energy bin 28GeV $< E_{\mu} <$ 32 GeV).

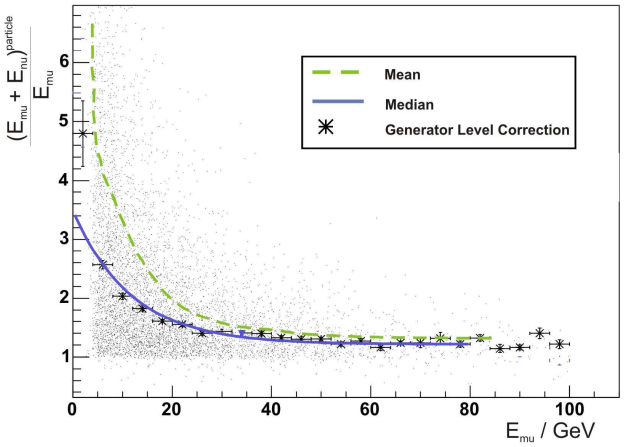

Figure 4.4: Correction factor as a function of the reconstructed muon energy for inclusive decays. Also shown is the correction factor in terms of generator level information.

Correction Factor for Inclusive Decays

Figure 4.5 displays the correction for the inclusive sample split by the energy of the bjet into $E_{jet} > 50$ GeV and $E_{jet} < 50$ GeV. There seems to be a slight dependence on jet energy per E-bin; however, with the low statistics available, the evidence is inconclusive.

Figure 4.6 displays the correction factor for inclusive decays split by $p_T^{rel} > 1$GeV and $p_T^{rel} < 1$GeV. Again, there seems to be only a slight dependence on p_T^{rel}, with the correction being higher for events with $p_T^{rel} < 1$GeV. This is possibly due to different corrections for cascade and direct decays which is discussed further in the next section.

Correction for Direct and Cascade Decays

There is no reason to expect the correction factor to be the same for direct and cascade decays. Direct decays should have a higher correction than cascade decays due to the higher boost and higher b-quark mass. However, in Figure 4.6, the correction factor for $p_T^{rel} < 1$GeV seems to be slightly higher than that for $p_T^{rel} >$ 1GeV, which would indicate that it is not possible to separate cascade and direct

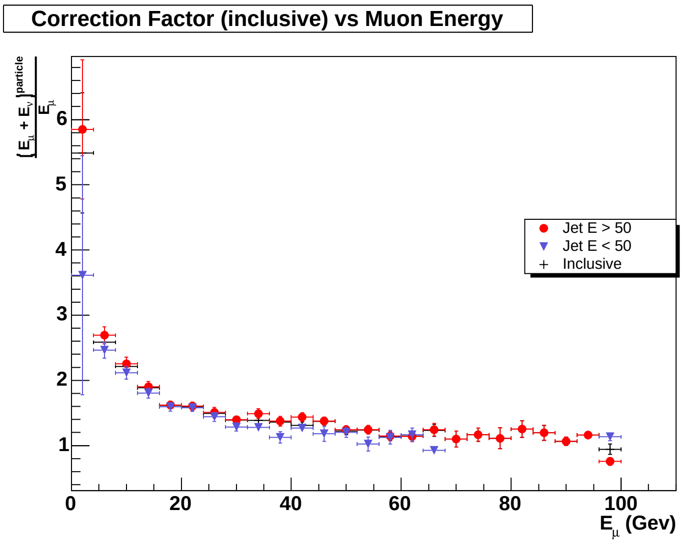

Figure 4.5: Correction factor as a function of reconstructed muon energy for $E_{b-jet} < 50$ GeV and $E_{b-jet} > 50$ GeV.

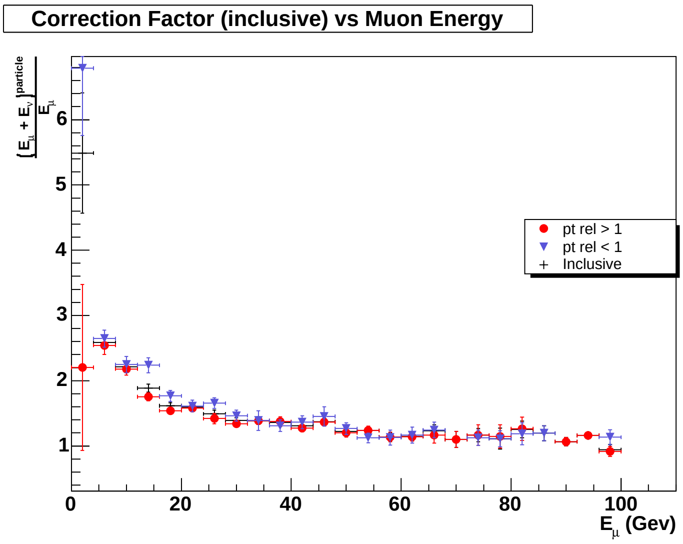

Figure 4.6: Correction factor as a function of reconstructed muon energy for $p_T^{rel} > 1GeV$ and $p_T^{rel} < 1GeV$

decays by p_T^{rel}. Figure 4.7 shows the reconstructed p_T^{rel} distribution for direct, cascade and inclusive decays; the p_T^{rel} distribution is dominated by direct decays except at very low p_T^{rel}. This is due to the high branching ratio of the direct decay compared to the cascade decay and is again illustrated by Table 4.1. Figure 4.8 shows the correction separately for direct and cascade decays. As expected, the correction

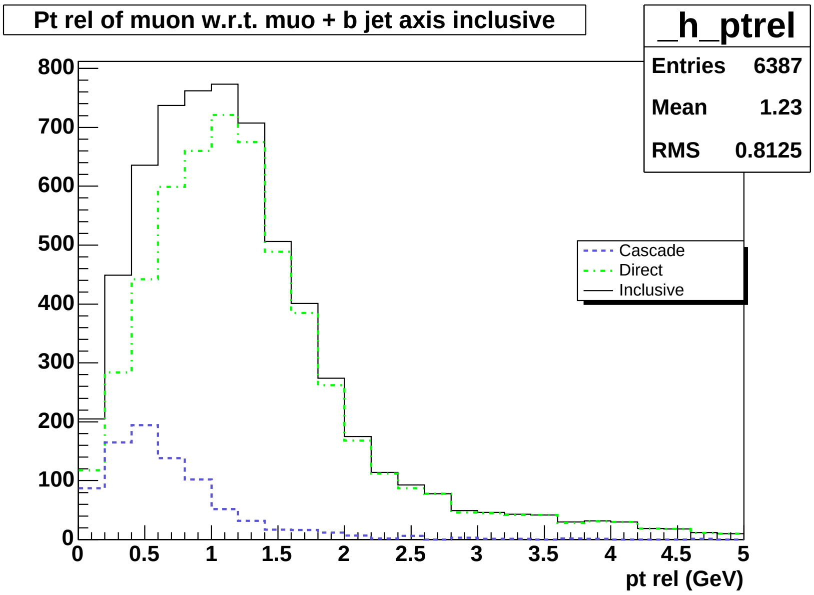

Figure 4.7: Reconstructed p_T^{rel} distribution for direct, cascade and inclusive decays

factor for direct decays is noticeably higher than that for cascade decays. Figure 4.9

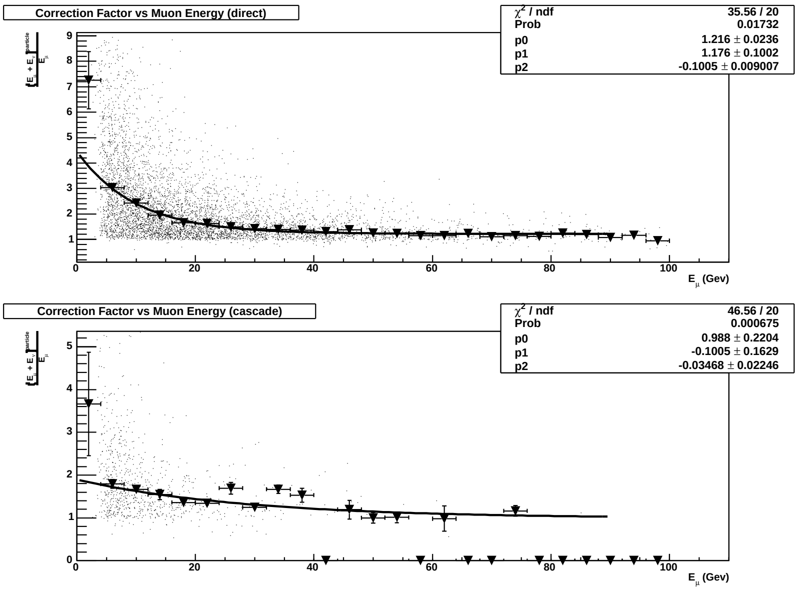

Figure 4.8: Correction factor as a function of reconstructed muon energy for direct (top) and cascade (bottom) decays

shows the dependence of the correction factor on p_T^{rel} for direct and cascade decays separately. When decays are separated, there is a stronger dependence on p_T^{rel} than for the inclusive sample shown in Figure 4.6. Again, the correction is larger for p_T^{rel}

< 1GeV. The statistics are limited for cascade decays with high p_T^{rel} but in the lower muon energy bins, which have the most statistics, a dependence on p_T^{rel} appears to be present. The lack of statistics means that the fit for $p_T^{rel} > 1$GeV is unreliable.

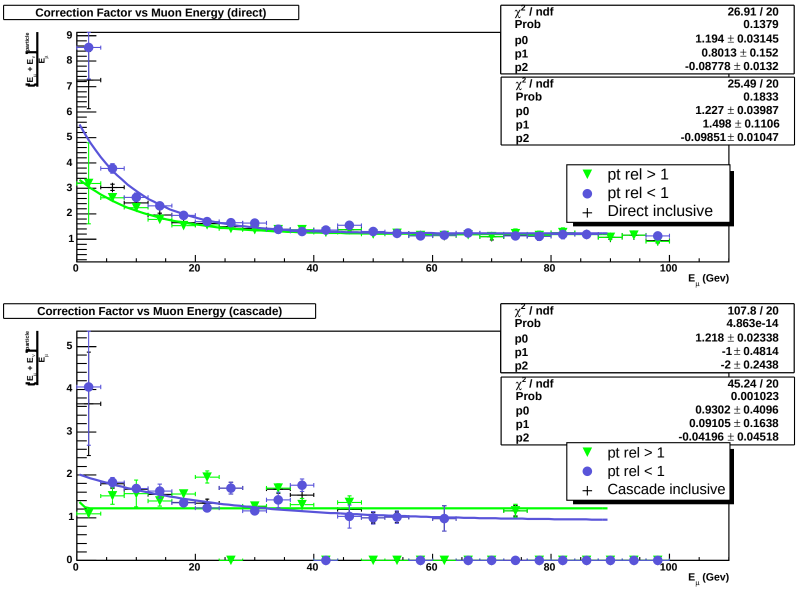

Figure 4.9: Correction factor as a function of reconstructed muon energy for direct (top) and cascade (bottom) for p_T^{rel} greater and less than 1 GeV.

Figure 4.10 shows the dependence of the correction factor on E_{jet} for direct and cascade separately. For direct decays, the dependence on E_{jet} is somewhat larger, particularly at small energies, than for the inclusive sample shown in Figure 4.8. For cascade decays, there are insufficient statistics to draw a conclusion.

Figures 4.11 and 4.12 show the dependence of the correction factor on jet energy after being split by p_T^{rel} for direct and cascade decays respectively. Unfortunately, the statistics are not enough to allow the correction factor to be differentiated by both p_T^{rel} and E_{jet} simultaneously for direct and cascade decays separately.

The correction factors derived here were implemented as part of the JetCorr package. The implemented correction was first split by decay type, into direct, cascade and inclusive decays. The correction was then split by p_T^{rel} , but for direct and inclusive decays only, as there were insufficient statistics for this to be done for cascade decays. The dependence of direct decays on p_T^{rel} is more pronounced than the dependence on E_{jet} as shown in Figures 4.8 and 4.9 (upper panels). A single

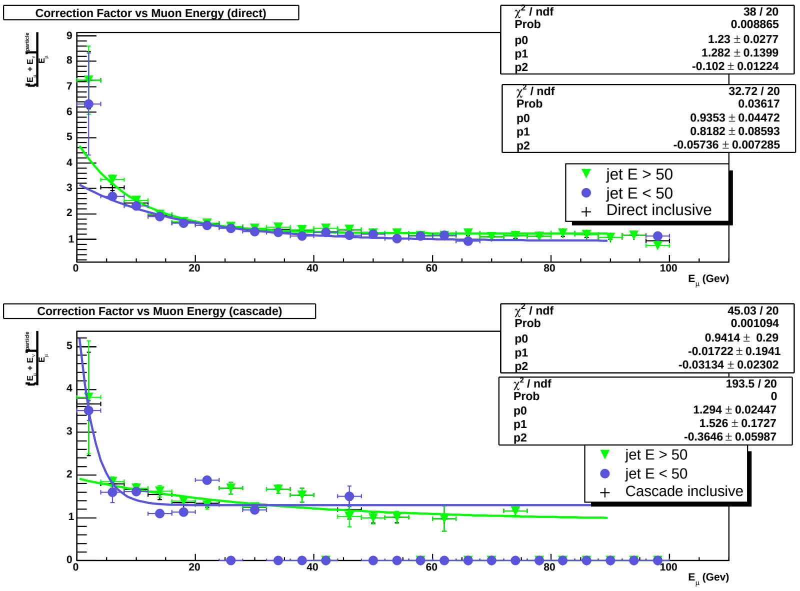

Figure 4.10: Correction factor as a function of reconstructed muon energy for direct (top) and cascade (bottom) for jet energy greater and less than 50 GeV.

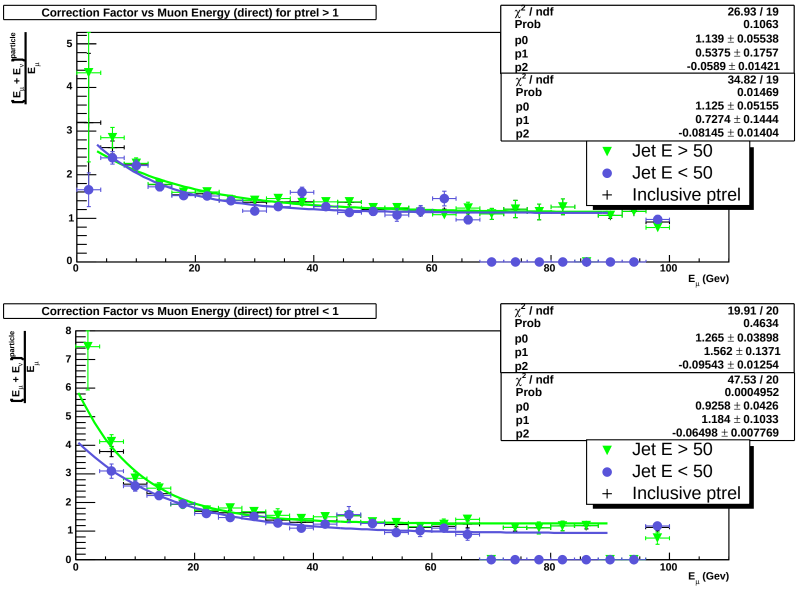

Figure 4.11: Correction Factor for direct decays for $E_{jet} < 50$GeV (upper fit values) and $E_{jet} > 50$GeV (lower fit values), split by $p_T^{rel} > 1GeV$ (top) and $p_T^{rel} < 1GeV$ (bottom).

common correction factor was used for cascade decays for all p_T^{rel} taken from Figure 4.8 (lower panel). The dependence on E_{jet} was ignored as there were insufficient

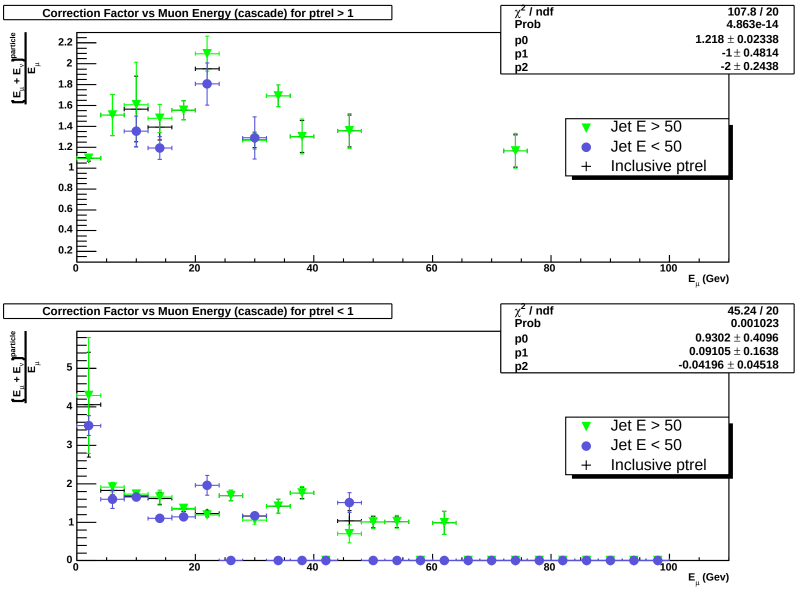

Figure 4.12: Correction factor for cascade decays for $E_{jet} < 50$GeV and $E_{jet} >$ 50GeV, split by jet energy for $p_T^{rel} > 1GeV$ (top) and $p_T^{rel} < 1GeV$ (bottom). In each plot the upper fit values are for $E_{jet} > 50$GeV and the lower values are for E_{jet} < 50GeV

statistics to constrain the correction factor parameters. To compensate for the muon energy that is deposited in the calorimeter and removed when the jet energy correction is applied, 2GeV is subtracted from the muon energy.

Comparison of the correction to generator-level information

Figure 4.13 compares the neutrino energy for direct decays obtained using the correction factor to that at generator level. The lower plot in Figure 4.13 shows the difference in neutrino energy between that obtained from the fit and that at generator level. Figure 4.13 highlights the benefits and drawbacks of this method to correct the energy of b-jets. Although on average the neutrino energy is correct, as can be seen by a mean close to zero in the lower plot, the neutrino energy distribution is completely different. The use of such a correction factor eliminates the extreme values in the neutrino energy distribution and hence averages the distribution so that it is peaked at a value close to the mean generator level neutrino energy.

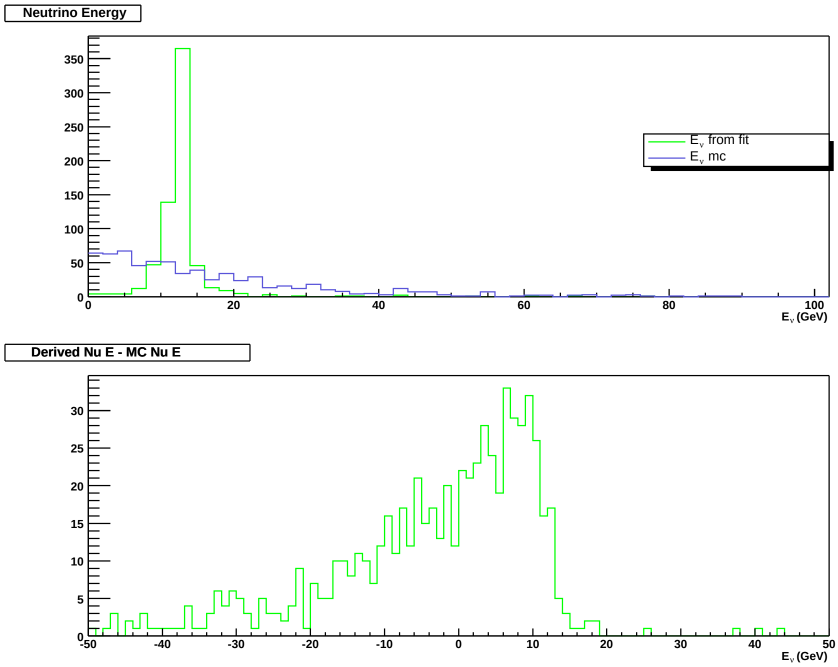

Figure 4.13: Neutrino energy from generator level information and the neutrino energy derived from the fit to the correction factor (top), difference between the two neutrino energies (bottom).

4.2.2 Vector Correction

So far, the semileptonic correction has been derived to correct only the absolute value of the b-jet four-momentum and for the 2GeV muon energy deposit, without changing its direction. To improve upon the scalar correction, and to account for the change in jet direction, a vector semileptonic correction was proposed. The corrected jet four-momentum, p^{corr}_{jet}, is defined as:

$$\overrightarrow{p}^{corr}_{jet} = \overrightarrow{p_{old}} + (\overrightarrow{p_\mu} + \overrightarrow{p_\nu}) - \overrightarrow{2GeV} \tag{4.3}$$

where the vectors $\overrightarrow{p_\nu}$ and $\overrightarrow{2GeV}$ have the same direction as the muon four-momentum, $\overrightarrow{p_\mu}$. The neutrino energy is derived from the correction factor, in terms of the muon energy, as described before. Figures 4.14(a) and 4.14(b) show the $\triangle R$ distributions between the original b-quark and the jet after scalar semileptonic correction and after vector semileptonic correction respectively. It can be seen that the vector correction reduces both the mean and the spread of the $\triangle R$ distributions and so corrects more successfully the jet back to the original b-quark direction, compensating for the direction-change from the “loss” of the muon and neutrino. Although this method of applying the correction shows potential for improvement over the scalar correction, it was not fully implemented as it was felt that more effort should be focussed on improving the jet energy scale as a whole.

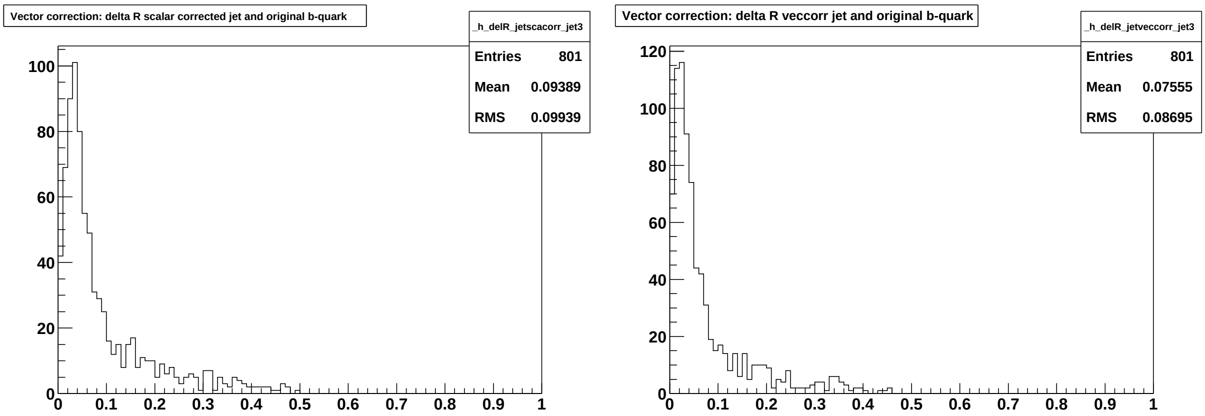

(a) Scalar semileptonic correction

(b) Vector semileptonic correction

Figure 4.14: $\triangle R$ between the b-quarks and the b-jets corrected with a)the scalar and b)the vector semileptonic corrections.

4.2.3 Closure Test: Effects on Mass Resolutions

The effect of the basic jet energy scale correction and the full correction (i.e. including the scalar semileptonic correction where appropriate) in the dijet mass resolution was investigated using MC event samples of $Z \rightarrow b\bar{b}$ and $H \rightarrow b\bar{b}$ ($m_H = 115$ GeV) decays. In these events, it was required that both jets pass the same standard p14 jet identification selection criteria as detailed in Section 4.2.1, and no mass cut was placed on the dijet masses. Where there was a good b-jet in the event that did not decay semileptonically, the basic jet energy scale was applied. Where the b-jet did decay semileptonically, both the basic jet energy scale and the scalar semileptonic corrections were applied. The Z and H bosons were then reconstructed from the two jets in the event. Table 4.2 shows how the dijet masses, and mass resolutions are affected by the two jet energy scale corrections. A typical dijet mass distribution is shown in Figure 4.15.

		Before Correction	Basic Correction	Full Correction
$H \rightarrow b\bar{b}$	Mean	75.7 GeV	107.6 GeV	120.3 GeV
	RMS	15.4 GeV	19.3 GeV	16.9 GeV
	Resolution	20%	18%	14%
$Z \rightarrow b\bar{b}$	Mean	55.5 GeV	82.1 GeV	93.1 GeV
	RMS	11.9 GeV	15.5 GeV	13.4 GeV
	Resolution	21%	19%	14%

Table 4.2: Dijet masses, spreads of the distributions and resolutions for $H \rightarrow b\bar{b}$ and $Z \rightarrow b\bar{b}$ MC samples after no JES correction, basic JES correction, and full jet correction. The error on the means and RMS is approximately 0.5GeV.

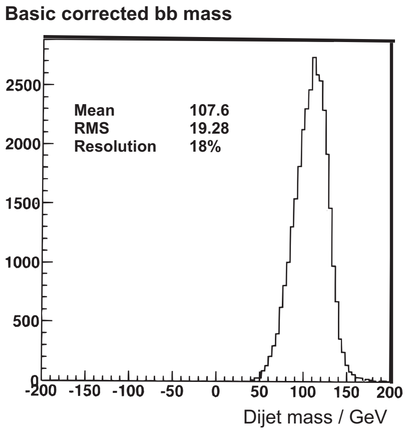

Figure 4.15: Dijet Mass Resolutions for $H \rightarrow b\bar{b}$

It can be seen from Table 4.2 that applying the full correction[2] to semileptonic decays appears to improve the resolution for those decays more than simply applying the basic correction to all decays. However, as the number of semileptonic decays is less than 20% of all decays, the effect on the overall resolution is reduced. The effect of the semileptonic correction on the $Z \rightarrow b\bar{b}$ dijet mass resolution was further investigated: the resolution was measured for events with zero, one and two semileptonic decays in the event. The results are summarised in Table 4.3. The dijet mass distributions were fitted with Gaussian functions which described them well, and the mean and σ were used to calculate the resolutions. It can be seen that without the semileptonic correction, the resolution is poorer for events with one or

---

[2] Note: the full correction is only applied to events where both jets were b-tagged

	Mean	σ	**Resolution/%**
Dijet Mass, no correction			
All Events	55.26	11.25	20
> 1 semileptonic decay	48.97	10.55	22
2 semileptonic decays	42.06	10.74	26
0 semileptonic decays	56.33	10.97	20
Dijet Mass, basic correction			
All Events	81.79	14.87	18
> 1 semileptonic decay	73.26	14.07	19
2 semileptonic decays	64.75	14.10	22
0 semileptonic decays	83.27	14.45	17
Dijet Mass, full correction			
All Events	83.32	14.46	17
> 1 semileptonic decay	72.90	13.21	18
2 semileptonic decays	93.34	13.36	14
0 semileptonic decays	83.27	14.45	17

Table 4.3: Dijet mass Gaussian means, sigmas and resolutions for $Z \rightarrow b\bar{b}$ events with no correction, basic JES correction and basic + semileptonic correction. Errors on the means and sigmas are approximately 0.1GeV, except for the case of two semileptonic decays where the error is approximately 1GeV due to lower statistics.

more semileptonic decays as expected. For events with no semileptonic decays, the resolution is improved by applying the basic correction by 15%. The semileptonic correction improves the resolution for events with at least one semileptonic decay by 22% and for events with two semileptonic decays by approximately 50%. Overall, the improvement to the dijet mass resolution for all jets when the full correction (i.e. with or without the semileptonic correction as appropriate) is applied is 15%.

4.2.4 Discussion

The semileptonic correction derived in this chapter clearly improves upon the basic jet energy scale corrections and was used in the official release of the jet energy scale correction for p14 data. The vector correction has the potential to enhance this semileptonic correction. It remains to consider how this vector correction will be implemented in both MC and data. The muon momentum in MC is better than that in data, and so the MC muon momentum should be smeared to match the MC resolution to that in data. At the time this work was carried out, a muon MC smearing had not been calculated but was planned and it would be interesting to see how this affects the semileptonic correction. Furthermore, before the vector correction could be used, the size of the muon calorimeter MIP energy deposit, set at 2GeV should be investigated.

4.3 Energy Flow: Electromagnetic Calorimeter Calibration

A first, illustrative, version of an eflow algorithm was coded in the DØ environment in 2002 [77]. It is based on the ALEPH package [80]. Preliminary studies, based on Monte Carlo, have shown jet resolution improvements of about 20% for low and intermediate energy jets. The next step was to update the basic algorithm and test it on data, a process that was started in December 2003.

Eflow Particles There are three types of eflow particles produced based on track-calorimeter associations: charged particles, photons and neutral hadrons. Energy flow should include information from all the subdetectors, but at DØ , mostly tracker and calorimeter information is used, with some information from the muon system. Charged particles are made of one track associated with a calorimeter cluster of energy, whereas a photon or a neutral hadron is an electromagnetic or hadronic cluster with no associated track. The energy clusters are calorimeter cells with energy deposits that have been clustered using a nearest neighbour clustering algorithm, the *cellNN* algorithm [81], thus a calorimeter cellNN calibration is needed. Reconstructed tracks are extrapolated through the calorimeter along a straight line and all clusters crossing the track are matched if their energy is <1% of the track momentum. [3]

---

[3] This cut is to strike a balance between matching efficiency and fake associations.

4.3.1 Towards a Working Algorithm

Eflow is more complicated than a simple calorimeter energy measurement so several things must be considered. To implement a working eflow algorithm, several calibrations and scales need to be calculated and integrated: a calorimeter cell-level scale for hadronic and electromagnetic particles scale, accurate cell-level calibrations for the calorimeter itself, and a tracking scale with understanding of the systematics at low energy. As stated earlier, effort was redirected back to eflow in December 2003 and one of the necessary steps was to derive a track-EM cell intercalibration In this section, an electromagnetic scale for calorimeter cell clusters is derived using low momentum ($<$ 25GeV) MC and data $J/\Psi \rightarrow e^+e^-$ event samples. The electromagnetic scale is calculated using clusters of calorimeter cells that are matched to within 0.2 in η and ϕ (R<0.2)of a track that has been identified as coming from an electron. The momentum of the track is taken to give the 'correct' energy for the cluster and a function is derived to map the cluster energy back to the track momentum. The EM scale is examined for the whole detector as a function of cluster energy and cluster detector η. Events are chosen to have at least two electrons, matched to clusters, that reconstruct to give an invariant mass within the J/Ψ resonance peak.

Tracks from Electrons The electrons whose tracks are used in the calculation of the EM scale are not standard DØ electrons as described in Section 2.2.8, but are identified using the *road algorithm* [82], [83]. The standard way of identifying electrons at DØ relies on the characteristic transverse and longitudinal shapes of EM showers [84]. This method is efficient for high-energy, isolated electrons, but it is not efficient for electrons in jets and so the 'road' method is used primarily to identify such electrons. It is based on the extrapolation of charged tracks in the tracker into the calorimeter; for a given track, only the energy contained in a tube of R=0.2 ('road') along the track extrapolation into the calorimeter is used.

4.3.2 Event Samples and Selection Criteria

A sample of 6560 data events containing at least two EM objects was used as it was the largest suitable dataset available at the time. It was reprocessed with version p14.06.00 [73] of the reconstruction code. The data were skimmed using the low-energy electron triggers E7A_2RL3_RT3_RL5 and E7B_2RL3_RT3_RL5. Table 4.4 lists the L1, L2 and L3 trigger requirements for these triggers. For comparison with MC, an event sample containing 13200 $J/\Psi \rightarrow e^+e^-$ events, processed using p14.03.00 and generated using Pythia, was used. The MC was generated for the central region of the calorimeter only.

Trigger Name	E7A_2RL3_RT3_RL5	E7B_2RL3_RT3_RL5
L1 requirements	• Two calorimeter EM objects with E_T >3GeV. • One of the objects must have E_T >6GeV. • Two tracks with p_T >3 GeV • One of these tracks must have p_T >5GeV.	
L2 requirements	• Two EM objects with E_T >3GeV within $\|\eta\|$ <1.6. • One of those objects must have E_T > 6GeV	
L3 requirements	• Two road electrons with loose cuts and track p_T >3GeV. • One of the electrons also must satisfy tight cuts. • One of the electrons must have track p_T >5 GeV	

Table 4.4: Details of the L1, L2 and L3 trigger requirements for the E7A_2RL3_RT3_RL5 and E7B_2RL3_RT3_RL5

Electron Track Selection

It is required that there are at least two road electrons in the event which pass the following criteria:

- Isolation $\leq$ 0.9
- HMx8 $\leq$ 75

- Be within the fiducial region of the calorimeter
- Reconstruct to give an invariant mass of between 2.096GeV and 4.096GeV. (J/Ψ mass ±1GeV)
- Be within $|\eta| <1.25$

All road electrons have track matches by definition, and so this was not a selection criterion. The standard isolation cut is to require that Isolation $\leq$ 0.15. However, electrons from J/Ψ are likely to not be particularly isolated so this was loosened to allow more events to pass the cuts. The electrons were also required to pass the 'tight' road electron criteria [85]. Table 4.5 outlines the criteria for loose, medium and tight road electrons. The kinematic distributions for the electrons/tracks were as expected.

Selection Criteria	Loose Road Electron	Tight Road Electron
f_{EM}	> 0.6	> 0.9
E_T	> 0	> 0
E/p	$0.4 < \frac{E}{p} < 1.3$	$0.6 < \frac{E}{p} < 1.05$
Associated track p_T	$>$ 3GeV	$>$ 3GeV

Table 4.5: Criteria for loose and tight road electrons

CellNN Cluster Selection and Track Matching

CellNN clusters were required to have $p_T > 3GeV$ and to be matched to an electron track within R=0.2 corresponding to the size of a typical EM shower. In the MC sample, it was found that the two highest energy clusters belong to the e^+e^-pair from the J/Ψ when matching was possible. So the clusters were ordered in descending energy before matching to electron tracks that lie within R<0.2. It was a requirement that tracks could only be matched to one cluster, but the clusters could be matched to more than one electron. When this was the case, the closest match in η and ϕ was taken. Figure 4.16 shows a scatter plot of $E_{cluster}/p_{track}$ against $\triangle R$ between the cluster and the matched track for data (left) and MC (right). It can be seen that tracks and clusters match closely, and that the matching requirement is quite loose. Most clusters matched within R=0.075 of the track, and with no observable dependence on $E_{cluster}/p_{track}$. Table 4.6 gives the number of data and MC events passing the various selection criteria.

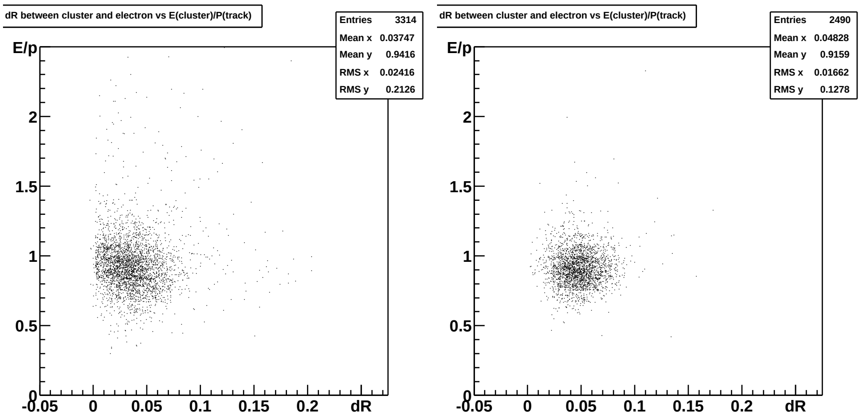

Figure 4.16: $E_{cluster}/p_{track}$ against $\triangle R$ between the cluster and the matched track for data (left) and MC (right)

4.3.3 Electromagnetic Scale

The cluster energy was binned in track momentum in 1GeV bins from 3 GeV to 14GeV, with a 4GeV-wide bin for track momentum 14GeV and 18 GeV. Figures 4.17(a) and 4.18(a) show histograms of cluster energy for a typical track momentum bin for data and MC respectively. Although the Gaussian fit describes the distributions well, a small tail can be seen at the higher end of the distributions for data and this is probably due to a small number of events where neutral energy in clusters has been matched to tracks. The mean from the Gaussian fits was plotted against the midpoint of the track momentum bin. Figures 4.17(b) and 4.18(b) show the resulting plots of 'average' cluster energy against track momentum for data and MC respectively. The cluster energy varies linearly with the track momentum so a straight line has been fitted to the points where:

$$E_{cluster} = p_0 p_{track} + p_1 \tag{4.4}$$

Selection Criteria	**Data Events**	**MC Events**
Number of events processed	6560	13200
Electron and track selection		
f_{EM}	6279	11195
Isolation cut	6233	11053
HMx8 cut	6167	10773
Fiducial region	5901	8680
Electron η cut	5897	8657
Cluster Selection		
Cluster η cut	3542	2176
Track Matching		
0 clusters matched	21	6
1 clusters matched	641	598
2 clusters matched (1st two in E)	2474	1622
3+ clusters matched	25	3

Table 4.6: Numbers of events passing selection criteria for data and MC event samples

setting $C = 1$. The calculated values for p_0 and p_1 are given in Table 4.7 for MC and data. As a closure test, a correction factor, C, dependent on the cluster energy:

$$C = \frac{E_{cluster} - p_1}{p_0} \tag{4.5}$$

was applied to the cluster energies and the invariant mass calculated.

If the correction is effective, the cluster invariant mass should move closer to the J/Ψ mass, and the mass resolution should improve. It can be seen in Figures 4.19(a) and 4.19(b) which show the cluster invariant mass distributions after correction, that the correction factor over-corrects. Table 4.7 shows the invariant masses and widths before and after correction for data and MC. To understand the over-correction, and to attempt to reduce it, the response was examined as a function of $E_{cluster}/p_{track}$. One would expect this quantity to be linearly related to the track momentum with no sharp change at low track momentum. Figure 4.20(a) shows $E_{cluster}/p_{track}$ against track momentum, derived using the same method, but binning $E_{cluster}/p_{track}$ in track momentum (rather than E) instead. There is a sharp increase in the gradient towards low track momentum. This clear bias in the first three or four bins is due to

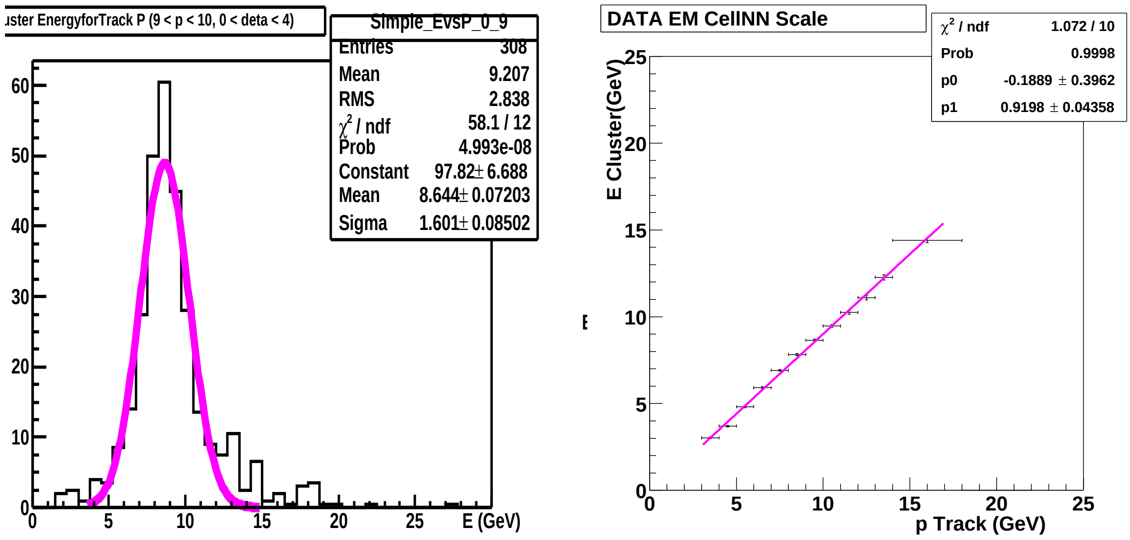

(a) Typical cluster energy distribution fitted with a Gaussian function for the momentum bin 9<p<10GeV.

(b) Cluster energy vs track momentum.

Figure 4.17: Electromagnetic scale for data.

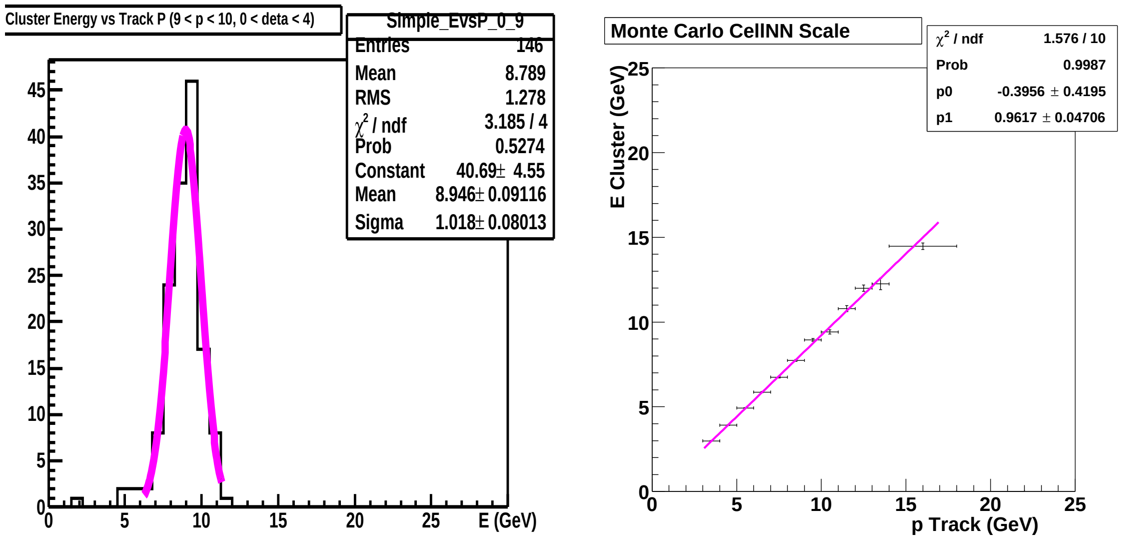

(a) Typical cluster energy distribution fitted with a Gaussian function.

(b) Cluster energy vs track momentum.

Figure 4.18: Electromagnetic scale for MC.

the $p_T > 3$GeV requirement in the track selection criteria. Omitting these bins from the fit (blue) does lead to a correction that is relatively better than that derived in

Figure 4.20(a), when using the position of the cluster invariant mass peak, but it still over-corrects. The 'corrected' mass peak using the factor omitting the biased momentum bins was 3.36 ± 0.54 GeV, still no better than not correcting the clusters at all. Since this alternative method was not effective, it was not pursued, instead returning to the original investigation of cluster energy against track momentum.

The EM scale was investigated to see if a variation in detector η could be observed. The same binning in energy was applied, but a further split according to η was also applied. Figure 4.20(b) shows the EM scale as a function of track momentum, for η bins $|\eta| <0.25$, $0.25< |\eta| <0.75$, $0.75< |\eta| <1.25$, $1.25< |\eta| <1.75$ and $1.75< |\eta| <2.25$. With the limited statistics available, there is no clear dependence on η. The MC sample showed a similar lack of variation in η.

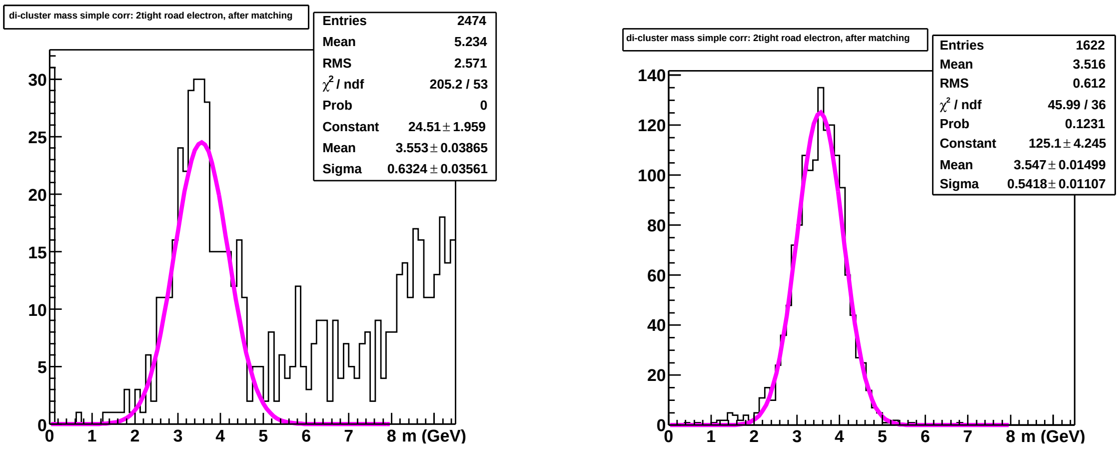

(a) Data (b) Monte Carlo

Figure 4.19: Cluster invariant mass after correction. The events above 5GeV in (a) are due to combinatorics.

Event Sample	p_1	p_2	$m_{J/\Psi}$ Before Correction	$m_{J/\Psi}$ After Correction
Data	0.92 ± 0.04	0.19 ± 0.40	2.87 ± 0.04	3.55 ± 0.63
Monte Carlo	0.87 ± 0.08	0.37 ± 0.86	2.72 ± 0.01	3.55 ± 0.54

Table 4.7: Data and Monte Carlo EM scale parameters (refer to Equation 4.4). Cluster invariant masses (GeV) before and after correction.

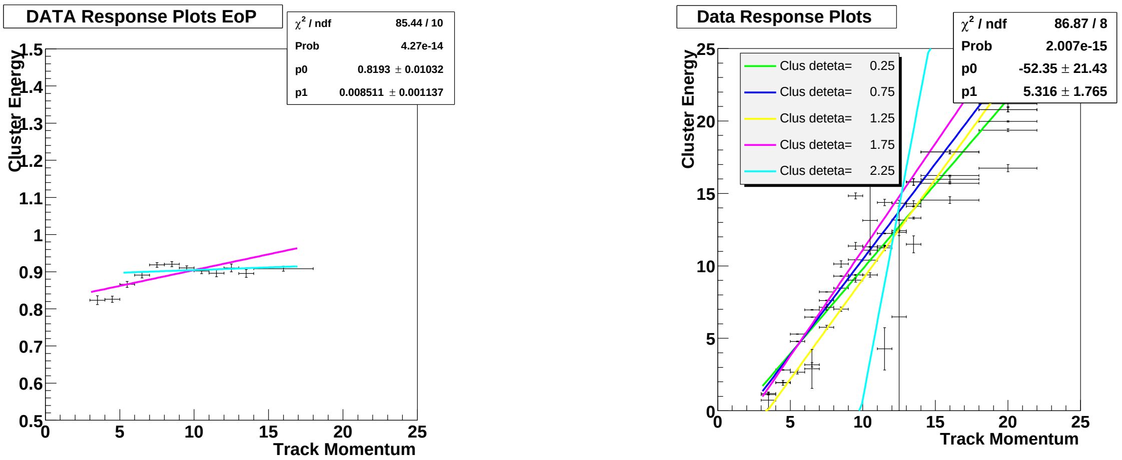

(a) (b)

Figure 4.20: a) Cluster energy/track momentum against track momentum, b) Cluster energy (GeV) against electron track momentum (GeV) for various η bins for data.

4.4 Conclusions

A scalar correction to b-jet energies was derived for events where a jet originating from a b-quark contains a muon and a neutrino from the direct or cascade decay of the b-quark. The correction is a function of the reconstructed muon energy and returns a scalar correction factor for the jet. It was derived from a sample of $t\bar{t} \rightarrow bWbW$ Monte Carlo events and it was shown to improve upon the basic jet energy scale correction for semileptonic b-jets. An alternative vector correction to semileptonic b-jets, also derived from MC, was considered and it showed a small improvement in the quality of the correction over that of the scalar correction. Closure tests on the scalar semileptonic correction show that for events where both b-jets decay semileptonically, the basic correction alone provides a 14% improvement in the $b\bar{b}$ mass resolution in $Z \rightarrow b\bar{b}$ and $H \rightarrow b\bar{b}$ decays (Monte Carlo event samples), whereas there is a 15% improvement in the mass resolution for events with no semileptonic decays. When the semileptonic correction is used, in addition to the basic jet energy scale correction, the improvement in resolution increases to 46% for events with 2 semileptonic decays, and remains at 15% for all events (inclusive b decays). The scalar [muonic] semileptonic correction was implemented in JES versions 4.2, 5.1 and 5.3 (p13 and p14 data).

As one of the necessary steps towards implementing an eflow algorithm at DØ , a electromagnetic cluster scale was derived using the momenta of low-energy matched-tracks. The energy of the clusters is linearly related to the track momenta as is clearly shown in Figures 4.17(b) and 4.18(b). There is no discernible offset between the cluster energies and the track momentum. The offsets (p_1) listed in Table 4.7 are consistent with zero (within statistical errors) and are sensitive to the binning of cluster energy in track momentum. There were insufficient statistics in either the MC or data samples to detect any variation in the scale with detector η. Since no η-dependence could be determined, only a scale factor correction could be derived as expected. There is no real difference between using this method, and obtaining a correction by calculating the factor needed to shift the cluster J/Ψ mass peak to the correct place. In fact, with so few events, this second method might be more effective since the correction factor overcompensates so there is no real gain in resolution. It is likely that, with larger event samples, a non-linearity in track momentum and a variation with η would be observed, and a more effective correction could be found.

It was decided, in 2004, after this study and others conducted by the eflow working group, that it was more important to do a full calibration of the current calorimeter rather than invest further effort straightaway in a full eflow algorithm. The previous intercalibration of the calorimeter was carried out during Run I of the experiment and, since then, an extra layer has been added to the tracking system and the Tevatron bunch spacing has decreased, which have changed the response of the calorimeter. A more accurate calibration of the detector is underway [86], [87]. A basic version of the eflow algorithm has been implemented called *TrackCal*[88]. Figure 4.21 shows the improvement in jet E_T resolution obtained using this algorithm in initial studies. TrackCal does take advantage of the tracker's better momentum resolution for low energy charged particles and combines this with jet energy measurements made in the calorimeter. The algorithm combines hadronic charged tracks and jets reconstructed in the calorimeter only using the simple cone algorithm. Tracks with a p_T between 0.5GeV and 25GeV are propagated to the calorimeter surface and extrapolated to see if they lie within the R=0.5 jet cone. If they lie within the jet, their momentum from the tracking system is added to that of the jet. To compensate for the energies of these particles that have already

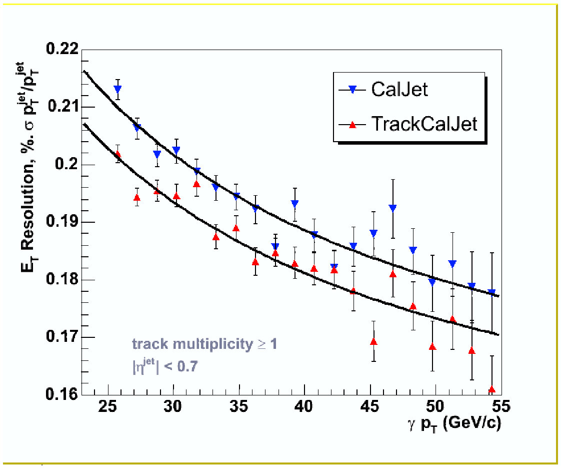

Figure 4.21: MC jet E_T resolution for cone R=0.7. Upper, blue points are for calorimeter jets only, lower, red points are for TrackCal jets.

been measured and included within the jet energy, the average calorimeter energy deposition for a charged hadronic track is subtracted. This average energy is derived from the single pion response obtained from Monte Carlo.

Chapter 5

Search for the Standard Model Higgs Boson

5.1 Introduction

The search for the Higgs boson, one of the truly basic particles and the least experimentally verified part of the Standard Model, dominates the Run II physics programme at DØ , and this analysis focuses on a search for the Standard Model Higgs boson. If the Higgs boson exists, the Tevatron is well-placed to produce evidence of it, and perhaps even discover it as it operates at a centre of mass energy that means it has sensitivity in the right mass range ($\lesssim$ 200GeV) [6]. The phenomenology of the Higgs boson and the global search strategies at the Tevatron are well known and have been studied in detail in [89][7].

Direct searches at LEP2 set a 95% C.L. lower limit on the mass of the standard model Higgs boson, m_H, of 114.4GeV [26]. Indirect constraints favour a light Higgs boson [3].

At the Tevatron, there are four important Higgs boson production mechanisms, and Figure 5.1 shows the production cross-sections as a function of the Higgs mass, from [7]. The most significant obstacle for Higgs searches is filtering out the large QCD background of $p\overline{p}$ collisions and this, in turn, affects which Higgs production mechanisms and decay channels may be most easily searched for.

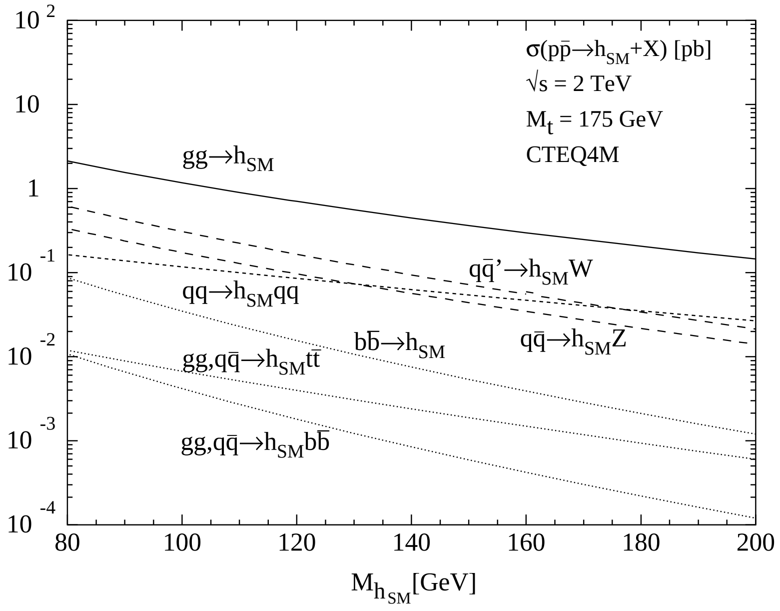

Figure 5.1: Higgs production cross-sections (pb) at the Tevatron for the various production mechanisms as a function of the Higgs mass, taken from [6].

The primary production mechanism is from $g\bar{g}$ fusion where the Higgs is produced via a top quark loop. The two next most frequent production mechanisms, at cross-sections an order of magnitude lower, are the Higgs-strahlung processes which are the associated production of a Higgs and a W/Z boson, shown in Figure 5.2. The Higgs may also be produced in the $Hq\bar{q}$ channel, but a search in this channel is difficult due to the large QCD background. For a light Higgs ($m_H \lesssim$135GeV) the Higgs decays predominantly to $b\bar{b}$; for a heavier Higgs, it decays most often to $WW^{(*)}$. The dominant decay modes and their branching ratios for a Standard Model Higgs are shown in Figure 5.3 as a function of Higgs mass. For a low-mass Higgs, large QCD jet background prevents the $g\bar{g}$ mode from being exploited. So instead, the vector associated production needs to be used, triggering on the vector boson, and finding the Higgs from its decay to b-jets. The high branching ratio of $Z \rightarrow \nu\overline{\nu}$ of 20% then means that the $ZH \rightarrow \nu\bar{\nu}b\bar{b}$ decay is potentially the single most sensitive channel for a light Higgs boson at the Tevatron.

However, the lack of visible leptons and the presence of only two jets in the final state makes this channel difficult to detect at the Tevatron. To detect this channel, the presence of large missing transverse energy ($\not{E}_T$) must be relied on and the jets must be b-tagged. This strategy creates, first and foremost, problems for the

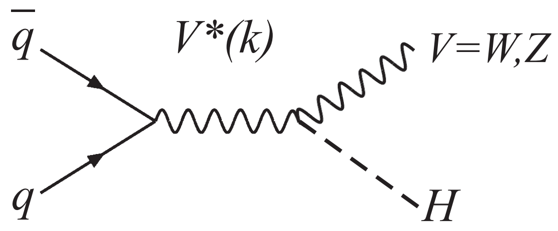

Figure 5.2: Feynman diagram of the associated production of a Higgs boson and a vector boson.

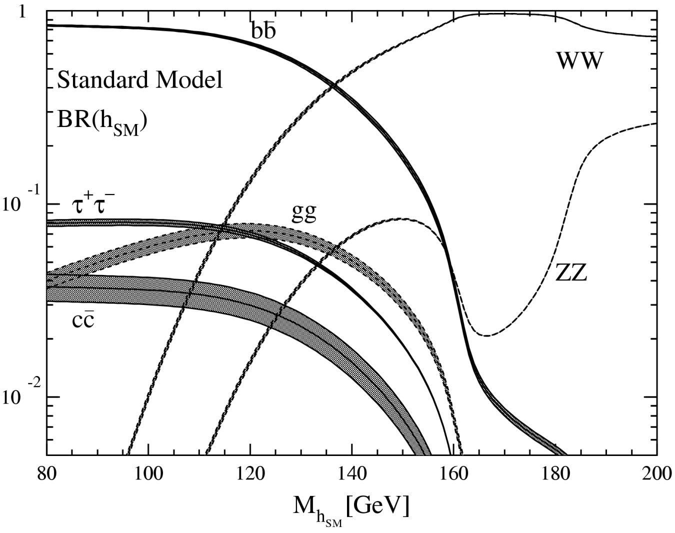

Figure 5.3: Branching ratios of the dominant decay modes of the Standard Model Higgs boson [7].

trigger selection in order to keep the trigger rates at an acceptable level. Secondly, it creates problems for the estimation of any instrumental backgrounds arising from calorimeter miscalibrations which can lead to high $\not{E}_T$ signals with the presence of jets from QCD processes.

This chapter describes a search for the Standard Model Higgs boson produced in association with a Z boson, where the Higgs decays to a $b\bar{b}$ pair and the Z boson decays to $\nu\bar{\nu}$. The data sample used is that taken with the v13 trigger list which contains four new triggers that select events with two acoplanar jets and $\not{E}_T$. This analysis is carried out using a series of selection criteria which have been optimised on Monte Carlo (MC) simulations of the main background decay channels. The MC and data samples are described in the first section. A sequential cuts analysis is carried out and described in Section 5.3. This analysis allows the effects of cutting on the key signal/background discriminating variables to be observed separately, and a comparison of MC and data to be made. Advanced techniques to optimise the MC event selection criteria and the b-tagging have been used to improve the sensitivity, and these are evaluated in Section 5.4. The systematic uncertainties and results for the limit on the ZH cross-section are given in Sections 5.5 and . This analysis is based on the preliminary DØ analysis presented at Moriond '05 [90] using the data taken with the v12 trigger list (without acoplanar triggers).

5.2 Data and Monte Carlo Event Samples Used

5.2.1 Data Set

The analysed data were taken from the 28^{th} of June 2004 (run 194567) to the 23^{rd} of August 2004 (run 196584), with a total luminosity of $55.25pb^{-1}$. The data were taken with the v13 version of the trigger list which contained four new triggers that select events with acoplanar jets and missing transverse energy. The data taken were skimmed for events passing one or more of the 10 triggers listed in Figure 5.4. Of these 10 triggers, only events firing four of them are of interest to this analysis and these are described later in this section. The data were reconstructed with p14.06.01 [91], passed through the thumbnail correction software p14.fixtmb2.02 [92] and passed through d0correct v8.1 [66]. Bad calorimeter, muon, CFT and SMT runs from the Run Quality Database were eliminated, removing a total of 193 bad runs. Furthermore, a total of 37973 bad luminosity blocks were eliminated.

5.2.2 Monte Carlo

The signal and background samples used are listed in Tables 5.2 and 5.3, along with their cross-sections×branching ratios and their SAM[1] request ID numbers. The $Z+jets$ and the $W+jets$ background samples used in this analysis are generated by

---

[1] SAM: Sequential Access Metadata. This is the storage facility for our MC and data, stored under ID numbers.

ALPGEN [93] with the showering and hadronisation processes modelled by Pythia [74], with p14 minimum bias events overlain . The cross-sections × branching ratios for these samples are based on leading order ALPGEN calculations multiplied by a K-factor[2] obtained from MCFM[3], [94]. The main backgrounds that are simulated by the MC include Zjj/Zbb, W+jets/Wbb, WZ, ZZ, and top quark production with jets or escaping leptons. The instrumental background, which is mainly QCD multijet events, cannot be effectively modelled in MC due to the large cross-section and small acceptance, so this background is extracted from data and described in Section 5.3.3.

5.2.3 Trigger Terms

The four trigger terms of interest for this analysis were the set of 'acoplanar' [95] triggers which were all in the same exposure group[4] . The v13 trigger list was designed to run up to luminosities of $10^{32} cm^{-2} s^{-1}$. This set of acoplanarity triggers share the same Level 1 and Level 2 trigger requirements and some Level 3 requirements. In addition, these four triggers each have further individual L3 requirements and these are listed below with the common requirements in Table 5.1.

---

[2] K-factor: also called a fudge factor, this is a way to express unknown or difficult-to-express effects with a correction factor. A K-factor is used in comparing cross-sections calculated up to leading order (LO), to the same up to next-to-leading order (NLO) ($K = \sigma_{NLO}/\sigma_{LO}$), or in comparing observed values of cross-sections to those calculated.

[3] MCFM is a parton-level Monte Carlo program which gives NLO predictions for processes at hadron colliders

[4] Triggers in a Trigger List sharing a set of scalers are called an Exposure Group

Trigger	JT1_ACO_MHT_ER2	JT1_ACO_MHT_BDV	JT1_ACO_MHT_HT	JT1_ACO_MHT_LM0
L1	Three calorimeter towers with an $E_T < 5$GeV			
L2	$\not{E}_T$ from jets > 20GeV Two jets, with the leading two separated by $0 < \phi < 168.75°$			
L3	One jet with a $\mathrm{E}_T > 9$GeV The ϕ angle between the two leading jets $< 170°$ The vector sum of the p_T of all jets (with a $p_T > 15$GeV and with $\lvert\eta\rvert < 2.5$) must be > 30GeV			
Other	Requires an extra road electron.	Requires one jet to be b-tagged and a primary vertex with $\lvert z\rvert < 35$cm.	Requires that scalar sum of p_T of all jets (with $p_T > 15$GeV and with $\lvert\eta\rvert < 2.5$) must be > 50GeV.	Requires a loose muon to be present at L3.

Table 5.1: Details of the L1, L2 and L3 trigger requirements for the four acoplanarity triggers used in this analysis.

Process	Cross-section × BR (pb)	SAM request id	Number of Events
$ZH \to \nu\bar{\nu}b\bar{b}$ ($M_H = 105$ GeV)	0.0221	13571	9000
$ZH \to \nu\bar{\nu}b\bar{b}$ ($M_H = 115$ GeV)	0.0152	16142	31814
$ZH \to \nu\bar{\nu}b\bar{b}$ ($M_H = 125$ GeV)	0.00953	16141	31800
$ZH \to \nu\bar{\nu}b\bar{b}$ ($M_H = 135$ GeV)	0.00521	13752	33500
$ZH \to e\bar{e}b\bar{b}$ ($M_H = 105$ GeV)	0.00372	11661	5000
$ZH \to e\bar{e}b\bar{b}$ ($M_H = 115$ GeV)	0.00255	11662	5000
$ZH \to e\bar{e}b\bar{b}$ ($M_H = 125$ GeV)	0.0016	11663	5000
$ZH \to e\bar{e}b\bar{b}$ ($M_H = 135$ GeV)	0.00088	11664	5000
$ZH \to \mu\bar{\mu}b\bar{b}$ ($M_H = 105$ GeV)	0.00372	11667	5000
$ZH \to \mu\bar{\mu}b\bar{b}$ ($M_H = 115$ GeV)	0.00255	11668	5000
$ZH \to \mu\bar{\mu}b\bar{b}$ ($M_H = 125$ GeV)	0.00160	11669	5000
$ZH \to \mu\bar{\mu}b\bar{b}$ ($M_H = 135$ GeV)	0.00088	11670	5000
$ZH \to \tau\bar{\tau}b\bar{b}$ ($M_H = 105$ GeV)	0.00372	11675	5000
$ZH \to \tau\bar{\tau}b\bar{b}$ ($M_H = 115$ GeV)	0.00255	11676	5000
$ZH \to \tau\bar{\tau}b\bar{b}$ ($M_H = 125$ GeV)	0.00160	11677	5000
$ZH \to \tau\bar{\tau}b\bar{b}$ ($M_H = 135$ GeV)	0.00088	11678	5000
$WH \to e\nu b\bar{b}$ ($M_H = 105$ GeV)	0.0207	11643	5000
$WH \to e\nu b\bar{b}$ ($M_H = 115$ GeV)	0.0139	11644	5000
$WH \to e\nu b\bar{b}$ ($M_H = 125$ GeV)	0.0086	11645	5000
$WH \to e\nu b\bar{b}$ ($M_H = 135$ GeV)	0.0046	11646	5000
$WH \to \mu\nu b\bar{b}$ ($M_H = 105$ GeV)	0.0207	11649	5000
$WH \to \mu\nu b\bar{b}$ ($M_H = 115$ GeV)	0.0139	11650	5000
$WH \to \mu\nu b\bar{b}$ ($M_H = 125$ GeV)	0.0086	11651	5000
$WH \to \mu\nu b\bar{b}$ ($M_H = 135$ GeV)	0.0046	11652	5000
$WH \to \tau\nu b\bar{b}$ ($M_H = 105$ GeV)	0.0207	11655	5000
$WH \to \tau\nu b\bar{b}$ ($M_H = 115$ GeV)	0.0139	11656	5000
$WH \to \tau\nu b\bar{b}$ ($M_H = 125$ GeV)	0.0086	11657	5000
$WH \to \tau\nu b\bar{b}$($M_H = 135$ GeV)	0.0046	11658	5000

Table 5.2: Table of signal Monte Carlo event samples used.

Process	Cross-section × BR (pb)	SAM request id	Number of Events
$Zbb \rightarrow \nu\nu b\bar{b}$	3.25	16376 16377 16378 16379	68750
$Zbb \rightarrow e\bar{e}b\bar{b}$	0.67	11407 11408	98000
$Zbb \rightarrow \mu\bar{\mu}b\bar{b}$	0.67	11409 11410	96500
$Wbb \rightarrow e\nu b\bar{b}$	4.16	11298 11299	99500
$Wbb \rightarrow \mu\nu b\bar{b}$	4.16	11300 11301	99000
$Wbb \rightarrow \tau\nu b\bar{b}$	4.16	13721 13727	18750
$Zjj \rightarrow \nu\bar{\nu}jj$	174.49	15008 15009 18037 18039 18353 18354 18355 18356 18357 18358	104500
$Zjj \rightarrow e\bar{e}jj$	28.3	15289 15290 15513 15514 15517 15518	71250
$Zjj \rightarrow \mu\bar{\mu}jj$	28.3	15284 15291 15295 15301	49750
$Zjj \rightarrow \tau\bar{\tau}jj$	28.3	15587 15589 15593 15595 15597 15598 15605 15792	83250
$Wjj \rightarrow e\nu jj$	287.36	10749 10750 10751 10752 15221 15224 15226 15229 15230 15272 15298 15317 15511	243000
$Wjj \rightarrow \mu\nu jj$	287.36	10727 10740 10741 10742 15222 15223 15225 15228 15271 15273 15287 15288 15337 15393 15112 15516	239750
$Wjj \rightarrow \tau\nu jj$	287.36	15584 15585 15586 15590 15594 15602	30250
$Zj \rightarrow \tau\bar{\tau}j$	81.32	15567 17090	96500
$Wj \rightarrow \tau\nu j$	841.93	15442 15566	97750
$t\bar{t} \rightarrow bl\nu\bar{b}l\nu$ $(M_t = 175GeV)$	0.784	15181 15385	57500
$t\bar{t} \rightarrow bl\nu\bar{b}jj$ $(M_t = 175GeV)$	3.116	15177 15326 15343 15344 15345	191300
$t\bar{t} \rightarrow bjj\bar{b}jj$ $(M_t = 175GeV)$	2.8	15182 15386 15890	105250
$ZZ \rightarrow \nu\bar{\nu}b\bar{b}$	0.086	10144	52025
$ZZ \rightarrow \nu\bar{\nu}c\bar{c}$	0.067	10143	56860
$WZ \rightarrow l\nu jj$	0.338	10188	23000
$WZ \rightarrow e\nu b\bar{b}$	0.059	17095	73000
$WZ \rightarrow \mu\nu b\bar{b}$	0.059	17094	39500

Table 5.3: Table of background Monte Carlo event samples used

Figure 5.4 shows the inclusive distribution of fired triggers in the skim where the numbers correspond to the triggers listed in the table to the right. Note 2CJT5_mp3_pf1 is a mark and pass trigger[5] and MHT20_L2L0_PVZ is only present in the v12 trigger list. The other triggers in the list, 1, 2, 3 and 4 are in different exposure groups and hence are not used for this analysis.

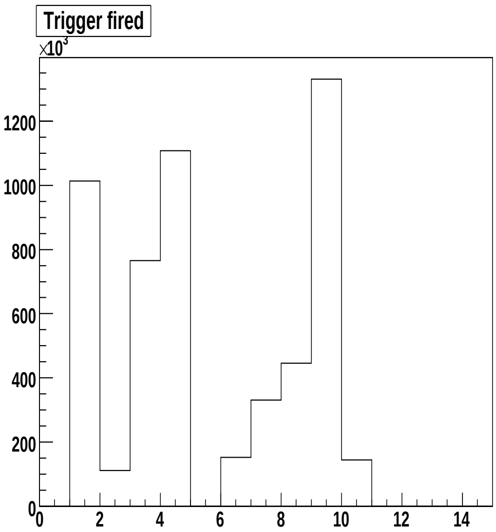

No.	Trigger Name
1	JT2_MHT25_HT
2	JT6_ACO_MHT_LM0
3	JT_25TT_NG
4	JT_45TT
5	MHT20_L2L0_PVZ
6 ✓	JT1_ACO_MHT_LM0
7 ✓	JT1_ACO_MHT_ER2
8 ✓	JT1_ACO_MHT_BDV
9 ✓	JT1_ACO_MHT_HT
10	2CJT5_mp3_pf1

Figure 5.4: Inclusive distribution of fired triggers for the v13 data set.

5.3 Event Selection

The event selection is a series of sequential cuts that can be considered to be in three stages:

1. **Basic Event Selection** This selects good quality physics objects, selects on the basic topology of the event, and helps to remove some of the physics backgrounds from $t\bar{t}$ events and instrumental backgrounds that are generic multijet events.

---

[5] A "mark and pass" trigger passes and writes to tape every nth event at Level 3, regardless of whether the event has passed any L3 filters. It provides a set of L3 unbiased events, useful for studying L3 trigger efficiencies.

2. **Instrumental Background Selection** This makes further reductions in the large instrumental background, through comparison of the MC physics backgrounds with the data to identify the characteristics of the instrumental backgrounds by a process of elimination.
3. **b-tagging** This, as the name suggests, identifies b-jets in the event so that events with two acoplanar b-jets can be identified. This also includes corrections to the MC to correct the b-tagging efficiencies to that of data.

Physics Objects The physics objects used in the analysis are the standard corrected objects obtained from d0correct. For jets, the standard JES (version 5.3 [96]) is applied without the semileptonic correction. The $\not\!\!E_T$ is taken from the calorimeter, muon-corrected value, ignoring the unclustered energy in the CH layer of the hadronic calorimeter[6]. The H_T is calculated as the vector sum of the p_T of all jets with a $p_T > 15$GeV and with $|\eta| < 2.5$. The scalar H_T instead is calculated as the simple scalar p_T sum of all the jets in the event. A further variable used is the missing E_T from tracks, $trk\not\!\!E_T$. This is simply the vector sum of the p_T of all tracks with at least 14 CFT hits, a DCA[7] to the primary vertex of $<$ 2mm and a distance from the primary vertex in z less than 5 mm. The tracks are also required to be associated to the same vertex as the leading jet in the event.

5.3.1 Basic Event Selection

Basic Selection Criteria

The basic event selection is designed to select events with fundamental signal like properties (two jets and large missing E_T) and to reject obvious background events. The basic event selection is as follows:

Cut 1 No bad runs

Cut 2 No bad calorimeter or luminosity blocks

---

[6] The CH layer of the calorimeter is noisy so any unclustered energy is ignored.

[7] DCA:distance of closest approach.

Cut 3 Pass trigger requirements (see Section 5.2.1)

Cut 4 Jet Requirements: two jets with a $p_T > 20$GeV and $|\eta| < 2.5$ originating from the same vertex. The presence of a vertex with $|z| < 50$ cm, with at least 5 attached tracks.

Cut 5 $\not\!\!E_T > 20$GeV.

Cut 6 Scalar $H_T < 210$GeV.

Cut 7 No isolated good electrons or muons with a $p_T > 8$GeV.

Cut 8 $\triangle\phi(dijet) < 165^o$

This event selection has been optimised as part of this analysis to improve the sensitivity and this is discussed in detail in Section 5.4. Cuts, 4, 5 and 8 select the topology of the events, mainly eliminating QCD di-jet back-to-back events. Cuts 6 and 7 are designed to eliminate $t\bar{t}$ events; if the top quarks decay to jets the total scalar sum of the jets in the events will be large and conversely if the top quarks decay to leptons via a W boson, then the isolated lepton cut will reject these events. The isolated lepton cut also eliminates the leptonic decays (muon and electron) of Z and W bosons.

Data Distributions After Basic Event Selection

Figure 5.5 show the leading and next-to-leading jet η, ϕ and $\eta - \phi$ distributions. Figures 5.6 and 5.8 show the $\not\!\!E_T$ ϕ and the $\not\!\!E_T$ x and y components. Figures 5.7 and 5.9 show the same distributions for the $\not\!\!H_T$ in the events.

As can be seen in Figure 5.5, with these basic cuts (cuts 1 to 8) alone, the jet distributions of η, ϕ and $\eta - \phi$ are very irregular. The ϕ (Figure 5.5a) of the leading jet is broadly peaked to low ϕ values and the leading jet η distribution (Figure 5.5c) has a large hole in the ICR region. The next-to-leading jet distribution is somewhat flatter, however, there is a spike in the $\eta - \phi$ distribution which is not run-dependent. Furthermore, there is no hole in the ICR region in the η distribution.

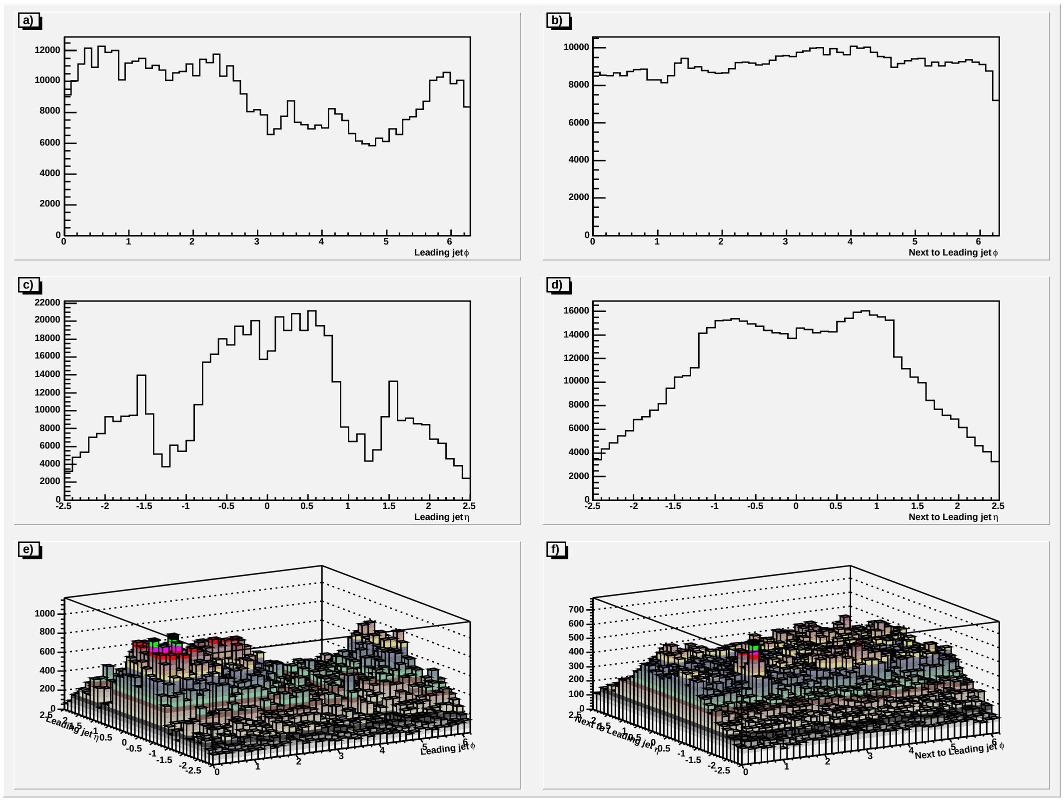

Figure 5.5: Distributions for the leading and next-to-leading jet in the event after basic cuts. a)ϕ-distribution for leading jet, b)ϕ-distribution for next-to leading jet, c)η-distribution for leading jet, d)η-distribution for next-to leading jet, e)$\eta - \phi$-distribution for leading jet and f)$\eta - \phi$-distribution for next-to leading jet.

All the $\not\!\!E_T$ (Figure 5.6) and $\not\!\!H_T$ (Figure 5.7) distributions are broadly similar except for the absence of the low tail in the actual $\not\!\!E_T$ distribution (due to the $\not\!\!E_T$ cut in the basic selection) and in the ϕ distribution at $\phi > 5$. There are clear asymmetries in the $\not\!\!E_T$ and $\not\!\!H_T$ distributions, the origins of which are not clear, but are thought to be the result of a combination of miscalibrations in the calorimeter, instrumental backgrounds, trigger effects, presence of "bad" and noise jets in the event, etc. In addition to this asymmetries in the ϕ distribution, the x and y-components show the a dip around zero, characteristic of some of the problems with DØ tracking. These are beyond the scope of this thesis and are not discussed further here.

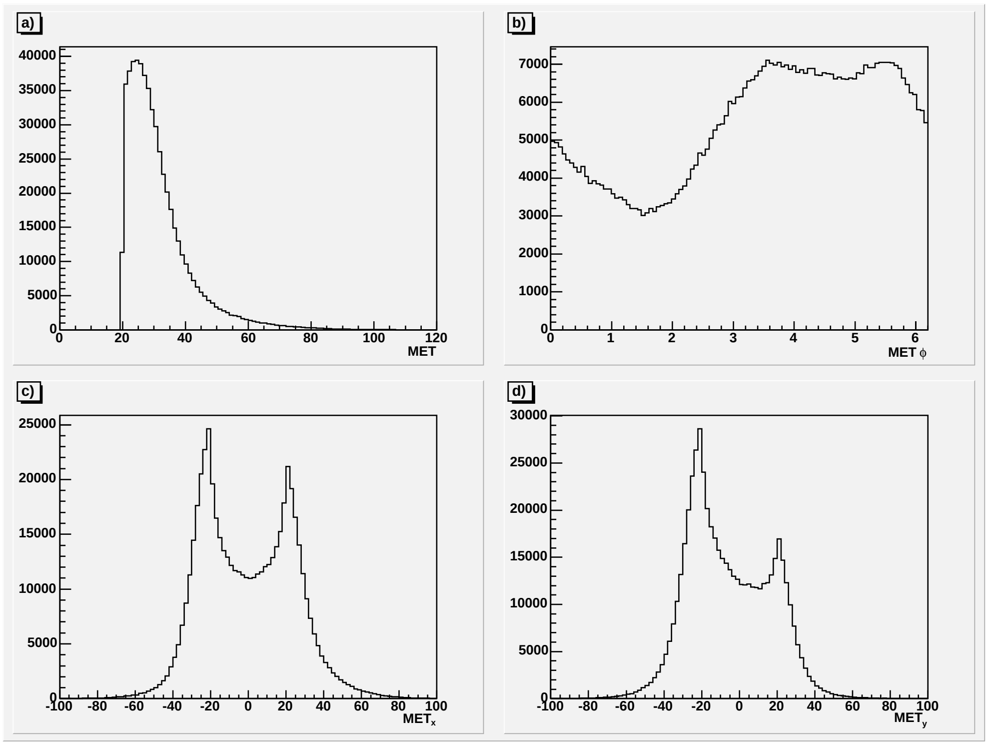

Figure 5.6: $\not\!\!E_T$ distributions after basic cuts and a two-jet requirement. Top left: $\not\!\!E_T$ Top right: $\not\!\!E_T$ - ϕ which shows the asymmetry that is thought to be due to calorimeter miscalibrations, instrumental backgrounds, trigger effects and 'noise' jets in the event. Bottom left: $\not\!\!E_T$ x-component Bottom right: $\not\!\!E_T$ y-component. In addition to the asymmetry mentioned visible in the ϕ distribution, the x and y-components show the a dip around zero characteristic of some of the problems with DØ tracking.

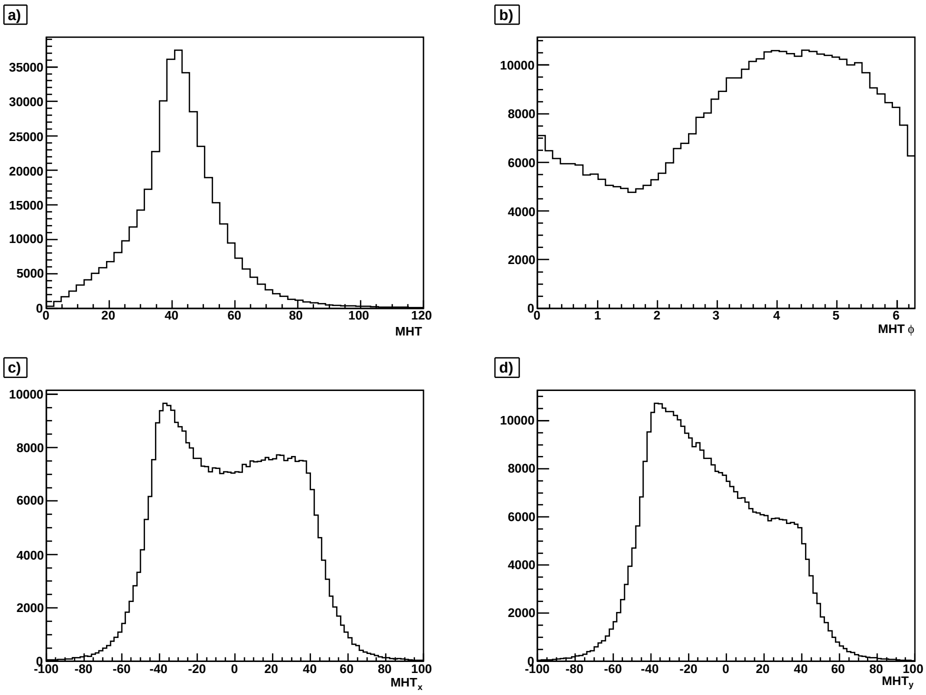

Figure 5.7: $\not\!\!H_T$ distributions after basic cuts and a two-jet requirement. Top left: $\not\!\!H_T$ and top right: $\not\!\!H_T$ ϕ distribution. Bottom left: x-component $\not\!\!H_T$ distribution. Bottom right: y-component $\not\!\!H_T$ distribution.

To try to understand if the asymmetry is solely due to the miscalibrations and the effect of instrumental backgrounds, the effects of imposing higher $\not\!\!E_T$ and $\not\!\!H_T$ cuts were considered. If this were the case, then it could be assumed that the asymmetries would decrease when imposing higher $\not\!\!E_T$ and $\not\!\!H_T$ cuts. Figures 5.8 and 5.9 show the effect on the ϕ variation as tighter cuts are imposed on these variables. It can be seen that $\not\!\!H_T$ ϕ distribution improves after the $\not\!\!H_T > 80$GeV cut is imposed. The $\not\!\!E_T$ ϕ distribution exhibits large peaks around the $0/2\pi$ region, whereas the central ϕ distribution improves with the higher cuts. The possible reason for these inhomogeneities is discussed further in the next section.

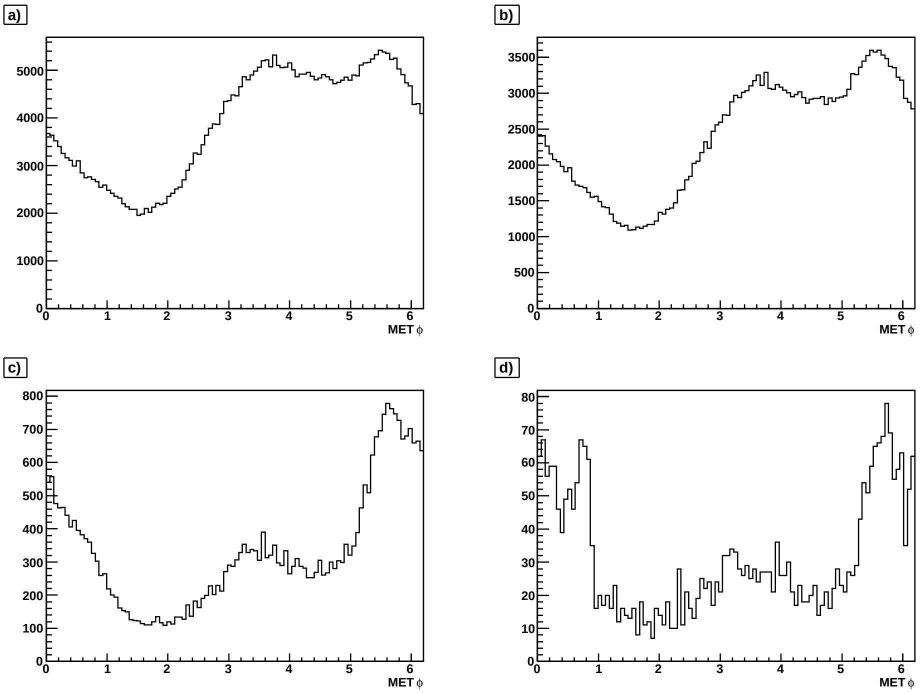

Figure 5.8: $\not\!\!E_T$ ϕ distributions after basic cuts and after imposing varying $\not\!\!E_T$ cuts. Top left: $\not\!\!E_T$ ϕ distribution. Top right: $\not\!\!E_T$ ϕ distribution and $\not\!\!E_T$ >30GeV. Bottom left: $\not\!\!E_T$ ϕ distribution and $\not\!\!E_T$ >50GeV. Bottom right: $\not\!\!E_T$ ϕ distribution and $\not\!\!E_T$ >80GeV. It can be seen that the central asymmetry in the ϕ-distribution decreases with increasing $\not\!\!E_T$ cuts.

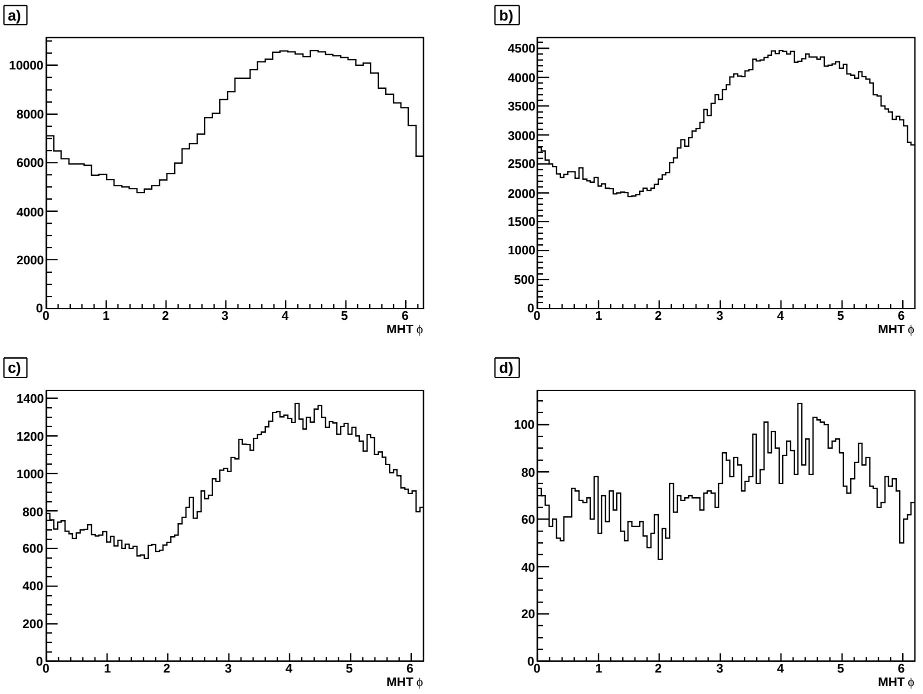

Figure 5.9: $\not{H}_T$ ϕ distributions after basic cuts and after imposing varying $\not{H}_T$ cuts. Top left: $\not{H}_T$ ϕ distribution after basic cuts. Top right: $\not{H}_T$ ϕ distribution and $\not{H}_T$ >30GeV Bottom left: $\not{H}_T$ ϕ distribution and $\not{H}_T$ >50GeV Bottom right: $\not{H}_T$ ϕ distribution and $\not{H}_T$ >80GeV. It can be seen that the $\not{H}_T$ ϕ distribution improves after imposing the $\not{H}_T$ >80GeV cut.

Further Analysis of the Missing E_T Distribution

Shown in Figure 5.10 are the $\not\!\!E_T$ distributions (as in Section 5.3.1) for events with no bad or noise jets [8]. The analysis standard cut is to exclude events where the leading and next-to-leading jet are noise/bad jets. These figures exclude events where *any* jets are noise/bad jets. The distributions for jets and for $\not\!\!H_T$ are very similar to Figures 5.8 and 5.9. However, as seen in Figure 5.10 the large spikes in $\not\!\!E_T$ (ϕ) at $0/2\pi$ have disappeared. However the general shape of the ϕ distribution is similar.

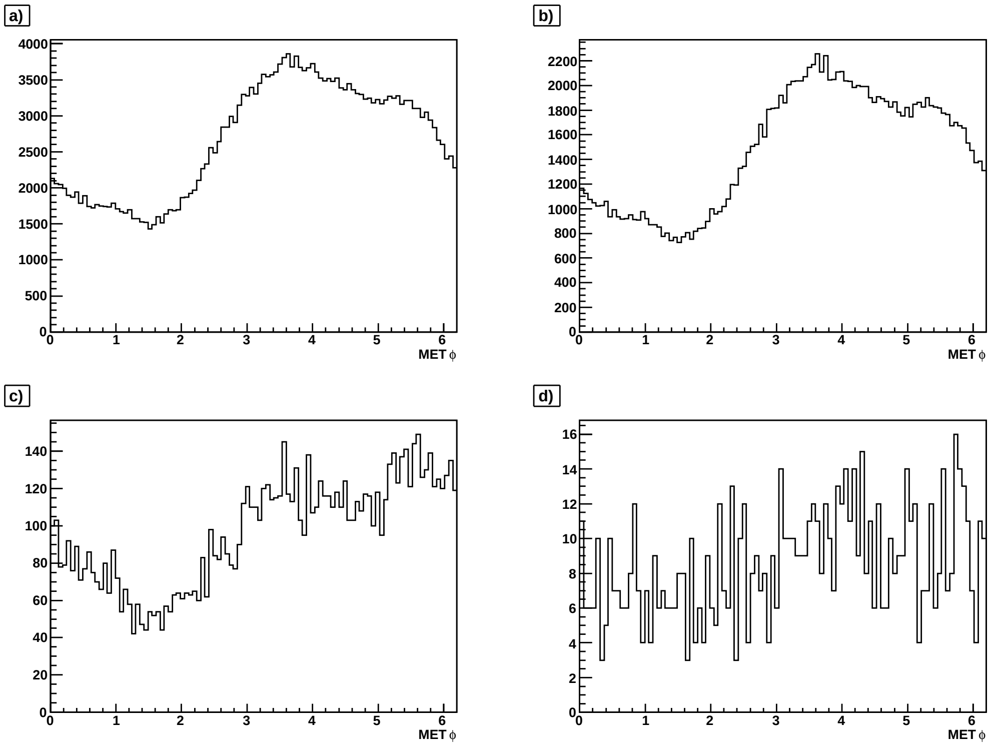

Figure 5.10: $\not\!\!E_T$ - ϕ distributions after basic cuts and with varying $\not\!\!E_T$ cuts, for events with no bad or noise jets

To compare the distributions with those of another sample without the jet trigger bias, a 1MULOOSE skim[9] sample was examined. Figures 5.11 - 5.13 show distributions for events in the 1MULOOSE skim. In the muon skim, events have been triggered by muon triggers and hence should give a sample without the jet

---

[8] Noise jets are defined as jets failing the L1 criteria and bad jets failing any other jet identification cut

[9] Data skim for events with one loose muon as defined by the muon id group in DØ Note 4350

trigger bias and with less QCD background (there should be a large fraction of W+jet events). To create a $\not\!\!E_T$ signal, any good isolated muons have their momenta reversed and added to the $\not\!\!E_T$ in the event. Interestingly, for this sample, the leading jet does not have a hole in the ICR in the η distribution. Furthermore, the jet ϕ distributions are a lot flatter although still show similar features. The $\not\!\!E_T$ and $\not\!\!H_T$ distributions still exhibit a similar structure to the jets from the analysis data sample. This would really indicate that although a trigger bias accounts for some of the structure, the major features are trigger-independent and are related to the features of the hardware or the reconstruction process. Fortunately, it is possible to impose instrumental cuts to eliminate these inhomogeneities. These cuts are described in detail in Section 5.3.2.

5.3.2 Instrumental and Other Selection Criteria

To compensate for the differences and the inhomogeneities in the distributions after the basic event selection, various cuts are imposed to deal with the *instrumental backgrounds* which give rise to these asymmetries. For events with a 'physical origin' the $\not\!\!H_T$, $\not\!\!E_T$ and $trk\not\!\!E_T$ should all point in the same direction and should be correlated. Furthermore, di-jet events in which one of the jets has been mis-measured, so giving a $\not\!\!E_T$ signal, will have the $\not\!\!E_T$ in the same ϕ-direction as one of the jets. In the case of $trk\not\!\!E_T$, this above statement assumes that the fake track distribution and the tracking efficiency is flat in ϕ. Following earlier work for the v12 analysis [90], the cuts below were applied, after those listed in Section 5.3.1. These cuts are motivated and explained following their listing:

Cut 9 $min\Delta\phi(\not\!\!E_T, jets) > 0.15$

Cut 10 $\not\!\!E_T > -40 \times min\Delta\phi(\not\!\!E_T, jets) + 80GeV$

Cut 11 $\Delta\phi(\not\!\!E_T, trk\not\!\!E_T) < 1.0$

Cut 12 $0 < Asym(\not\!\!E_T, trk\not\!\!E_T) < 0.6$, where $Asym(\not\!\!E_T, trk\not\!\!H_T) \equiv (\not\!\!E_T - trk\not\!\!E_T)/(\not\!\!E_T + trk\not\!\!E_T) < 0.6$

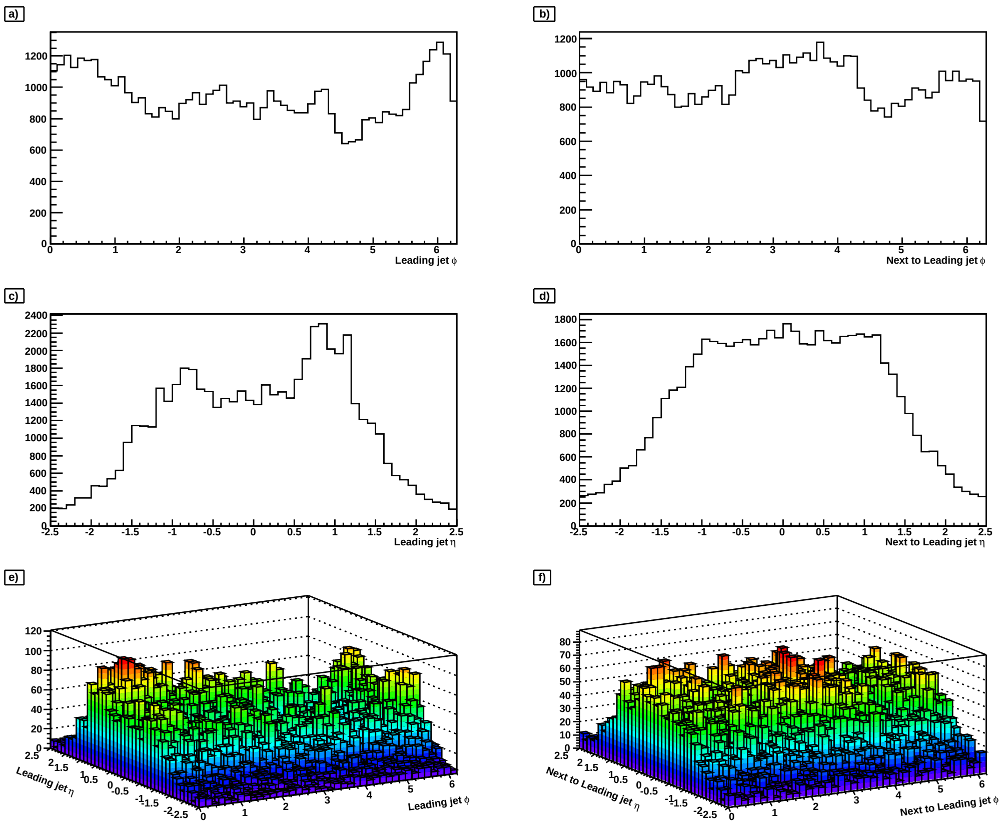

Figure 5.11: Distributions for the leading and next-to-leading jet in the event after basic cuts, for the muon-triggered sample. Distributions in the left column are for the leading jet, and in the right column for the next-to-leading jet. Top to bottom are shown the ϕ distributions, the η distributions and the $\eta - \phi$ distributions.

Cut 13 $-0.1 < Asym(\not\!\!E_T, \not\!\!H_T) < 0.2$, where $Asym(\not\!\!E_T, \not\!\!H_T) \equiv (\not\!\!E_T - \not\!\!H_T)/(\not\!\!E_T + \not\!\!H_T) < 0.2$

Cut 14 trk$\not\!\!E_T > 20$GeV

Cut 15 $|trk\not\!\!E_T - trk\not\!\!E_T(dijet)|/trk\not\!\!E_T < 0.2$

Cut 16 Both jets taggable

Cut 17 Both jets are b-tagged

Cuts 9 to 15 were motivated by comparing the data, MC signal and MC background distributions of the relevant variables, and placing the cuts by eye to remove

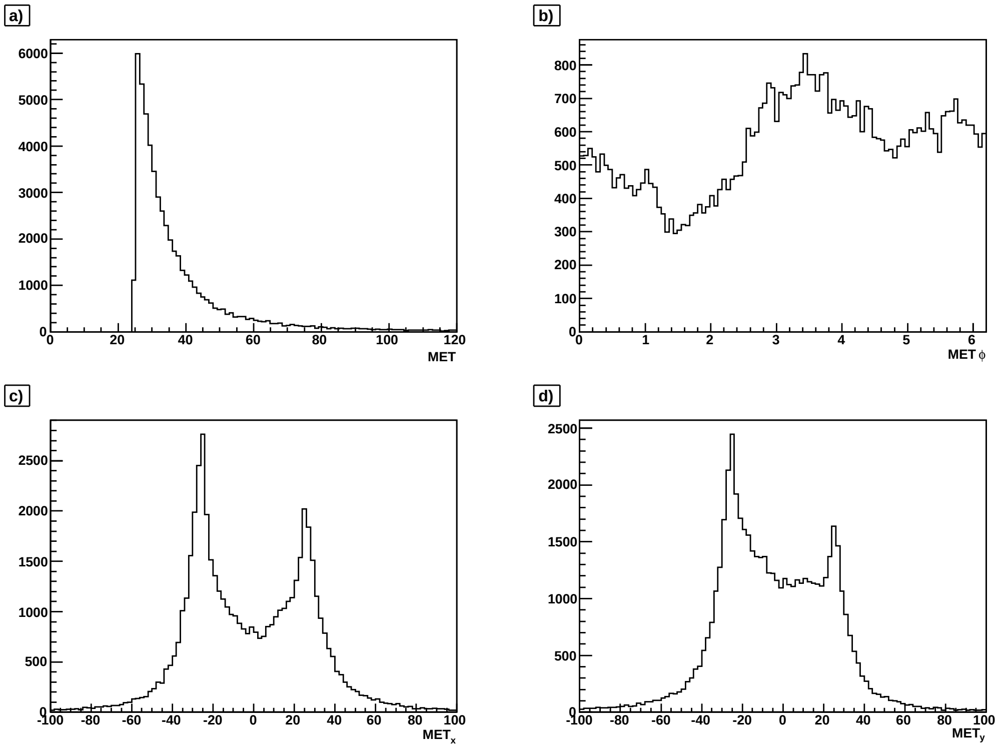

Figure 5.12: $\not\!\!E_T$ distributions after basic cuts and a two-jet requirement for the muon-triggered sample. Top left: $\not\!\!E_T$. Top right: ϕ distribution. Bottom left: x-component of the $\not\!\!E_T$ distribution. Bottom right: y-component of the $\not\!\!E_T$ distribution.

instrumental background events. Instrumental background events are defined as those events that lie in the parts of the distributions that are present in the data plots, but not the MC signal and MC background. An example of the elimination of noise events by cuts 10 and 12 is nicely shown in Figure 5.14, which is a scatter plot of $Asym(\not\!\!E_T.\not\!\!H_T)$ against $|trk\not\!\!E_T - trk\not\!\!E_T(dijet)|/trk\not\!\!E_T$ after all selection criteria have been applied except the two plotted. In the top plot (data), a diagonal trail of events can be seen reaching from the central, signal region down to low values of $Asym(\not\!\!E_T.\not\!\!H_T)$ $|trk\not\!\!E_T - trk\not\!\!E_T(dijet)|/trk\not\!\!E_T$. This trail of events is not seen in the middle (MC background) and bottom (MC signal) plots, so they are assumed to be due to instrumental background. Cut 15 ensures that the tracks from the jets contribute the majority of the $trk\not\!\!E_T$ as one would expect for real jets and that the $trk\not\!\!E_T$ does not result from an uneven track distribution from the underlying event

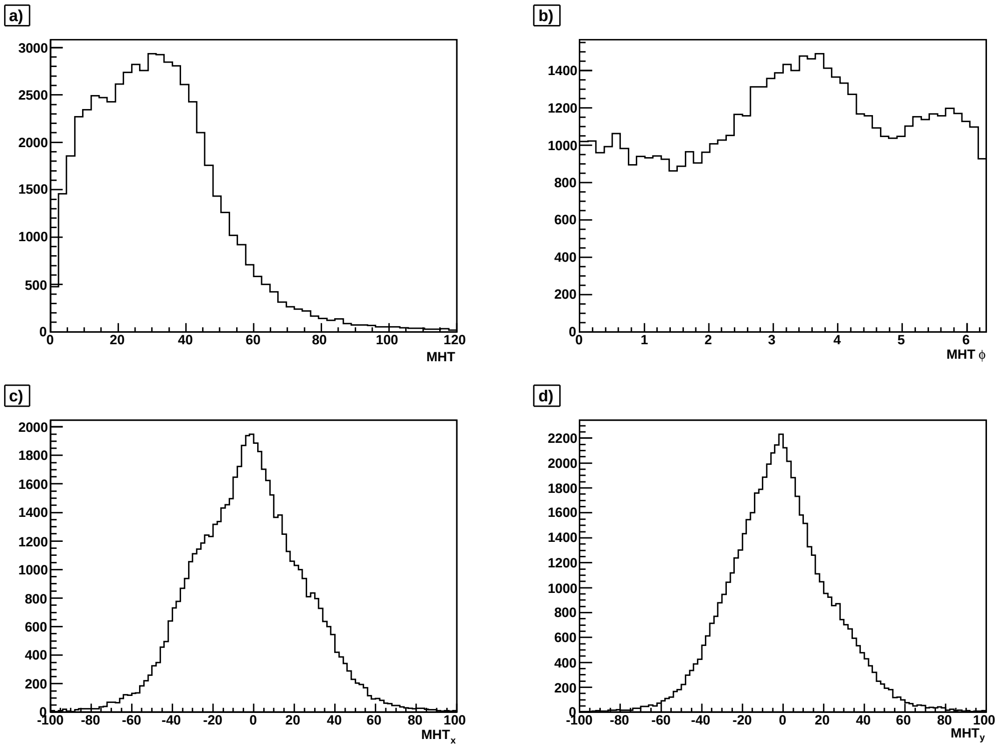

Figure 5.13: $\not\!\!H$ distributions after basic cuts and a two-jet requirement for the muon-triggered sample. Top left: $\not\!\!H$. Top right: ϕ distribution. Bottom left: x-component of the $\not\!\!H_T$ distribution. Bottom right: y-component of the $\not\!\!H_T$ distribution.

or from the track reconstruction itself.

Cuts 16 and 17 choose events in which there are two jets that originate from b-quarks and so b-tag the jets by assigning a probability that they indeed originated from b-quarks. The probability that a jet is a b-jet is broken down into two parts: the probability that a jet is taggable (*taggability*), and the probability that a taggable jet is efficiently tagged (*tagging efficiency*). The taggability is separately defined [97] from the tagging algorithm and requires that:

- The jet has at least two tracks.
- The tracks in the jet are required to have p_T >0.5GeV and at least 1 SMT hit in the SMT barrels or F disks
- At least one track in the jet is required to have p_T >1GeV (track seed)

- Tracks are required to have DCA<0.2cm and Z_{DCA} <0.4cm.

A priori, it is expected that taggability will be different between data and Monte Carlo. In MC, the taggability is higher than in data mainly due to a limited description of the tracking detectors resulting in a higher tracking efficiency, particularly within jets. So the MC taggability must be calibrated to that observed in the data and this process is described in Section 5.3.4.

5.3.3 Background Estimation

By applying the cuts outlined in the previous section, the instrumental background is reduced significantly. However, the absolute scale of this background, which is mainly QCD, is still unknown. It is difficult to model the scale of the QCD background accurately in Monte Carlo so the normalisation is estimated by selecting a region of parameter space (the sideband region) which is expected to be dominated by the QCD background. The parameter space chosen was $Asym(\not{E}_T, \not{H}_T)$ against $|trk\not{E}_T - trk\not{E}_T(dijet)|/trk\not{E}_T$ because the signal, physics and instrumental background events are visibly separate. The distributions for signal, MC physics backgrounds and data are shown in Figure 5.14. The scatter plots have been divided into three boxes, a central 'signal' box (cuts 10 and 12) and two sideband regions defined by $0.4 > (\not{E}_T + \not{H}_T)/dijet(trk\not{E}_T) < 1.0$ and $-0.1 < Asym(\not{E}_T, \not{H}_T) < 0.2$.

Examining Figure 5.14, the central region well defines the signal events, contains physics background events, and excludes the instrumental background events. The sidebands include and exclude the opposite, so they may be used to make a good estimate, by extrapolation, of the number of unwanted 'QCD' events in the signal region. The MC shape is calculated via a fit to MC events in the signal box whereas that of the instrumental background is calculated from a fit to data in the sideband regions. The absolute normalisation of the MC and the instrumental background is then fixed via the combined fit of the two to the data in the signal box, allowing only the absolute scale of the two backgrounds to float.

Figure 5.15 shows the fits to the physics background, sideband data and the

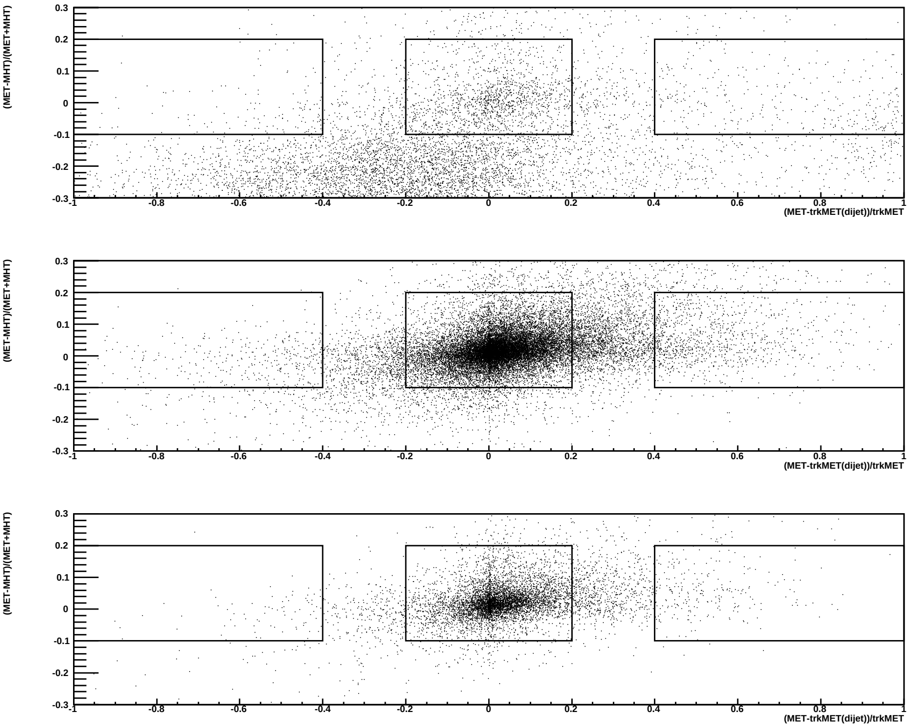

Figure 5.14: Scatter plot of $Asym(\not{E}_T, \not{H}_T)$ against $|trk\not{E}_T - trk\not{E}_T(dijet)|/trk\not{E}_T$. After all selection criteria except the two plotted. Top plot: data. Middle: signal MC. Bottom: background MC (un-normalized). The central boxes represent the signal region and the side boxes the 'sideband' regions.

combined fit to the signal region (left, middle and right) for no taggability requirements, one or more taggable jets and two taggable jets (respectively top, middle and bottom). The fit to the MC is a double Gaussian and to the sideband data it is an exponential. The only numbers left to float in the combined fit are the absolute normalization of the two components labelled 'p_7' for the sideband component and 'p_8' for the MC physics. As one can see, the normalization of the two components is 1.0 within errors (top right hand plot). However, the normalisation ranges from 0.94 with no taggability requirements to 0.80 when requiring both jets to pass the taggability requirements. As a consequence, the taggability in MC needs to be corrected to that seen in data (see Section 5.3.4 for more details). This is because taggability in MC is a lot higher than in data so subsequently, the MC component is overestimated as the taggability requirements are imposed (middle and bottom right hand plots). Table 5.4 gives the number of instrumental and physics background events with: (a) no taggability requirement, (b) a single taggability requirement and (c) a double taggability requirement. These were estimated using these fits to the data and MC. The number of physics background events with a double taggability requirement is used as a cross-check with the number of MC events remaining after all cuts in the MC simulation. After all cuts, including a double taggability requirement, these are 417±14 events in the MC simulation which is in agreement with the number derived from the fit of 442±11 events. The error on the number of events from the fits is estimated by varying the parameters of the fits by $\pm 1\sigma$ and noting the variation in the number of events.

	Instrumental Noise Events	Physics Background Events
No taggability requirement	593.60	693.12
At least one taggable jet	399.78	656.68
Two taggable jets	268.35	442.44

Table 5.4: Number of events obtained from fits to the QCD and non-QCD components in data for different taggability conditions.

5.3.4 Taggability Corrections

The taggability is dependent on the z-coordinate of the primary vertex (PV_Z), the jet transverse energy and the jet η. A two dimensional parameterisation in terms of E_T and η is derived by assuming that the dependence on PV_Z is factorisable. The taggability per jet is determined from data and parameterised as a function of jet E_T and η only:

$$P^{tagg}(E_T,\eta) = \frac{\#\, taggable\ jets\ in\ (E_T,\eta)\ bin}{\#\, jets\ in\ (E_T,\eta)\ bin}. \tag{5.1}$$

The functional form below is fitted to this parametrisation and calculated after basic selection cuts have been applied:

$$p_0 \times \tanh(p_1 + p_2 p_T + p_3 + p_4\eta + p_4\eta^2) \tag{5.2}$$

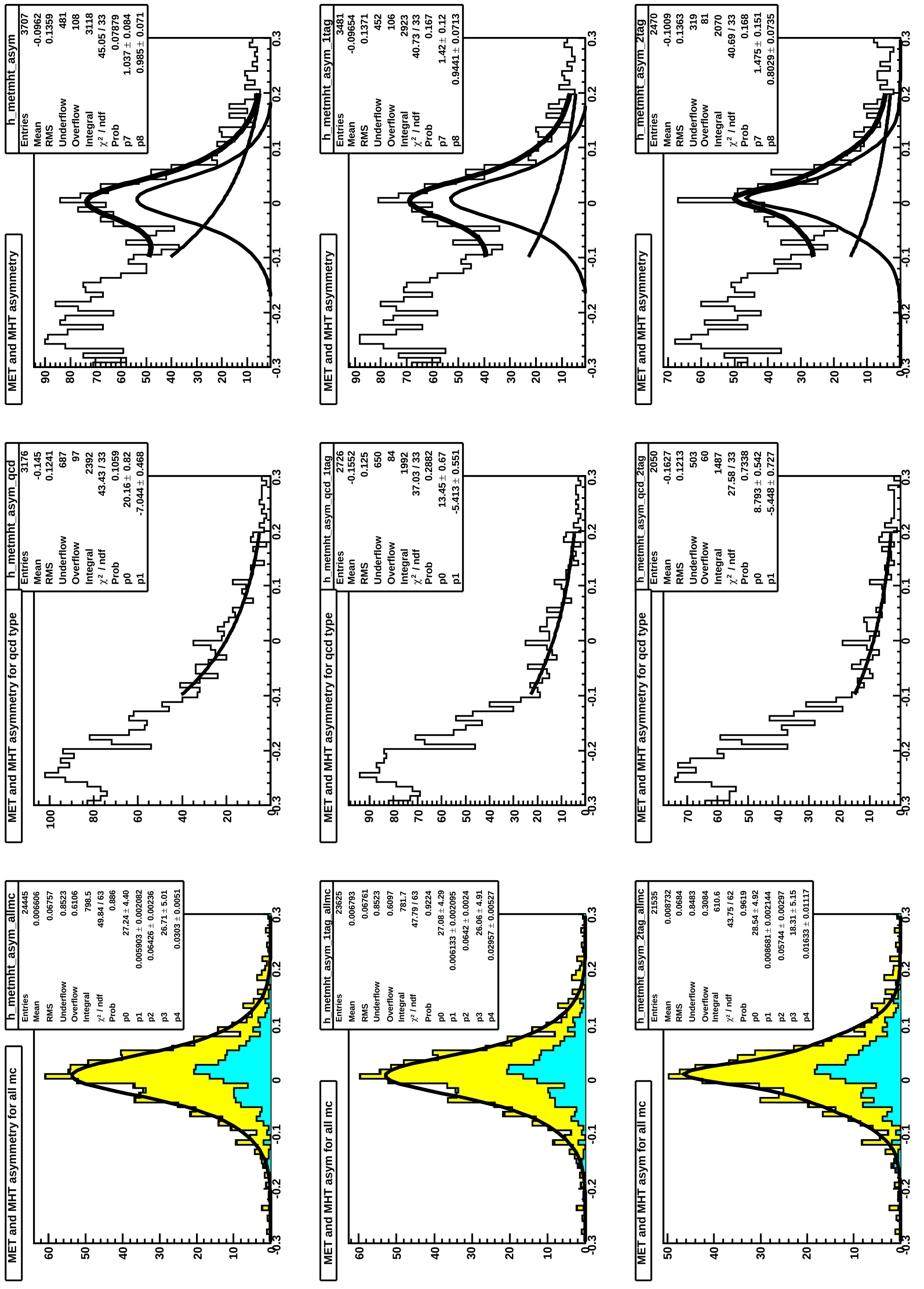

Figure 5.15: Fits for MC, sideband and signal region (left, centre and right), with no taggability requirements, at least one taggable jet and two taggable jets (top, centre, bottom). The lighter, yellow-shaded region represents the contribution to the physics background from Wj/Wjj/Wbb events. The darker, blue-shaded region represents the contribution from Zj/Zjj/Zbb events.

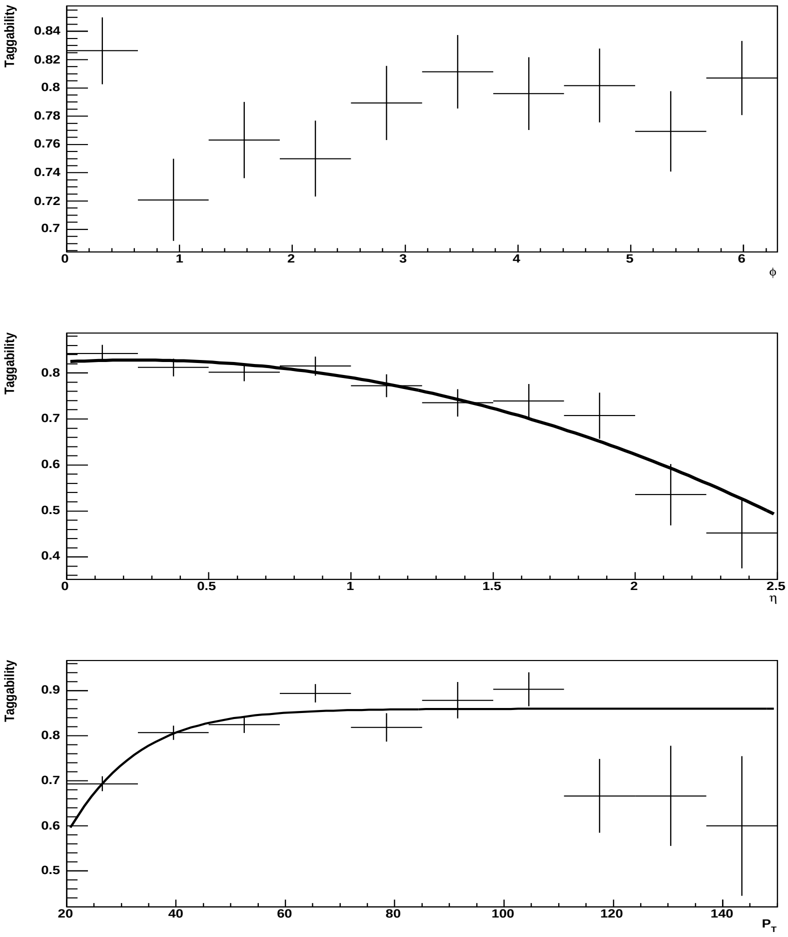

Figure 5.16: Jet taggability in data as a function of ϕ (top), η (middle) and p_T (bottom).

This parametrisation is then used to correct the taggability of the jets in the MC. Figure 5.16 shows the taggability efficiency in data parameterised in terms of η and p_T with a one dimensional fit shown. Also shown is the dependency on ϕ which, within errors, is flat (as expected). Figure 5.17 shows the two-dimensional binning and the above 2-D parametrisation along with the fit results. The taggability distributions are similar to those seen in [90], although the taggability with respect to p_T shown here plateaus at a lower value.

However, it is not enough to simply re-scale the MC taggability by the taggability in data, as the instrumental and physics backgrounds have different taggabilities within the signal region. From the numbers in Table 5.4, the taggability efficiency

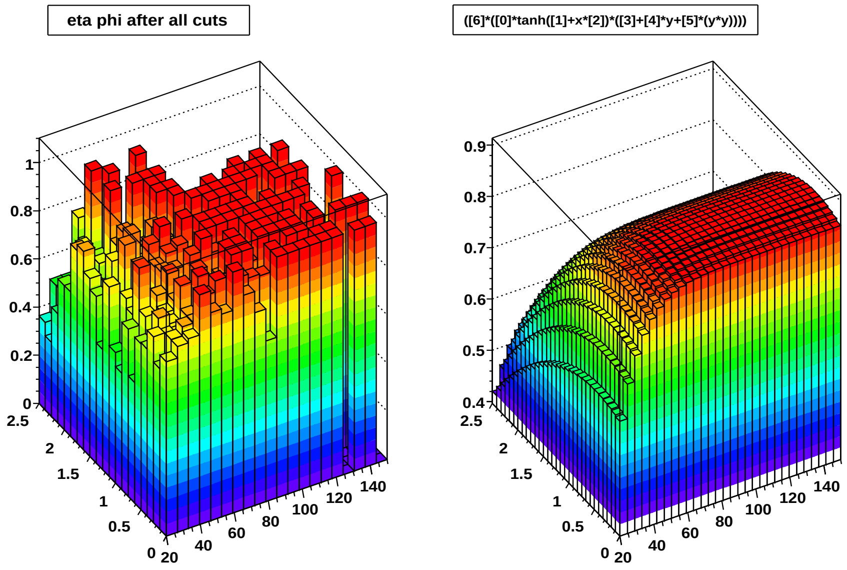

Figure 5.17: Jet data taggability efficiency parameterised in η–p_T

was calculated separately for QCD and non-QCD events using the following formula:

$$\epsilon = \frac{\epsilon_1^{event} + \epsilon_2^{event}}{2}, \tag{5.3}$$

where ϵ_1^{event} and ϵ_2^{event} are respectively the event efficiencies for at least one taggable jet and for two taggable jets. This gives a taggability of 54.48% for QCD and of 79.63% for non-QCD. This has to be compared to 78.33% for the overall efficiency in the signal region. Hence a scale factor of 1.016 is applied to the 2-D taggability parametrisation. Furthermore, τ jets have a further 0.56 scale factor applied, based upon MC efficiency calculations [90].

After all these corrections, the fits to the MC, sideband and signal region are shown in Figure 5.18 for events with two taggable jets. From the fits it can be seen that the MC normalisation agrees with the data within errors.

Kinematic Distribution Issues after Taggability

Figures 5.19-5.21 show the basic distributions after taggability requirements but before b-tagging. From Figure 5.19 it can be seen that the asymmetries in the jet ϕ distribution have been eliminated and furthermore, that the difference between the leading and next-to-leading jet η has gone. Overall, the agreement is reasonable.

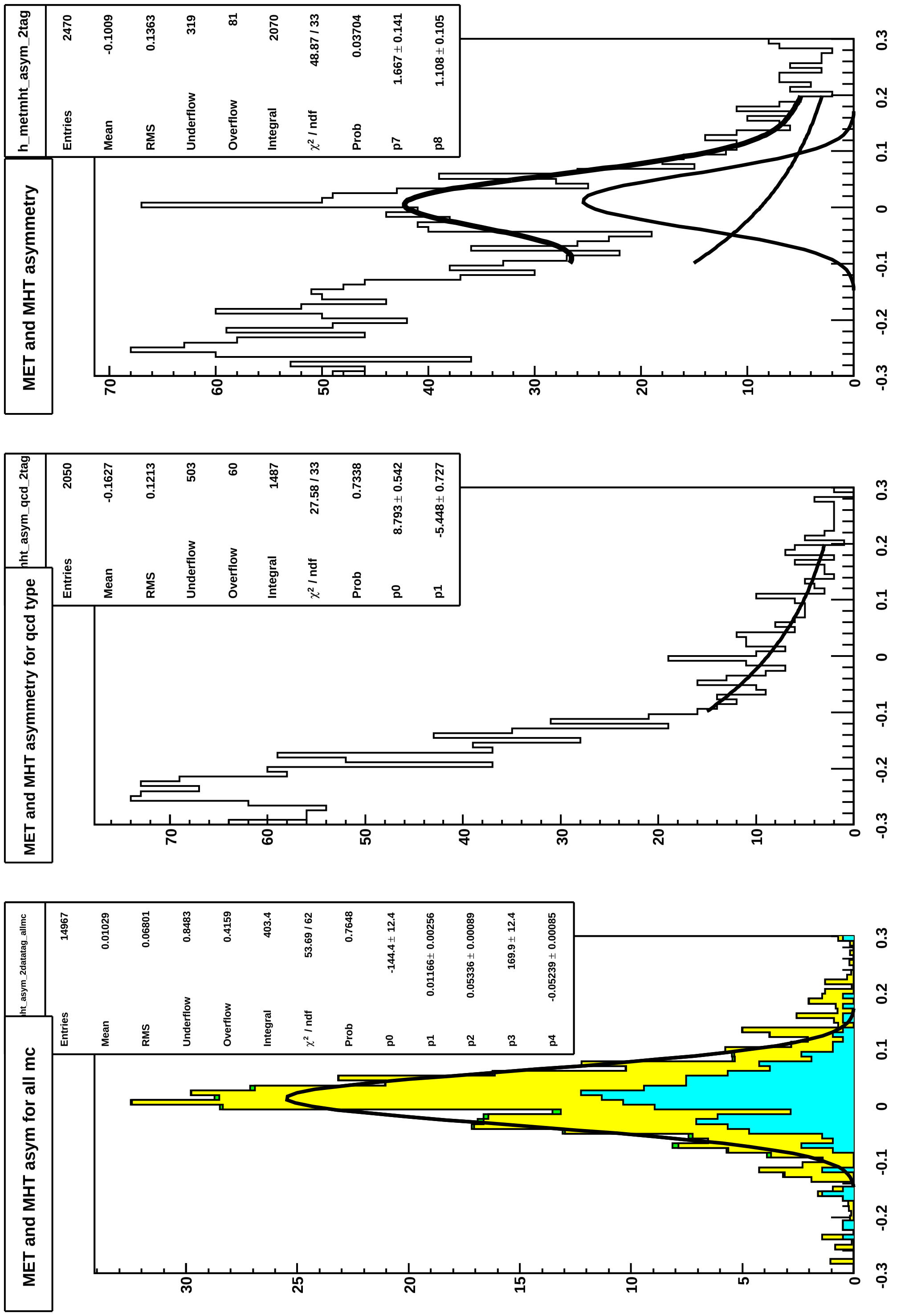

Figure 5.18: Fits for MC, sideband and signal region (left,centre and right) for two taggable jets after taggability corrections.

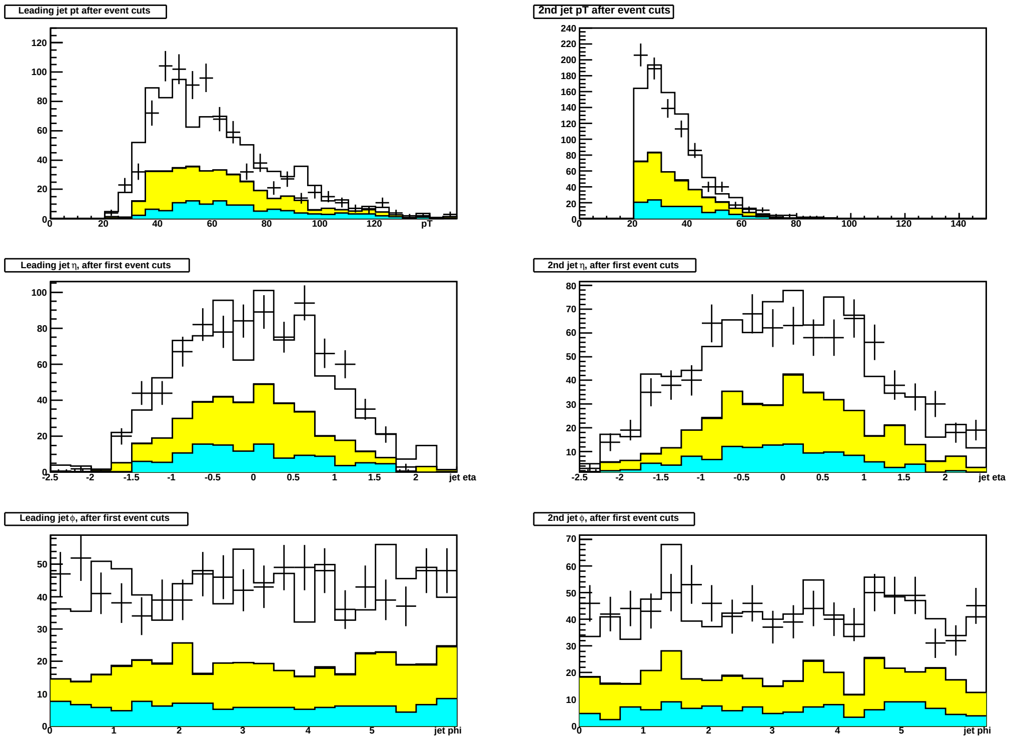

Figure 5.19: Basic jet distributions for leading (left) and next-to-leading jet (right). The lighter, yellow-shaded region represents the contribution to the physics background from Wj/Wjj/Wbb events. The darker, blue-shaded region represents the contribution from Zj/Zjj/Zbb events.

The $\not{E}_T$ distributions seen in Figure 5.20 also show a reasonable agreement. The $\not{H}_T$, shown in Figure 5.21, is seemingly modelled better. In the same figure, the number of jets is clearly not modelled well by this approach with significant discrepancies in all bins. This is most probably a problem in the modelling of the trigger using d0trigsim. There are known discrepancies in the d0trigsim description of the L1 calorimeter trigger between online and offline and there is also an incorrect noise simulation. So the L1 trigger term, which is solely dependent on tower energies, is generally inaccurate.

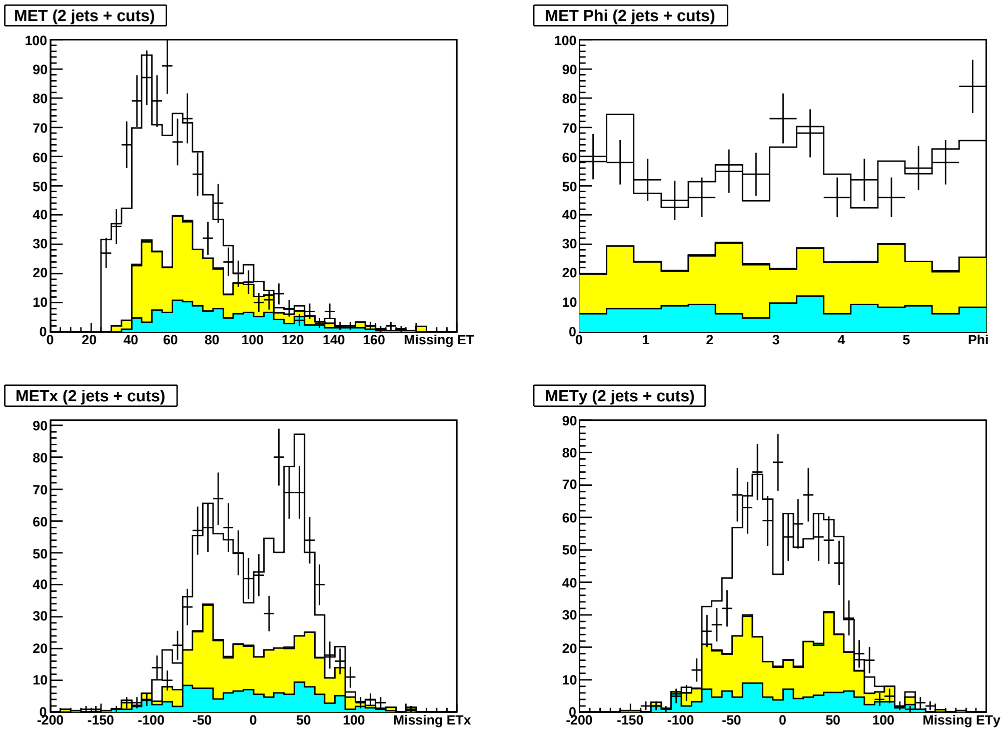

Figure 5.20: Missing energy distributions. Missing E_T in units of GeV. The lighter, yellow-shaded region represents the contribution to the physics background from Wj/Wjj/Wbb events. The darker, blue-shaded region represents the contribution from Zj/Zjj/Zbb events.

5.4 Monte Carlo Optimisation and b-tagging

In the previous v12 analysis, the selection criteria were placed by eye after comparing data and MC distributions, and included placing a window cut on the dijet mass in the event of 80GeV< M_{dijet} <130GeV. To improve the sensitivity of this analysis and to re-optimise the selection criteria now that a different trigger simulation was applied, two key multivariate techniques were used:

- A neural net based b-tagger (NN tagger), more efficient than the b-tagger used in [90], was applied to improve the selection efficiency of $ZH \rightarrow \nu\bar{\nu}b\bar{b}$ events, and to give better discrimination of non-b quark backgrounds
- Several key selection cuts were optimised for the MC analysis using the MI-

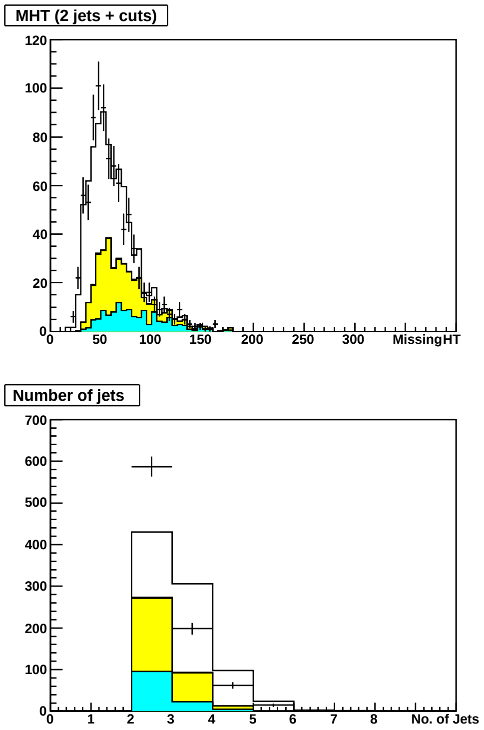

Figure 5.21: Distributions for missing H_T, scalar H_T, jet multiplicity and di-jet invariant mass. Units of GeV. The lighter, yellow-shaded region represents the contribution to the physics background from Wj/Wjj/Wbb events. The darker, blue-shaded region represents the contribution from Zj/Zjj/Zbb events.

NUIT optimisation software in ROOT. These cuts included some of the basic selection cuts described earlier, the b-tagging method used and the mass window applied.

5.4.1 B-tagging

Effective b-tagging is essential to this analysis both to enhance the signal and to reduce unwanted backgrounds not containing b-jets. The current, most effective method to tag b-jets is using the DØ NN b-tagger. A description of its development may be found in [10] and the certification results are detailed in [98]. The NN b-tagger was applied to the Monte Carlo samples to see if improvements could be made to the sensitivity, and the expected limit.

Other b-taggers Other b-taggers available are the jet lifetime impact parameter tagger (JLIP)[99], the secondary vertex tagger (SVT)[100] and the counting signed impact parameter (CSIP) [101] tagger; JLIP is the most effective of the three. All three are dependent on the long decay path of the B-hadron due to its long lifetime. The decay of a long-lived hadron produces several charged particles emanating from a secondary vertex, displaced from the primary $p\overline{p}$ interaction point.

The JLIP tagger uses the impact parameter information of the tracks seen in the SMT layers to calculate a probability. The impact parameters of all tracks associated to a jet can be combined into a single variable called the *jet lifetime probability* which is the probability that all tracks in a jet originate from the primary interaction point. Light quark jets have a flat probability distribution between 0 and 1, whereas the probability distribution for b-jets peaks at a low value so they are selected by appropriately-placed cuts.

The CSIP b-tagger also relies on the fact that tracks of charged decay products of long-lived B-hadrons have non-zero impact parameter with respect to the primary vertex. A sign and significance can be assigned to the impact parameter, and using these, a jet is tagged if two, or more, tracks associated with this jet have signed impact parameter significance greater than 3, or three or more tracks have signed impact parameter significance greater than 2.

The SVT identifies B-hadrons based on the properties of the secondary vertex and the decay length of the B-hadron. Using Pythia Monte Carlo, the 'average' properties of a B-hadron secondary vertex are described in terms of the decay length, the average number of charged particles emanating from the secondary vertex, the jet cone size containing 99% of the jet energy and the impact parameter significance[10].

The Neural Net Tagger The NN b-tagger shows an improvement of between 15% (loosest operating point) and 40% [98] in signal efficiency over the JLIP tagger, and fake rates reduced by at least one third for a fixed signal efficiency. The NN tagger is constructed using the ROOT class TMultiLayerPerceptron and takes as

---

[10] Impact parameter significance = Distance of closest approach/σ(Distance of closest approach)

input variables a combination of the best quantities from the three other b-taggers, such as the JLIP b-tag probability. It was then trained on several relevant MC samples including $t\bar{t}$, $Z \to b\bar{b}$, $c\bar{c}$, $q\bar{q}$ and QCD events. All training samples were processed to apply the Jet Energy Scale corrections and $\not\!\!E_T$ smearing. While the NN b-tagger outputs a continuous "probability" that the jet is a b-jet, tag rate functions only exist for discrete operating points, similar to the JLIP loose, medium and tight operating points. Each operating point has a tag rate function, parameterised as a function of jet η and p_T, for mapping MC b-tagging efficiencies to data b-tagging efficiencies. Table 5.5 details the operating points, efficiencies, approximate fake rates, and systematic uncertainties of the NN tagger. These operating points are currently the only cuts that may be applied to events in the form of lower bounds on the NN output.

Operating Point	L4	L3	L2	Loose	Medium	Tight
NN probability cut	> 0.2	> 0.25	> 0.325	> 0.5	> 0.625	> 0.7
Efficiency	71.4%	68.7%	65.3%	59.4%	54.0%	48.6%
Approximate Fake Rate	4.0%	3.0%	2.0%	1.0%(1.4%)	0.5%(0.7%)	0.325%(0.4%)
Systematic Uncertainty	1.9%	1.5%	1.2%	1.1%	1.2%	1.0%

Table 5.5: NN b-tagger operating points, and corresponding efficiencies, approximate fake rates and systematic uncertainties [10]. The JLIP equivalent fake rates are quoted where available in brackets next to the NN b-tagger quantity.

The NN b-tagging was applied firstly to the Monte Carlo samples, after requiring all other cuts and using the standard taggability, in place of the JLIP b-tagging used in the earlier analysis of this channel (1^{st} and 2^{nd} columns in Table 5.6). The use of the NN tagger in place of the JLIP tagger with no adjustments to cuts gives a 30% improvement in sensitivity. It was then incorporated into the optimisation of the basic event cuts using the MINUIT package (3^{rd} column in Table). To ensure that the MC tag rate is the same as the rate in data, the data tag rate functions were used directly on the MC. The optimisation of the cuts using MINUIT gives a further 15% improvement in sensitivity.

The $\not\!\!E_T$ cut (Cut 4 and Cut 5) removes many of the multijet events (see cutflow tables in Appendix B). Unfortunately, the $\not{E}_T$ requirement also picks up events where a $W \rightarrow l\nu$ and this will include backgrounds from WZ and $Wb\bar{b}$. This also means that WH events will be added to the effective signal. Further cuts include isolated lepton cuts which reduce the backgrounds involving W decay and Z decays to muons, but many of these events will remain due to muon detection inefficiencies. An undetected muon will also add to the apparent $\not{E}_T$ of the event. This means that WH events will appear in the measured signal events and so these were included in the calculation of the sensitivity.

Table 5.8 shows the estimated numbers of b-jets passing a double JLIP medium tag and a double loose NN tag. These are derived from the fits to the signal region and background described earlier in Section 5.3.3.

	Original Cuts [90]	Original Cuts [90]	Optimised Cuts
b-tagging	JLIP double medium	NN double loose	NN double loose
ZH/WH	0.022 ± 0.001	0.040 ± 0.001	0.040 ± 0.001
Zjj/Zj/Zbb	0.49	0.83	0.76
WjWjjWbb	1.32	2.36	2.58
tt/tb/tqb	0.105	0.16	0.40
WZ/ZZ	0.04	0.07	0.07
Instrumental Background	1.2	0.9	0.0
Total Background Events	3.16 ± 0.32	4.33 ± 0.24	3.81 ± 0.31
Sensitivity	0.013 ± 0.001	0.017 ± 0.001	0.019 ± 0.001

Table 5.6: Summary of number of events after selection cuts, M_H =115GeV, no mass window, for comparison of the effect of replacing the JLIP tagger with the NN tagger.

5.4.2 MINUIT Optimisation of Certain Variables

The v12 analysis of this channel included basic selection cuts that were decided by comparison of the plots of MC signal and background events of the relevant variables. To improve the sensitivity of this analysis, the ROOT-embedded MINUIT [102] optimisation package was used, which is able to globally maximise a function that is dependent on the selection criteria. In this instance the significance ($N_{Sig}/\sqrt{N_{Bkgd}}$) was used. The original cuts were used as the starting point for the MINUIT optimisation on the MC backgrounds and $M_H = 115$GeV MC signal sample. MINUIT optimised the cuts on the event samples listed in Table 5.3. From examination of the cutflow table and the distributions themselves, it was decided that the values of the $\not{E}_T$ cut, jet p_T cuts, H_T cut, the b-tagging cuts and the mass window cuts have the most significant effect on the sensitivity. These variables are listed with their original values in Table 5.7. The optimum position of the mass window was found by MINUIT separately and after optimisation of the other variables. The optimum selection criteria of the other variables in Table 5.7 should not depend on the position of the mass window, nor its width. The min $\triangle\phi$ cut was also examined as there appeared to be a difference in distributions between background and signal upon inspection of the plots, but MINUIT was not able to discriminate on this, and so no change was made to this cut.

Variable	Original Cut	Optimised Cut
$\not{E}_T$	>25GeV	>20GeV
Leading jet and next to leading jet p_T	>25GeV	>20GeV
$\not{H}_T$	<200GeV	<210GeV
b-tagging (Leading jet)	JLIP medium	NN loose
b-tagging (Next to leading jet)	JLIP medium	NN Loose
Mass Window	80GeV - 130GeV	no window applied

Table 5.7: Variables optimised using MINUIT for $M_H = 115$GeV.

5.4.3 Results of Optimisation of Event Selection

The optimised selection cuts are given, with the original cuts, in Table 5.7. Table 5.8 shows the estimated number of instrumental and physics background events remaining after a JLIP double medium tag or a double loose NN tag. The number of instrumental background events with a double b-tag requirement is used directly in the limit calculation. The number of physics background events is used as a cross-check with the numbers remaining after selection cuts.

	Double Taggable	JLIP medium double tag	NN loose double tag
Physics Background	437.9	2.05	3.05
Instrumental Background	268	1.2	0

Table 5.8: Estimation of the number of instrumental background events after double medium JLIP tagging and double loose NN tagging.

5.4.4 Summary of Event Selection

Tables B.1 to B.4 in Appendix B give the selection efficiencies for data, MC signal and MC backgrounds in percent after optimised cuts, and NN b-tagging. These detailed tables are summarised later in Table 5.10.

5.5 Errors

The systematic errors for this analysis follow those from the v12 analysis [90] and are summarized in Table 5.9. It is assumed that the sources of these errors are uncorrelated and so they have been combined in quadrature. These errors arise from the errors in the fits used to derive the corrections that have been applied to the MC samples to correct for the MC/data differences.

These errors were estimated by varying each source of error by $\pm 1\sigma$ from the central value, and noting how the total background and signal acceptances are changed. The errors arising from jet corrections (errors 1 to 3 below) are taken directly from [90] and are assumed to be applicable to this analysis as they apply to the same samples, the remainder have been calculated as they are more affected by the differences between the v12 and v13 analyses.

1. **Jet Identification Efficiency** The jet-id correction factor was varied by $\pm 1\sigma$ or 5%, the error on the reconstruction efficiency[76].

2. **Jet Energy Scale Factor** The correction factor was varied by $\pm 1\sigma$ for each jet. The jet energy correction factor is based on light jets so the difference

Error Source	Signal Error (%)	Background Error (%)
Jet ID	7	6
Jet Energy Scale	7	8
Jet Smearing	3	3
Taggability	7	7
NN b-tagging	4	21
NN b-tagging (instrumental)	-	2
Background Cross-sections	-	18
Instrumental background expectation	-	2
Luminosity	6.5	6.5
Total	13	30

Table 5.9: Systematic uncertainties due to corrections, taggability fits, b-tagging and background estimation for all background samples and for $M_H = 115$GeV, and a double loose NN b-tag.

between the response for light jets and b-jets must also be accounted for. It was estimated in [90] using the Z mass calculated using Z→ qq and Z→ $b\bar{b}$ MC samples. The difference in the mean value of the Z mass distribution of 7% is included in the systematic error. This error is applied to both signal and background samples with b-jets.

3. **Jet p_T Resolution Smearing** The MC resolution was changed by $+1\sigma$ and the data by -1σ in the first instance to give a minimum smearing and the analysis repeated. In the second instance, to obtain the maximum smearing, the MC resolution was changed by -1σ and the data by $+1\sigma$, and the analysis repeated again. If the data resolution was better than the MC resolution, no smearing was applied [90], [103].

4. **Taggability** The correction factor of 1.016 ± 0.036 derived in Section 5.3.4 was varied by $\pm 1\sigma$, and the mean of the variation in each of the number of background and signal passing was taken.

5. **NN b-tagging efficiency** The tag rate function was varied by $\pm 1\sigma$ for both the signal and the background. The systematic uncertainty in the instrumental

and physics backgrounds was taken from [98] as described in Section 5.4 and weighted by the assumed ratios of b, c and light-quark jets.

6. **Background Cross-sections** From comparisons of LO and NLO cross-sections, this was estimated in the v12 analysis [90] to be a conservative 20%, leading to an error of 18% in the total background expectation in this analysis. This is based on information from [8].

7. **Instrumental Background Expectation** The uncertainty in the instrumental background expectation was estimated from the error of the fit to the backgrounds as described in Section 5.3.2. The error on the fit leads to estimated uncertainties of 268±9 QCD events, and 442±11 physics background events translating to an error of 2% in the total background.

The statistical errors for the MC signal and background are assumed to be Poisson-distributed. They are given next to the quantities in the relevant tables.

5.6 Limit on $\sigma(p\bar{p} \to ZH) \times Br(H \to b\bar{b})$

Upper limits were set for $\sigma(p\bar{p} \to ZH) \times Br(H \to b\bar{b})$, for four Higgs boson masses of 105GeV, 115GeV, 125GeV and 135GeV and are given in Table 5.10. This table details the number of MC signal events, the number of MC background events and the number of data events passing all cuts, and the sensitivity of this analysis for each mass point. Since the background samples used were the same, irrespective of the Higgs samples used, the number of events for each background does not vary with the Higgs mass. The table gives the signal acceptance after scaling by the $Z \to \nu\bar{\nu}$ branching ratio of 20% [8]. The 95% C.L. limits are calculated using a Bayesian method [104] [105] and are found to be between 19.3pb and 57.1pb. The expected cross-section limits in the no-signal hypothesis were calculated assuming that $N_{sig} \ll N_{bkg}$, and that $N_{data} = N_{bkg}$ and were found to be between 13.8pb and 40.3pb. The limits calculated include both the statistical and systematic errors as calculated and discussed in section 5.5. Figure 5.23 shows one of the five remaining

ZH candidates after all selection criteria have been passed. The remaining four may be found in Appendix C.

Higgs Mass	105 GeV	115 GeV	125 GeV	135 GeV
ZH	0.0057 ± 0.0013	0.0245 ± 0.0038	0.0193 ± 0.0031	0.0048 ± 0.0012
$ZH(H \rightarrow b\bar{b})$ acceptance	0.0061± 0.0016	0.0066 ± 0.0013	0.0082 ± 0.0009	0.0037 ± 0.0004
WH	0.006	0.012	0.007	0.004
Zjj/Zj/Zbb	0.76			
Wjj/Wj/Wbb	2.58			
tt/tb/tqb	0.40			
WZ/ZZ	0.07			
Instrumental Background	0.0			
Observed Data Events	5.00			
Total Background Events	3.81 ± 1.19			
Sensitivity ($N_{sig}/\sqrt{N_{bkg}}$)	0.006	0.019	0.014	0.005
Limit of $\sigma(p\bar{p} \rightarrow ZH) \times Br(H \rightarrow b\bar{b})$	32.8 pb	21.8 pb	19.3 pb	57.1 pb
Expected Limit of $\sigma(p\bar{p} \rightarrow ZH) \times Br(H \rightarrow b\bar{b})$	23.2 pb	15.7 pb	13.8 pb	40.3 pb

Table 5.10: Number of expected and observed events, channel and signal acceptance (includes $Z \rightarrow \nu\bar{\nu}$ branching ratio), sensitivity, observed and expected cross-section limit for three mass points $M_H = 105$GeV, 115GeV, 125GeV, 135GeV.

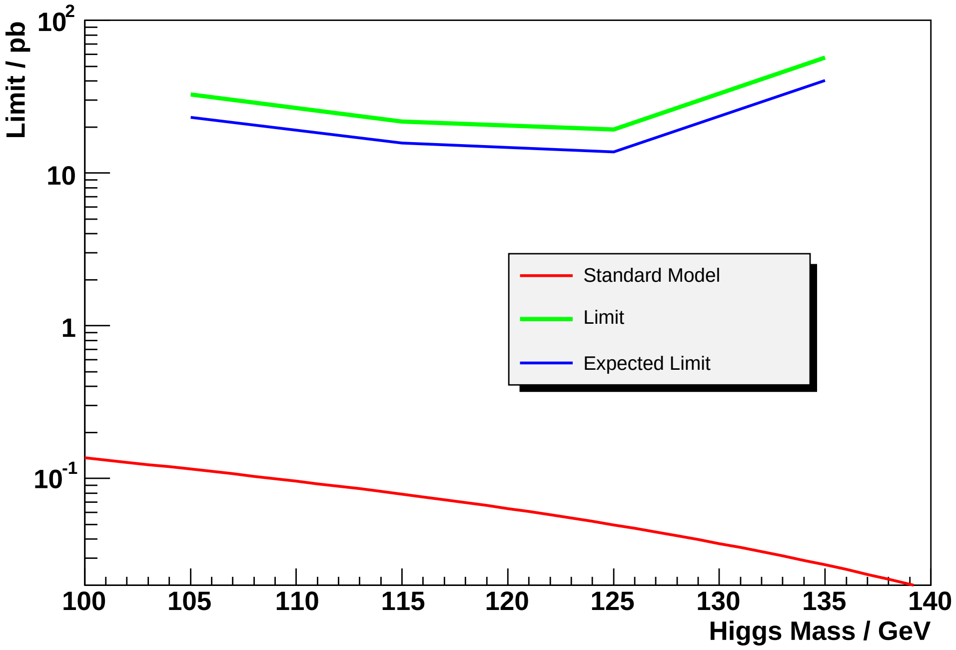

Figure 5.22: Standard Model, observed and expected limits (pb) against M_H (GeV).

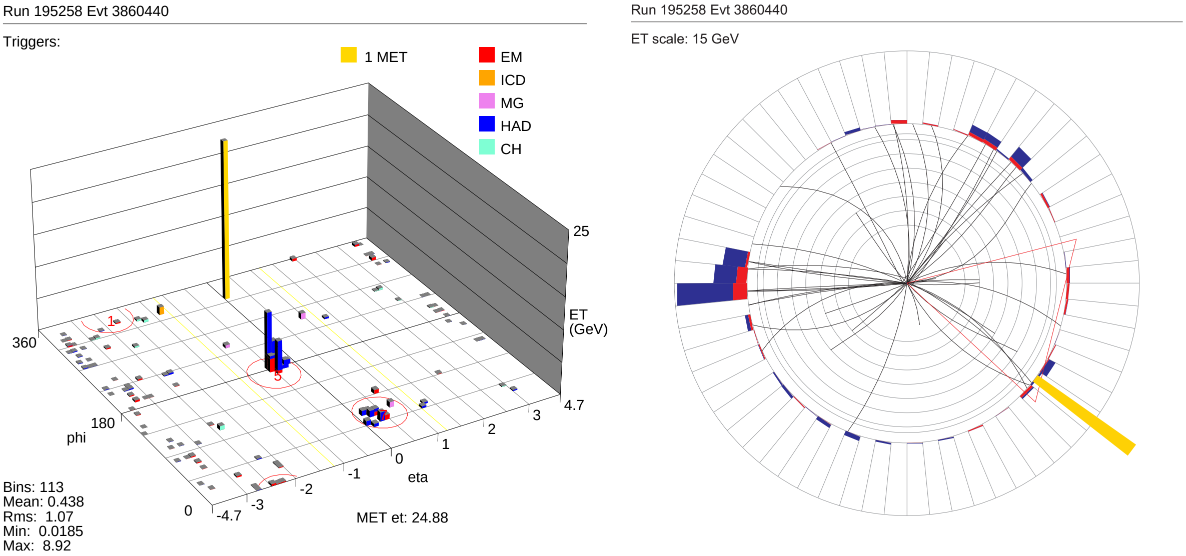

Figure 5.23: Data event display of a ZH event candidate that passes all selection cuts. Run number = 195258, event number = 3860440. On the left is shown the calorimeter transverse energy in the $\eta - \phi$ plane. On the right is the calorimeter and tracking view, as a projection in the $x - y$ plane at $z = 0$. Missing E_T is shown in orange.

5.7 Conclusions

A search for $ZH \rightarrow \nu\bar{\nu}b\bar{b}$ events on $55.25pb^{-1}$ of data, collected with the v13 trigger list, was carried out. The analysis follows that developed for the v12 trigger list data sample ($261pb^{-1}$) in [90]. Improvements in the offline analysis include a Monte Carlo optimisation of the analysis selection criteria and the first use at DØ of the neural net (NN) b-tagger tool. In MC, four different light Higgs masses (105GeV, 115GeV, 125GeV and 135GeV) and the main backgrounds listed in Tables 5.2 and 5.3 were simulated. The observed 95% C.L. limits are calculated at between 19.3pb and 57.1pb; the expected limit is set between 13.8pb and 40.3pb. While these limits are approximately 2 to 4 times greater than those set in the v12 analysis, they are comparable with them and with those set in other analyses, given the relatively small integrated luminosity. The limits set would scale to approximately 10pb for M_H = 115GeV for a 261pb^{-1} data set. Other recent expected limit results from DØ include 6.6pb for WH production ($174pb^{-1}$) [106] and a limit of 9.7pb was set for ZH production in the $\mu\bar{\mu}b\bar{b}$ channel[107] (320pb^{-1}). Comparable results from CDF include 95% C.L. upper limits of 17.8pb to 22.8pb (m$_H$=110GeV to 130 GeV) on the SM Higgs production cross-section for ZH/WH production, for the H→bb, and Z→ $\nu\bar{\nu}$ or W→ $l\nu$ decay channels [108]. Also, an upper limit on the WH production cross section times branching ratio was set at 3.9pb to 1.3pb. This search used data corresponding to an integrated luminosity of 955pb^{-1} and a neural network b-tagging selection to select double-tagged W+2jet events [109].

This v13 analysis and the v12 analysis are comparable but the improvements in sensitivity through the MC optimisation and the use of the neural net b-tagger in this analysis are compensated for by the use of single b-tagged events in addition to double b-tagged events in the v12 analysis. The use of the neural net b-tagger has improved the sensitivity of this study, over that of the v12 analysis, by approximately 30% when used instead of the JLIP b-tagger. The MC optimisation of the b-tagging selection criteria and certain basic selection criteria improves the sensitivity by a further 15%. The main backgrounds are from the Wjj samples, with the greatest contributions coming from the events where the W decays to $\mu\nu$. Further work includes investigating the poor efficiency of the isolated lepton cut further as this only has an efficiency of approximately 30%, and including the single b-tagged events in the MC optimisation.

This first look at available v13 data highlights many issues which will need to be taken into account in the p17 version of the analysis, although data and Monte Carlo are in reasonable agreement. It is anticipated that the new electromagnetic and hadronic calorimeter calibration in p17 will have a significant effect on the $\not\!\!E_T$ distributions and some of these conclusions will have to be revised. From the jet multiplicity plot in Figure 5.21, it can be seen that there is either a large trigger bias in the v13 triggers or that there is some problem with the trigger simulation. The small integrated luminosity of this sample means that the limit set in this analysis adds little to a combined v12/v13 analysis. So given the imminent availability of p17 data it was deemed worthwhile to spend more time understanding similar factors in the p17 data, rather than investing further effort understanding the remaining issues for the p14 v13 data. However as the p14 v12 data, which uses a different approach to the trigger modelling in Monte Carlo, matches better, it is reasonable to assume that the discrepancies seen can be traced to the use of d0trigsim to model the effect of the v13 triggers. The approach taken in this analysis underlies the p17 analysis and is therefore good preparation in advance of using a larger dataset, and has demonstrated the potential of the MC optimisation and the neural net b-tagger for increasing the sensitivity of the $ZH \rightarrow \nu\bar{\nu}b\bar{b}$ channel. DØ is moving towards using more advanced multivariate analysis techniques, such as neural nets, to make the most of the data by powerfully discriminating against the background processes. The SUSY Higgs workshop [6] group noted the potential for a neural net analysis of this channel and this analysis, when carried out on p17 data, will form a good standard analysis with which to assess such a technique. There are further improvements in the b-tagging from L0 in the silicon tracker. The new hadronic calorimeter calibration and TrackCal should improve dijet mass resolution by about 20%.

Chapter 6

Conclusions

One of the major goals for DØ and the Tevatron is the observation or the exclusion of the Higgs boson. Although the Standard Model, which is based on a SU(3)$\otimes$SU(2)$_L\otimes$U(1)$_Y$ symmetry, currently well-describes the strong, electromagnetic and weak forces and the observed particles, it does not explain the particle masses that we observe. The Higgs mechanism breaks the symmetry, thus generating the particle masses and the Higgs boson, but it does not predict the mass values themselves. Combined results from indirect and direct searches compellingly indicate that the Higgs has a mass between 114.4GeV and 200GeV. Since the Higgs is massive, it is only high-energy facilities like the Tevatron, or LHC when it comes online in 2007, that will be able to discover the Higgs if it exists in this form.

Both the Tevatron and the DØ experiment are running well and exceeding design expectations. Since DØ came online in 1992, it has undergone extensive upgrades to improve the detector, compensate for aging parts and to make the most of new physics opportunities that have arisen with the Tevatron upgrades, most noticeable the centre of mass energy increase from 1.8TeV to 1.96TeV. The running of the detector is split into two main runs, Run I and Run II, which is further subdivided into Run IIa, the focus of this thesis, and Run IIb. The total Run IIa integrated luminosity, from 19th April 2002 to 23 May 2006, as seen by DØ was 1.18fb^{-1} , operating for much of Run IIa at over 85% efficiency.

The studies described in this thesis represent a significant contribution to the DØ experiment. In $p\overline{p}$ interactions at 1.96TeV, jet production is the dominant process and so an accurate understanding of this process and the jet energy scale is essential. Currently, the jet energy scale represents the biggest source of systematic uncertainty in measurements such as the top mass. At DØ , the jet energy scale, the energy calibration for jets in the calorimeter, is derived from (γ + jets) data events using the missing E_T projection fraction method which exploits the conservation of transverse momentum in the $p\overline{p}$ collisions. As part of the certification of versions 4.2 and 5.1 of the (γ + jets) official jet energy response, the response was calculated for data and MC for p14 (Z + jets) events, using the missing E_T projection fraction method. Closure tests on (Z + jets) events, were also performed, contributing to the release of the jet energy scale. These provided a valid cross-check of the response before it was implemented as part of the jet energy scale at DØ. The (Z + jets) and (γ + jets) response agreed well within errors but despite using all the then available data and MC, the lack of statistics still meant that (Z + jets) events could not be used to derive the full jet energy correction. However, approximately $1fb^{-1}$ data is now available for use with a new collaboration-wide analysis format; it will then be possible to derive a response for (Z + jets) events with a precision comparable to the (γ + jets) response.

The b-quark has its own physics programme at DØ as its mass is low enough that that b-quarks are produced abundantly but high enough that its lifetime is long enough for it to be easily differentiated from other jets originating from the lighter quarks. Furthermore, b-quarks are present in the final states of many decays, most significantly in the decay of Higgs, and specifically in the $p\overline{p} \rightarrow ZH \rightarrow \nu\bar{\nu}b\bar{b}$ channel, studied in this thesis. The identification and jet energy scale correction of b-jets is thus important to the physics programmes at DØ. Scalar and vector corrections to b-jet energies were derived for events where a jet originating from a b-quark contains a muon and a neutrino from the direct or cascade decay of the b-quark. Closure tests on the semileptonic correction showed significant improvement in resolution over the basic correction for events with one or two semileptonic decays.

To further improve the energy resolution of the calorimeter for low-momentum charged particles, the implementation of an energy flow algorithm was considered by the experiment. This tracks low-momentum particles through the tracker and into and through the calorimeter, using the tracker momentum measurement as the energy measurement when the tracker resolution is better. As one of the necessary steps towards implementing an eflow algorithm at DØ , an electromagnetic cluster scale was derived using the momenta of low-energy matched-tracks using $J/\Psi \to e^+e^-$ events. The energy of the clusters was shown to be linearly related to the track momenta with no discernible offset between the cluster energies and the track momentum. There were insufficient statistics in either the MC or data samples to detect any variation in the scale with detector η.

Since no η-dependence could be determined, only a scale factor correction could be derived as expected. It is likely that, with larger event samples, a non-linearity in track momentum and a variation with η would be observed, and a more effective correction could be found. It was decided, in 2004, after this study and others conducted by the eflow working group, that it was more important to do a full calibration of the current calorimeter rather than invest further effort straightaway in a full eflow algorithm.

A search for $ZH \to \nu\bar{\nu}b\bar{b}$ events on $55.25pb^{-1}$ of data, collected with the v13 trigger list, was carried out. Improvements in the offline analysis included a Monte Carlo optimisation of the analysis selection criteria and the first use at DØ of the neural net (NN) b-tagging tool. Four different light Higgs masses (105GeV, 115GeV, 125GeV and 135GeV) and the main backgrounds were simulated. The observed 95% C.L. limits are calculated at between 19.3pb and 57.1pb; the expected limit is set between 13.8pb and 40.3pb. While these limits are approximately 2 to 4 times greater than those set in the previous v12 analysis, they are comparable with them and with those set in other analyses, given the relatively small integrated luminosity. This v13 analysis and the v12 analysis are comparable but the improvements in sensitivity through the MC optimisation and the use of the neural net b-tagger in this analysis were compensated for by the use of single b-tagged events in addition to double b-tagged events in the v12 analysis. The use of the neural net b-tagger improved the sensitivity of this study, over that of the v12 analysis, by approximately 30% when used instead of the JLIP b-tagger. The MC optimisation of the selection criteria improved the sensitivity by a further 15%. By comparing the jet multiplicity of the v13 data with the p14 v12 data, it was apparent that discrepancies arose due to problems with the use of the DØ trigger simulation.

6.1 Further work and the future

Considering the future of Higgs searches, success will depend critically on three issues: event yields because the Higgs production cross-sections are small but the backgrounds large, the efficient identification of b-quarks from Higgs decays and the invariant Mass peak of Higgs decay products as the sensitivity depends critically on mass resolution. As the available dataset continues to grow, it will be possible to make continuous improvements to the jet and semileptonic jet energy scales, improving mass resolution, and refinements to this search for the Higgs boson. Although a scalar, muonic semileptonic correction was implemented in JES versions 4.2, 5.1 and 5.3 (p13 and p14 data), there is no semileptonic correction currently available. One will be implemented soon for our enlarged dataset, also with a vector correction may be considered and a correction for electronic semileptonic decays. It was decided, after this study and others conducted by the energy flow working group, that a new, full calibration of the current calorimeter was the priority and the eflow algorithm as I worked on it was discontinued. Rather, a basic version of the eflow algorithm, TrackCal, has now been implemented. The new hadronic calorimeter calibration and TrackCal will both improve dijet mass resolution by about 20% according to initial studies. It has been found, following the Higgs Sensitivity study that, as an approximate rule, an improvement of ±1% in the dijet mass resolution will result in approximately ∓10% improvement in sensitivity [110].

This first look at available v13 data highlighted many issues which will need to be taken into account in the p17 version of the analysis, although data and Monte Carlo are in reasonable agreement. The small data sample meant that the limit set in this analysis adds little to a combined v12/v13 analysis. So given the imminent availability of p17 data, studies are being carried out to understand similar factors in the p17 data, rather than investing further effort in the data set used in this analysis. The approach taken in this analysis underlies the p17 analysis and is therefore good preparation in advance of using the larger dataset, and has demonstrated the potential of the MC optimisation and the neural net b-tagger for increasing the sensitivity of the $ZH \rightarrow \nu\bar{\nu}b\bar{b}$ channel.

DØ is now moving towards using more advanced multivariate analysis techniques, such as neural nets, to make the most of the data by powerfully discriminating against the background processes. The SUSY Higgs workshop [6] highlighted the potential for a neural net analysis of this channel and this analysis, when further developed on p17 data, will form a good standard analysis against which to compare such a technique. There are further improvements in the b-tagging from L0 in the silicon tracker. It is anticipated that the new electromagnetic and hadronic calorimeter calibration in p17 will have a significant effect on the $\not{E}_T$ distributions and some of these conclusions will have to be revised. Further work includes investigating the poor efficiency of the isolated lepton cut further as this only had an efficiency of approximately 30%, and including the single b-tagged events in the MC optimisation.

Looking to the future, the number of published Run II results is increasing pleasingly with 2 papers published in 2004, 27 in 2005 and 14 already published this year, a further 6 accepted for publication and another 10 submitted [111]. The experiment has changed the data format in line with efforts to streamline analyses using a common analysis format. Searches for the Standard Model Higgs boson are well underway in all vector boson associated channels and H→WW and efforts have been combined across the channels.

Recently, results from direct searches at CDF and DØ have been combined. Upper limits have been set on the production cross section of a Standard Model Higgs boson in vector-boson associated production (i.e. the $ZH \rightarrow \nu\nu b\bar{b}$, $WH \rightarrow e\nu b\bar{b}$, $WH \rightarrow \mu\nu b\bar{b}$ and $WH \rightarrow WW^+W^-$ channels) and gluon fusion ($H \rightarrow WW$). The current combined limit from both experiments for all search channels is shown in Figure 6.1 [112]. The observed limit at the Tevatron is currently a factor of 10(4) from the SM cross section at a mass of 115 (160) GeV, although with the expected increases in luminosity and improved analysis techniques (see for example the b-tagging improvements in Chapter 5) this factor will decrease rapidly. Previous studies have shown that $\sim$ 2 fb^{-1} is needed for sensitivity to a SM Higgs of mass $\sim$ 115 GeV [6].

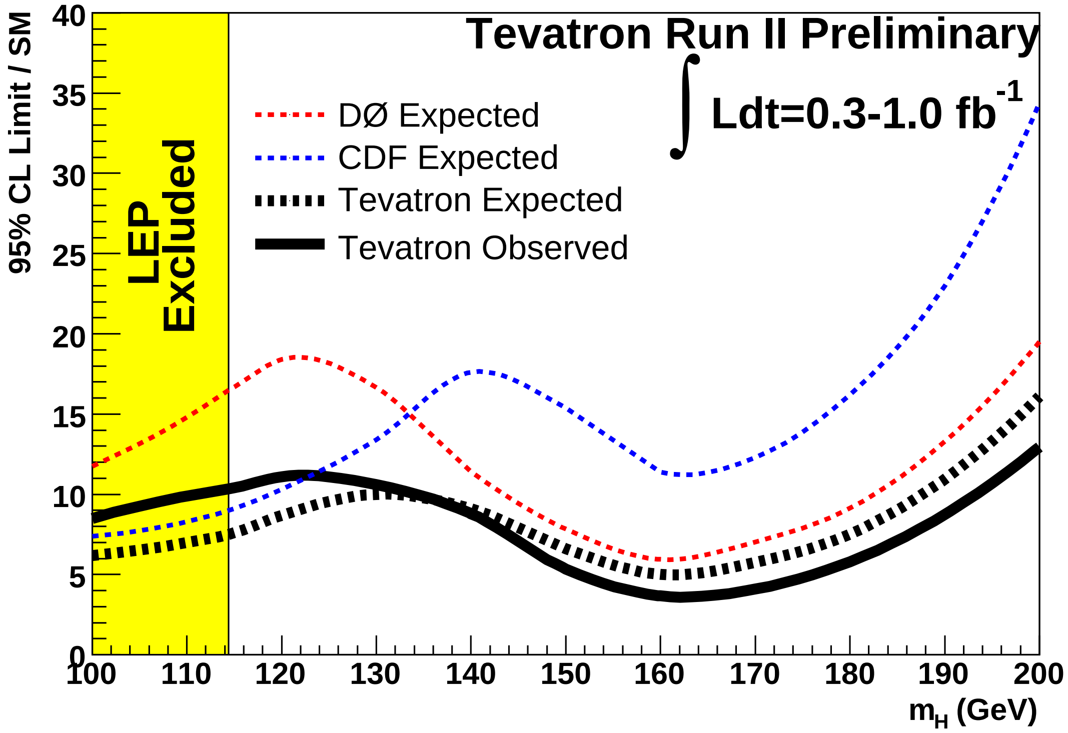

Figure 6.1: The ratio of the expected and observed 95% CL limits to the SM cross section for the combined CDF and DØ analyses.

Appendix A

Binning of Data and Monte Carlo Response in E’

(Z + jets) response binned in E’ for data (CC and EC) and MC (CC).

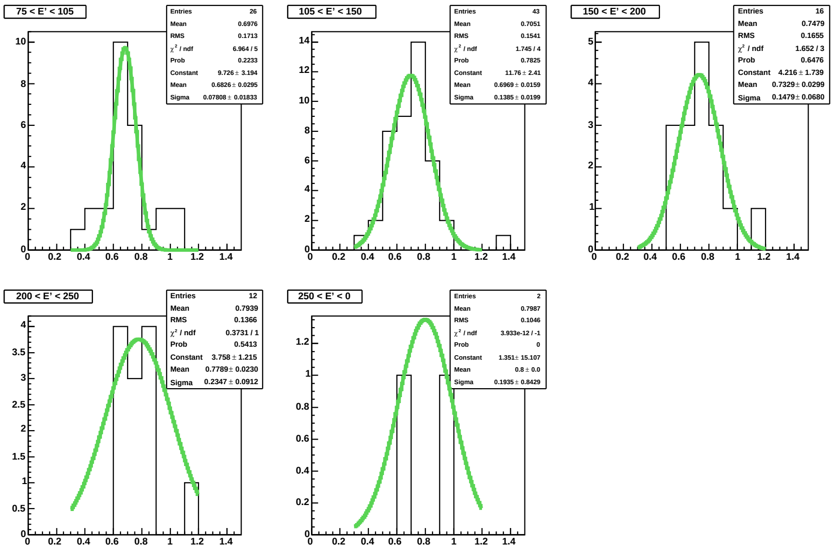

Figure A.1: Data response for the EC, binned in E’

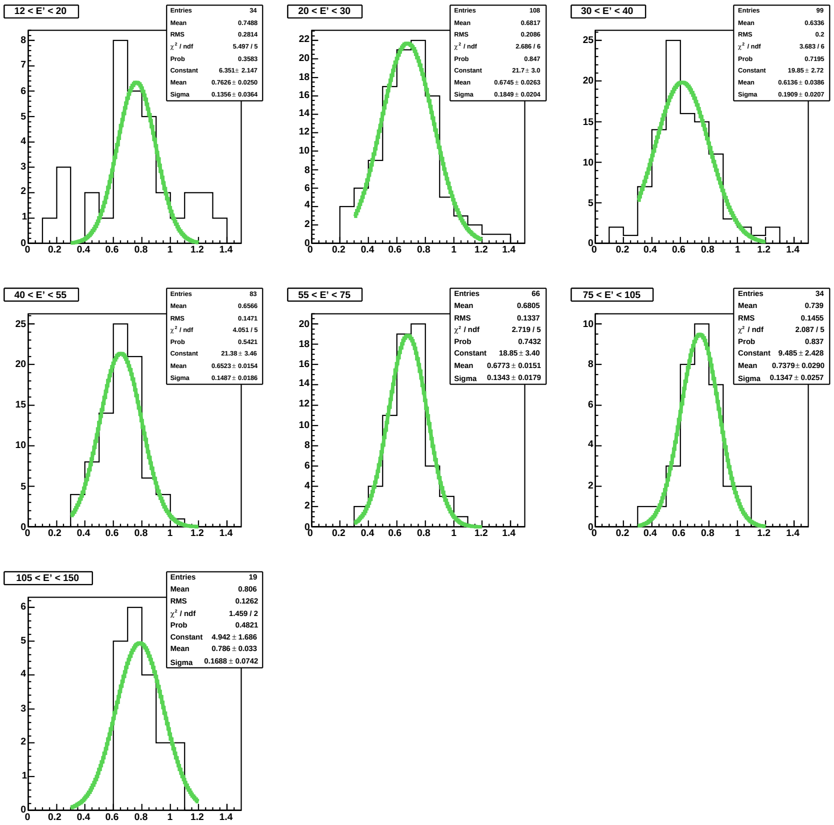

Figure A.2: Data response for the CC, binned in E’

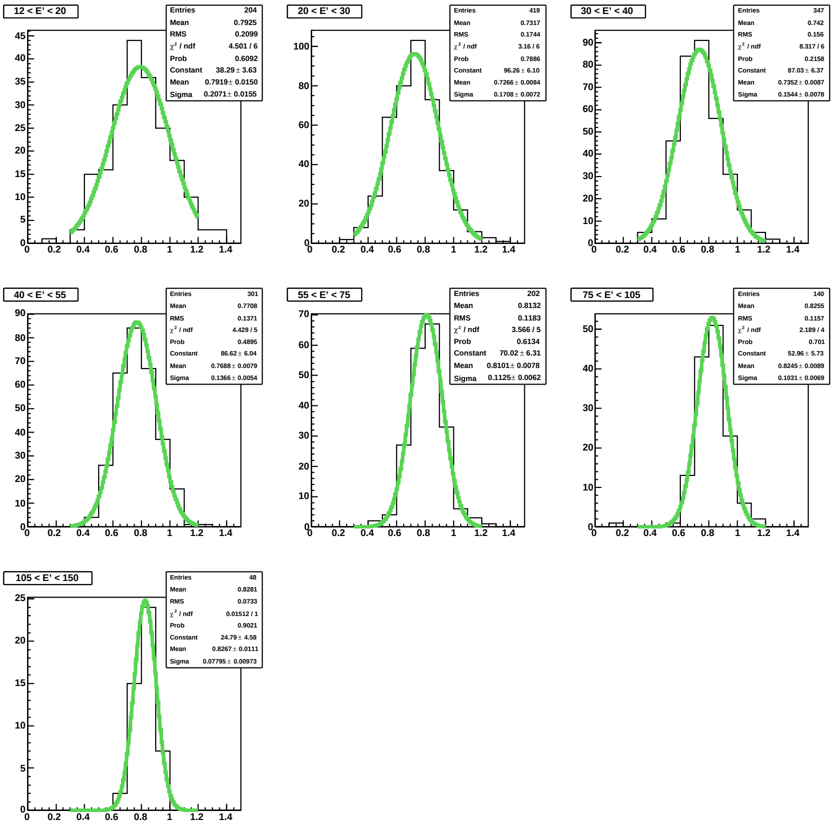

Figure A.3: Monte Carlo response for the CC, binned in E’

Appendix B

Analysis cutflow tables

Cut No.	Selection Criteria	Data %	Total Background	ZH→ $\nu\bar{\nu}b\bar{b}$	ZH→ $e\bar{e}b\bar{b}$	ZH→ $\mu\bar{\mu}b\bar{b}$	ZH→ $\tau\bar{\tau}b\bar{b}$	WH→ $e\nu b\bar{b}$	WH→ $\mu\nu b\bar{b}$
1	Bad Runs	99.97	100	100	100	100	100	100	100
2	Bad Cal/Lbn	99.97	100	100	100	100	100	100	100
3	Trigger	34.89	6.56	47.0	11.1	48.8	27.9	35.8	45.7
4	Jet Requirements	22.09	3.43	35.1	7.9	36.7	23.7	26.3	34.3
5	$\not{E}_T > 20\text{GeV}$	16.13	3.29	35.1	4.7	22.5	22.6	25.8	31.6
6	$H_T < 210\text{GeV}$	15.00	3.07	32.5	4.2	20.0	18.2	24.0	29.5
7	No Isolated tracks	13.25	1.93	29.3	0.1	3.0	8.0	4.9	9.6
9	$min\triangle\phi(\not{E}_T, jet)$	11.16	1.87	28.7	0.1	2.8	6.9	4.6	9.4
10	$\not{E}_T > -40 \times min\Delta\phi(\not{E}_T, jets) + 80$	2.06	1.59	26.6	0.1	2.2	4.6	3.6	7.8
8	$\triangle\phi(dijet) < 165^o$	1.97	1.57	26.4	0.1	2.1	4.5	3.6	7.7
11	$\triangle\phi(\not{E}_T, trk\not{E}_T) < 1.0$	0.72	1.30	24.2	0.0	0.5	2.8	2.9	4.3
12	$0 < Asym(\not{E}_T, trk\not{E}_T) < 0.6$	0.44	1.07	19.6	0.0	0.2	2.1	2.4	2.9
13	$-0.1 < Asym(\not{E}_T, \not{H}_T) < 0.2$	0.10	0.97	18.8	0.0	0.2	1.4	2.2	2.4
14	trk$\not{E}_T > 20\text{GeV}$	0.05	0.88	17.7	0.0	0.1	1.3	2.0	2.3
15	$\lvert trk\not{E}_T - trk\not{E}_T(dijet)\rvert/trk\not{E}_T < 0.2$	0.03	0.66	14.9	0.0	0.0	0.7	1.4	1.5
16	Both jets taggable	0.02	0.37	10.3	0.0	0.0	0.5	1.0	1.1
17	NN tag prob > 0.5	0.00012	0.0033	3.3	0.0	0.0	0.2	0.3	0.4
18	$80\text{GeV} < M_{dijet} < 130\text{GeV}$	0.00007	0.0011	1.8	0.0	0.0	0.0	0.1	0.2

Table B.1: Part I: Selection Cut Efficiencies (%) for the data, MC signal (M_H = 115GeV) and MC backgrounds used in this analysis. The efficiencies are given as percentages of the original number of events before any selection cuts have been applied

Cut No.	Selection Criteria	WH→ $\tau\nu b\bar{b}$	Zbb→ $e\bar{e}b\bar{b}$	Zbb $\mu\nu b\bar{b}$	Zbb→ $\nu\bar{\nu}b\bar{b}$	Zjj→ $e\bar{e}jj$	Zjj→ $\mu\bar{\mu}jj$	Zjj→ $\nu\bar{\nu}jj$	Zjj $\tau\bar{\tau}jj$
1	Bad Runs	100	100	100	100	100	100	100	100
2	Bad Cal/Lbn	100	100	100	100	100	100	100	100
3	Trigger	41.6	1.6	9.9	9.5	1.2	10.2	8.9	7.2
4	Jet Requirements	33.7	0.9	5.4	5.2	0.7	5.1	4.7	4.9
5	$\not\!\!E_T > 20\text{GeV}$	33.4	0.5	3.1	5.2	0.4	2.9	4.7	4.6
6	$H_T < 210\text{GeV}$	29.6	0.4	2.8	4.8	0.3	2.7	4.5	4.2
7	No Isolated tracks	20.3	0.0	0.5	4.3	0.0	0.5	4.2	2.2
9	$min\triangle\phi(\not\!\!E_T, jet)$	19.1	0.0	0.4	4.2	0.0	0.5	4.1	2.0
10	$\not\!\!E_T > -40 \times min\Delta\phi(\not\!\!E_T, jets) + 80$	15.4	0.0	0.3	3.8	0.0	0.4	3.7	1.2
8	$\triangle\phi(dijet) < 165^o$	14.9	0.0	0.3	3.8	0.0	0.4	3.7	1.2
11	$\triangle\phi(\not\!\!E_T, trk\not\!\!E_T) < 1.0$	12.1	0.0	0.1	3.3	0.0	0.1	3.4	0.9
12	$0 < Asym(\not\!\!E_T, trk\not\!\!E_T) < 0.6$	9.4	0.0	0.1	2.7	0.0	0.1	2.8	0.7
13	$-0.1 < Asym(\not\!\!E_T, \not\!\!H_T) < 0.2$	8.5	0.0	0.1	2.6	0.0	0.1	2.6	0.5
14	trk$\not\!\!E_T > 20\text{GeV}$	7.7	0.0	0.0	2.3	0.0	0.0	2.4	0.4
15	$\lvert trk\not\!\!E_T - trk\not\!\!E_T(dijet)\rvert / trk\not\!\!E_T < 0.2$	5.7	0.0	0.0	1.9	0.0	0.0	2.0	0.2
16	Both jets taggable	3.8	0.0	0.0	1.2	0.0	0.0	1.2	0.1
17	NN tag prob > 0.5	1.2	0.0	0.0	0.3	0.0	0.0	0.0	0.0
18	$80\text{GeV} < M_{dijet} < 130\text{GeV}$	0.7	0.0	0.0	0.1	0.0	0.0	0.0	0.0

Table B.2: Part II: Selection Cut Efficiencies (%) for the data, MC signal ($M_H = 115\text{GeV}$) and MC backgrounds used in this analysis. The efficiencies are given as percentages of the original number of events before any selection cuts have been applied

Cut No.	Selection Criteria	Zj→ $\tau t\bar{a}uj$	Wbb→ $e\nu b\bar{b}$	Wbb→ $\mu\nu b\bar{b}$	Wbb→ $\tau\nu b\bar{b}$	Wjj→ $e\nu b\bar{b}$	Wjj→ $\mu\nu b\bar{b}$	Wjj→ $\tau\nu jj$	Wj→ $\tau\nu j$
1	Bad Runs	100	100	100	100	100	100	100	100
2	Bad Cal/Lbn	100	100	100	100	100	100	100	100
3	Trigger	2.8	8.7	4.7	8.9	9.0	8.8	9.7	3.5
4	Jet Requirements	1.4	4.0	2.3	3.9	4.3	4.5	5.8	1.6
5	$\not{E}_T > 20$GeV	1.3	3.9	2.1	3.9	4.2	4.1	5.7	1.6
6	$H_T < 210$GeV	1.3	3.7	2.0	3.6	4.0	3.8	5.4	1.5
7	No Isolated tracks	0.7	0.9	0.7	1.8	1.1	1.4	4.4	1.3
9	$min\triangle\phi(\not{E}_T, jet)$	0.6	0.8	0.7	1.7	1.0	1.4	4.2	1.3
10	$\not{E}_T > -40 \times min\Delta\phi(\not{E}_T, jets) + 80$	0.4	0.7	0.6	1.5	0.9	1.2	3.5	1.1
8	$\triangle\phi(dijet) < 165^o$	0.4	0.7	0.6	1.5	0.9	1.1	3.4	1.1
11	$\triangle\phi(\not{E}_T, trk\not{E}_T) < 1.0$	0.3	0.6	0.4	1.3	0.7	0.8	2.8	0.9
12	$0 < Asym(\not{E}_T, trk\not{E}_T) < 0.6$	0.2	0.4	0.3	1.1	0.6	0.6	2.3	0.8
13	$-0.1 < Asym(\not{E}_T, \not{H}_T) < 0.2$	0.2	0.4	0.2	1.0	0.5	0.5	2.0	0.7
14	trk$\not{E}_T > 20$GeV	0.2	0.4	0.2	0.9	0.5	0.5	1.8	0.6
15	$\lvert trk\not{E}_T - trk\not{E}_T(dijet)\rvert / trk\not{E}_T < 0.2$	0.1	0.3	0.1	0.7	0.3	0.3	1.2	0.5
16	Both jets taggable	0.1	0.2	0.1	0.4	0.2	0.2	0.6	0.3
17	NN tag prob > 0.5	0.0	0.0	0.0	0.1	0.0	0.0	0.0	0.0
18	80GeV $< M_{dijet} <$ 130GeV	0.0	0.0	0.0	0.0	0.0	0.0	0.0	0.0

Table B.3: Part III: Selection Cut Efficiencies (%) for the data, MC signal ($M_H = 115$GeV) and MC backgrounds used in this analysis. The efficiencies are given as percentages of the original number of events before any selection cuts have been applied

Cut No.	Selection Criteria	tt→ $bjjbjj$	tt→ $bl\nu bjj$	tt→ $bl\nu bl\nu$	WZ→ $e\nu b\bar{b}$	WZ→ $l\nu b\bar{b}$	WZ→ $\mu\nu b\bar{b}$	ZZ→ $\nu\bar{\nu}c\bar{c}$	ZZ→ $\nu\bar{\nu}b\bar{b}$
1	Bad Runs	100	100	100	100	100	100	100	100
2	Bad Cal/Lbn	100	100	100	100	100	100	100	100
3	Trigger	14.5	62.2	60.5	25.2	30.4	27.9	8.8	10.0
4	Jet Requirements	14.5	60.9	48.7	15.8	20.3	17.8	4.6	6.4
5	$\not\!\!E_T > 20$GeV	11.7	59.0	47.5	15.5	19.7	16.6	3.9	6.4
6	$H_T < 210$GeV	1.3	28.9	39.3	15.0	19.3	16.1	3.81	6.2
7	No Isolated tracks	1.0	10.9	7.4	3.5	9.0	5.4	3.6	5.6
9	$min\triangle\phi(\not\!\!E_T, jet)$	0.7	10.0	7.1	3.3	8.7	5.2	3.4	5.4
10	$\not\!\!E_T > -40 \times min\Delta\phi(\not\!\!E_T, jets) + 80$	0.2	8.1	6.5	2.7	7.4	4.5	2.6	4.9
8	$\triangle\phi(dijet) < 165^o$	0.2	7.8	6.3	2.6	7.3	4.5	2.5	4.9
11	$\triangle\phi(\not\!\!E_T, trk\not\!\!E_T) < 1.0$	0.1	5.9	4.9	2.2	5.7	2.8	2.2	4.4
12	$0 < Asym(\not\!\!E_T, trk\not\!\!E_T) < 0.6$	0.0	4.8	3.9	1.8	4.6	2.2	1.8	3.2
13	$-0.1 < Asym(\not\!\!E_T, \not\!\!H_T) < 0.2$	0.0	3.8	3.3	1.5	4.1	1.9	1.6	3.0
14	trk$\not\!\!E_T > 20$GeV	0.0	3.7	3.2	1.4	3.7	1.8	1.4	2.8
15	$\|trk\not\!\!E_T - trk\not\!\!E_T(dijet)\|/trk\not\!\!E_T < 0.2$	0.0	1.9	2.0	0.9	2.7	1.3	1.4	2.4
16	Both jets taggable	0.0	1.4	1.3	0.7	1.7	0.8	0.8	1.5
17	NN tag prob > 0.5	0.0	0.1	0.4	0.2	0.1	0.2	0.3	0.5
18	80GeV $< M_{dijet} <$ 130GeV	0.0	0.0	0.1	0.1	0.1	0.1	0.2	0.3

Table B.4: Part IV: Selection Cut Efficiencies (%) for the data, MC signal ($M_H = 115$GeV) and MC backgrounds used in this analysis. The efficiencies are given as percentages of the original number of events before any selection cuts have been applied

Appendix C

Event Display Plots

The following figures in this Appendix are event display plots for $ZH \rightarrow \nu\bar{\nu}b\bar{b}$ candidate events. On the left in each plot, is shown the calorimeter transverse energy in the $\eta - \phi$ plane. On the right in each plot, is shown the calorimeter and tracking view, as a projection in the $x - y$ plane at $z = 0$.

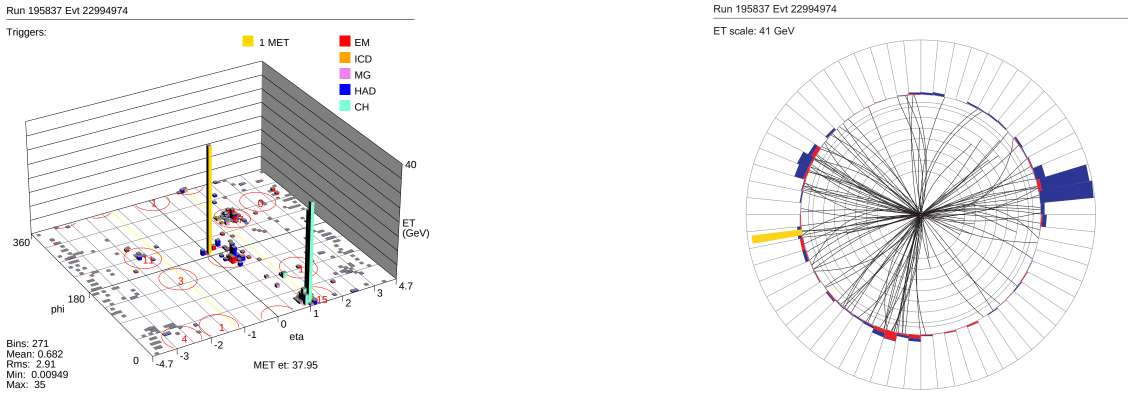

Figure C.1: Data event display of a ZH event candidate that passes all selection cuts. Run number = 195837, event number = 22994974

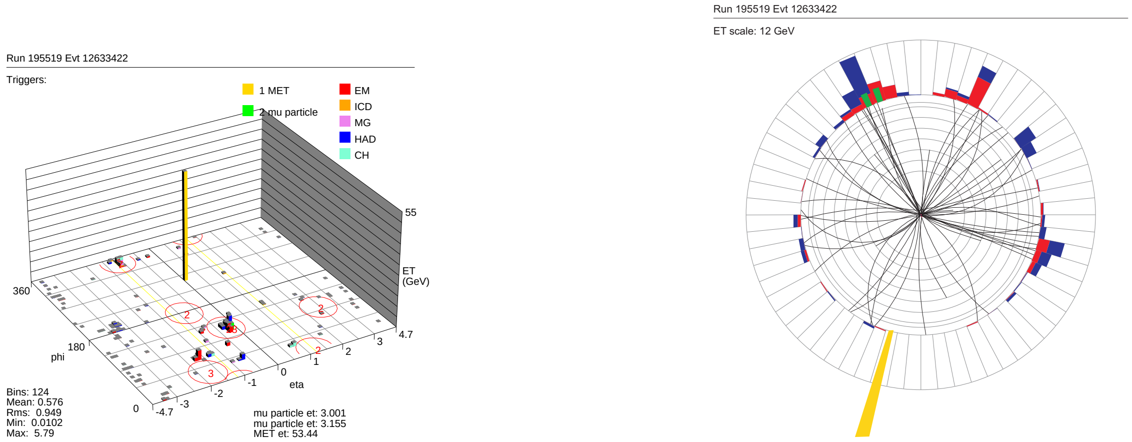

Figure C.2: Data event display of a ZH event candidate that passes all selection cuts. Run number = 195519, event number = 12633422

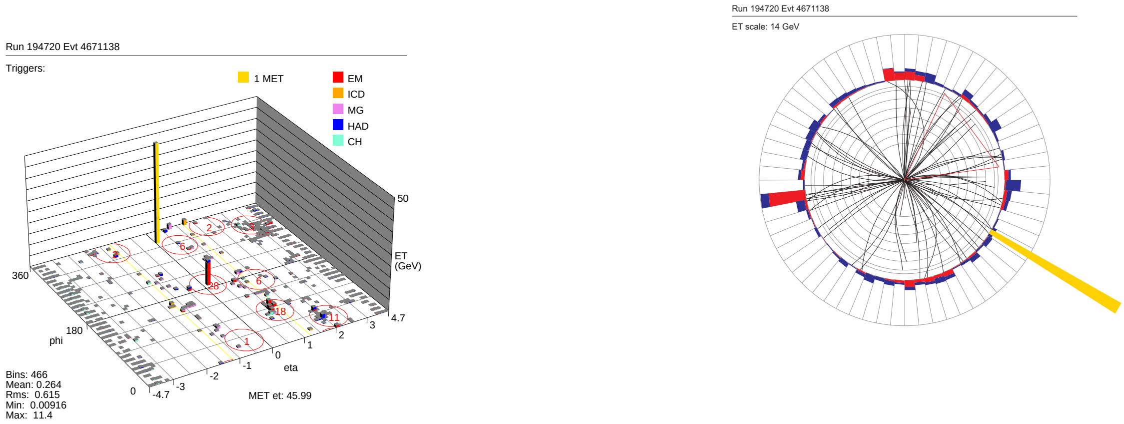

Figure C.3: Data event display of a ZH event candidate that passes all selection cuts. Run number = 194720, event number = 4671138

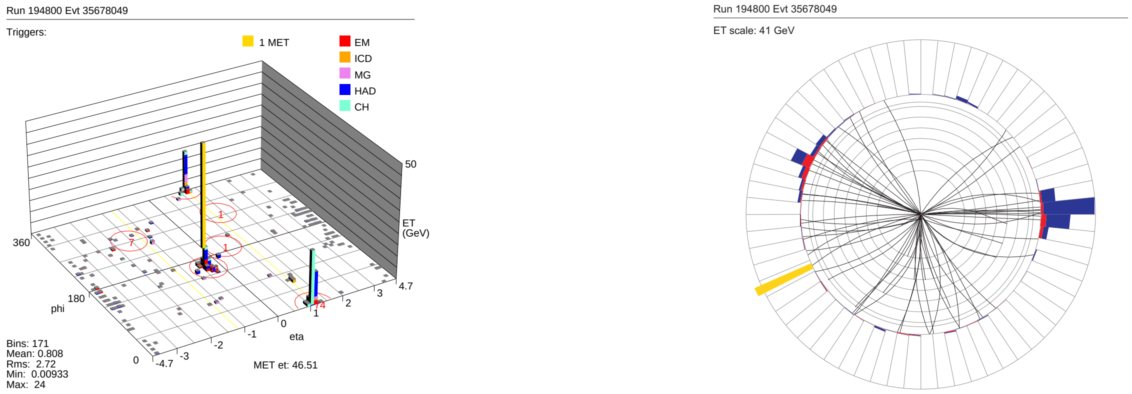

Figure C.4: Data event display of a ZH event candidate that passes all selection cuts. Run number = 194800, event number = 35678049

Bibliography

[1] I.Brock. The Higgs Potential. `http://www-zeus.physik.uni-bonn.de/~brock/feynman/vtp_ws0506/chapter09/higgs_pot.jpg`.

[2] K. Riesselmann. Limitations of a Standard Model Higgs Boson. *hep-ph/9711456*, 1997.

[3] ALEPH Collaboration, DELPHI Collaboration, L3 Collaboration and OPAL Collaboration, The SLD Collaboration, The LEP Electroweak Working Group, The SLD Electroweak and Heavy Flavour Groups. Precision electroweak measurements on the Z Resonance. *hep-ex/0509008*, 2006.

[4] The DØ Collaboration. Run II Luminosity. `http://www-d0.fnal.gov/runcoor/RUN/run2_lumi.html`.

[5] A. Goussiou *et al.* Jet Energy Scale and Resolution, v4.2. *DØ Note 4115*, 2003.

[6] The CDF and DØ Collaborations. Results of the Tevatron Higgs Sensitivity Study. *FERMILAB-PUB-03/320-E*, 2003.

[7] M. Spira. Higgs Boson Production and Decay at the Tevatron. *hep-ph/9810289*, 1998.

[8] W. M. Yao *et al.* The Review of Particle Physics. *Journal of Physics*, G 33, 1, 2006.

[9] A. Askew. Parametrising the Local Muon Resolution in p13. *DØ note 4314*, 2003.

[10] T. Scanlon and M. Anastasoaie *et al.* Development and Optimisation on Monte Carlo of a Neural Network Tool to Identify b-jets. *DØ note 4889*, 4889.

[11] Particle Data Group. A History of Particle Physics. `http://particleadventure.org/particleadventure/other/history/index.html`.

[12] D. Griffiths. *Introduction to Elementary Particles.* John Wiley and Sons, Inc., 1987.

[13] F. Halzen and A. Martin. *Quarks and Leptons: An Introductory Course in Modern Particle Physics.* John Wiley and Sons, Inc., 1984.

[14] Emmy Noether. Preface. *Mathematischer Annalen*, 96:26–11, 1927.

[15] C. Yang and R. Mills. Conservation of Isotopic Spin and Isotopic Gauge Invariance. *Phys. Rev.*, 96(1):191–195, Oct 1954.

[16] S. Glashow. Partial Symmetries of Weak Interactions. *Nucl. Phys.*, 22:579–588, 1961.

[17] A. Salam. Weak and Electromagnetic Interactions. *Svartholm: Elementary Particle Theory, Proceedings of the Nobel Symposium 1968*, 1968.

[18] S. Weinberg. A Model of Leptons. *Phys. Rev. Lett.*, 19(21):1264–1266, Nov 1967.

[19] The Super Kamiokande Collaboration. Evidence for the Oscillation of Atmospheric Neutrinos. *Phys. Rev. Lett. 81*, pages 1562–1567, 1998.

[20] The Super Kamiokande Collaboration. Determination of Solar Neutrino Oscillation Parameters using 1496 Days of Super Kamiokande I Data. *Phys. Lett. B539*, pages 179–187, 2002.

[21] N. Arkani-Hamed *et al.* The Hierarchy Problem and Dew Dimensions at a Millimeter Scale. *Phys. Lett.*, B429:263–272, 1998.

[22] P. Higgs. Broken Symmetries and the Masses of Gauge Bosons. *Phys. Rev. Lett.*, 13(16):508–509, Oct 1964.

[23] P. Higgs. Spontaneous Symmetry Breakdown without Massless Bosons. *Phys. Rev.*, 145(4):1156–1163, May 1966.

[24] C. Lai. *Gauge Theory of Weak and Electromagnetic Interactions. Selected Papers.* World Scientfic, 1981.

[25] B. Lee *et al.* Weak Interactions at Very High Energies: The Role of the Higgs Boson Bass. *Phys. Rev. D*, 16(5):1519–1531, Sep 1977.

[26] ALEPH Collaboration, DELPHI Collaboration, L3 Collaboration, OPAL Collaboration. Search for the Standard Model Higgs Boson at LEP. *Physics Letters B*, 565:61, 2003.

[27] M. Kruse *et al.* Combined Standard Model VH Production Cross Section Limits for Run I CDF. *CDF Note 4985*, 1999.

[28] The DØ Collaboration. Description of Original DØ Detector. *Nucl Instrum. Methods Phys. Res. A*, pages 338–185, 1994.

[29] The DØ Collaboration. Observation of the Top Quark. *Phys. Rev. Lett.*, 74(14):2632–2637, Apr 1995.

[30] The DØ Collaboration. Direct Measurement of the Top Quark Mass. *Phys. Rev. Lett.*, 79(7):1197–1202, Aug 1997.

[31] The DØ Collaboration. A Precision Measurement of the Mass of the Top Quark. *Nature*, 429:638–642, Jun 2004.

[32] The DØ Collaboration. The Upgraded DØ Detector. *Nucl.Instrum.Meth.*, A565:463–537, 2006.

[33] The DØ Collaboration. Run IIb Upgrade Technical Design Report. *http://d0server1.fnal.gov/projects/run2b/Silicon/www/smt2b/Documentation/documentation.html*, September 2002.

[34] T. Cole *et al.* Design Report, Superconducting Accelerator. Technical Report Beams-doc-1888-v1, Fermilab, 1979.

[35] R. Moore. An Overview of Tevatron Collider Run II at Fermilab. Technical Report Beams-doc-190-v1, Fermilab, Dec 2002.

[36] X. Hailey. Production of Negative Hydrogen Ions. `http://sist.fnal.gov/archive/2003/Hailey/Paper.pdf`.

[37] Wikipedia. Stochastic cooling. `http://en.wikipedia.org/wiki/Stochastic_cooling`, 2006.

[38] D. Adams *et al.* First Large Sample Study of Visible Light Photon Counters (VLPC's). `http://d0server1.fnal.gov/users/stefan/www/como94/como.html`.

[39] The DØ Collaboration. Beam Tests of the DØ Uranium Liquid Argon End Calorimeters. *DØ Note 1434*, 1992.

[40] The DØ Collaboration. The Muon System of the Run II DØ Detector. *Nuclear Instruments and Methods in Physics Research A*, 552 (2005) 372-398, 2005.

[41] Definitions. `http://www.fnal.gov/pub/now/definitions/`.

[42] T. Edwards *et al.* Determination of the Effective Inelastic $p\overline{p}$ Cross-section for the DØ Run II Luminosity Measurement. *Fermilab-TM-2278-E*, 2004.

[43] T. Andeen *et al.* The Upgraded Luminosity Detector Readout and Studies of the New Effective Inelastic Cross-section. *DØ Note 4904*, 2005.

[44] S. Klimenko *et al.* Averaging of the Inelastic Cross-sections Measured by the CDF and the E811 Experiments. *Fermilab*, 2004. FERMILAB-FN-0741.

[45] B. Casey *et al.* Determination of the Effective Inelastic $p\overline{p}$ Cross-section for the DØ Luminosity Measurement Using Upgraded Readout Electronics. *DØ Note 4958*, 2005.

[46] G. Steinbrück. *Measurement of the Angular Distribution of Electrons from W Boson Decays at DØ* . PhD thesis, University of Oklahoma, 1999.

[47] V. Buescher and J. Zhu. EM Certification Tools. *DØ Note 4171*, 2003.

[48] The DØ Collaboration. Top Quark Search with the DØ 1992 to 1993 Data Sample. *Phys. Rev. D*, 52(9):4877–4919, Nov 1995.

[49] The EM ID Working Group. DØ EM ID Certification. `http://www-d0.fnal.gov/phys_id/emid/d0_private/certification/main_v5_0.html`.

[50] J. Gardner *et al.* Electron Likelihood in p14. *DØ Note 4449*, 2004.

[51] C. Clement *et al.* Muon ID Certification for p14. *DØ Note 4350*, 2004.

[52] E. Busato and B. Andrieu. Jet Algorithms in the DØ Run II Software: Description and User's Guide. *DØ Note 4457*, 2004.

[53] G. Blazey *et al.* Run II Jet Physics. *Proc. of the QCD and Weak Boson Physics in Run II Workshop*, 1999.

[54] N. Hadley. Cone Algorithm for Jet Finding. *DØ Note 0904*, 1989.

[55] The Top Physics Working Group of the DØ Collaboration. DØ Top Analysis and Data Sample for the Winter Conference 2004. *DØ Note 4419*, 2004.

[56] B. Olivier *et al.* The Missing Transverse Energy Resolution of an Event. *DØ Note 3629*, 1999.

[57] The DØ Tracking Working Group. Tracking Efficiency Overview. Technical report, DØ Collaboration, 2006.

[58] H. Greenlee. Motion of a Charged Particle in a Magnetic Field. *DØ Note 4180*, 2003.

[59] D. Adams. Finding Tracks. *DØ Note 2958-2*, 1996.

[60] G. Hesketh. Central Track Extrapolation through the DØ Detector. *DØ Note 4079*, 2003.

[61] G. Borissov. Technical Details of AA Tracking. Talk presented at the DØ Workshop, December 2005.

[62] The Tracking Working Group. Performance of p14 Tracking. `http://www-d0.fnal.gov/global_tracking/results/p14.00.00_index.html`.

[63] The B-ID Working Group. Secondary Vertex Tagger. `http://www-d0.fnal.gov/phys_id/bid/d0_private/certification/p14/secvertex/secvertex_v2.html`.

[64] L. Feligioni *et al.* Update on b-quark Jet Identification with Secondary Vertex Reconstruction using d0reco p14. *DØ Note 4414*, 2004.

[65] The DØ Collaboration. Run II Software Algorithms. `http://www-d0.fnal.gov/computing/algorithms/`.

[66] The Common Samples Group. d0correct. `http://www-d0.fnal.gov/Run2Physics/cs/d0correct/d0correct.html`.

[67] S. Protopopescu *et al.* ThumbNail: a Compact Data Format. *DØ Note 3979*, 2002.

[68] The DØ Collaboration. Trigger webpages. `http://www-d0.fnal.gov/detector/trigger.html`.

[69] The DØ Top Physics Working Group. Public results. `http://www-d0.fnal.gov/Run2Physics/top/top_public_web_pages/top_public.html`.

[70] The Jet Energy Scale Working Group. Certified Jet Energy Scale. `http://www-d0.fnal.gov/phys_id/jes/d0_private/certified/certified_jes.html`.

[71] B. Abbott *et al.* Determination of the Absolute Jet Energy Scale in the DØ Calorimeters. *hep-ex/9805009*, 1998.

[72] The Jet Energy Scale Working Group. The Jetcorr Software Package. `http://www-d0.fnal.gov/d0dist/dist/packages/jetcorr/`.

[73] The DØ Collaboration. Run II Reconstruction Status. `http://www-d0.fnal.gov/computing/algorithms/status/p14.html`.

[74] T. Sjstrand *et al.* PYTHIA 6.3 Physics and Manual. *hep-ph/0308153*, 2003.

[75] The Electromagnetic Object Identification Working Group. EM Identification. `http://www-d0.fnal.gov/phys_id/emid/d0_private/emid.html`.

[76] The Jet Identification Working Group. Jet Identification. `http://www-d0.fnal.gov/phys_id/jets/jetid.html`.

[77] L. Duflot and M. Ridel. An Energy Flow Algorithm for DØ . *DØ Note 3927*, 2002.

[78] M. Petteni *et al.* Energy Correction for Semileptonic Decays of b-jets, using p13. *DØ Note 4248*, 2003.

[79] K. Hanagaki and J. Kasper. Identification of b-jet by Soft Muon Tagging. *DØ Note 4867*, 2005.

[80] The ALEPH Collaboration. Performance of the ALEPH detector at LEP. *Nuclear Instruments and Methods in Physics*, A360(3):481–506, June 1995.

[81] L. Dulfot and M. Ridel. The CellNN Algorithm: Cell Level Clustering in the DØ Calorimeter. *DØ Note 3923*, 2001.

[82] F. Beaudette and J.-F. Grivaz. The Road Method (an Algorithm for the Identification of Electrons in Jets). *DØ Note 3976*, April 11, 2002.

[83] F. Beaudette and J.-F. Grivaz. Electron Identification and b-tagging with the Road Method. *DØ Note 4032*, October 3, 2002.

[84] The Electromagnetic Object Identification Working Group. EMRECO: EM ID Vertical Review.

[85] The Electromagnetic Object Identification Working Group. EM Particle Documentation.

[86] M. Cwiok and A. Haas. Run II η-Intercalibration of the Hadronic Calorimeter. *DØ Note 5006*, 2006.

[87] J. Kvita and K.Peters. Run II ϕ-Intercalibration of the Fine Hadronic Calorimeter. *DØ Note 5005*, 2006.

[88] P. Mal. Energy Flow Status: Single Pion Response, Track-Calorimeter Jets. DØ Calorimeter Workshop, April 2006.

[89] M. Carena *et al.* Report of the Tevatron Higgs Working Group. *hep-ph/0010338*, 2000.

[90] M. Tomoto. A Search for SM Higgs Boson using the $zh \rightarrow \nu\overline{\nu}b\bar{b}$ Channel in $p\overline{p}$ Collisions at $\sqrt{(s)} = 1.96$TeV. *DØ Note 4744*, 2005.

[91] The Common Samples Working Group. p14 Data Reprocessing Pages. `http://www-d0.fnal.gov/Run2Physics/cs/skimming/pass2.html`.

[92] The Common Samples Working Group. Thumbnail Fixing. `http://www-d0.fnal.gov/Run2Physics/cs/fixing/fixing.html`.

[93] M. Mangano *et al.* Alpgen, a generator for hard multiparton processes in hadronic collisions. *hep-ph/0206293*, 2003.

[94] J. Campbell and R. Ellis. MCFM: A Monte Carlo for Femtobarn processes at Hadron Colliders. `http://mcfm.fnal.gov`.

[95] A. Duperrin *et al.* The v13 Physics Trigger List and New Phenomena Triggers. *DØ Note 4641*, 2004.

[96] The DØ Collaboration. Certified Jet Energy Scale v5.3. `http://www-d0.fnal.gov/phys_id/jes/d0_private/certified/v5.3/links.html`.

[97] C. Gerber *et al.* Taggability in p14 Pass 2 Data. *DØ Note 4995*, 2006.

[98] T. Scanlon *et al.* Certification of the Neural Network b-tagging Tool on Pass 2 Data. *DØ Note 4890*, 2005.

[99] D. Bloch *et al.* Performance of the JLIP b-tagger in p14. *DØ Note 4348*, 2004.

[100] B-ID Certification Group. DØ Secondary Vertex Tag Certification. `http://www-d0.fnal.gov/phys_id/bid/d0_private/certification/p14/secvertex/secvertex_v1.html`.

[101] B-ID Certification Group. The Counting Signed Impact Paramter Tagging Method. `http://www-d0.fnal.gov/phys_id/bid/d0_private/certification/p14/CSIP/CSIP_v2.html`.

[102] F. James. MINUIT, Function Minimization and Error Analysis, Reference Manual. *CERN Program Library Long Writeup D506, Version 94.1*, 2000.

[103] M. Agelou *et al.* 0.5 and 0.7 Jet p_T Resolution using JES v5.3. *DØ Note 4775*, 2005.

[104] I. Bertram *et al.* A Recipe for the Construction of Confidence Limits. *DØ Note 2775*, 1995.

[105] J. Hobbs. Bayesian Limit Calculator Web Interface. `http://www-d0.fnal.gov/hobbs/limitcalc.html`.

[106] The DØ Collaboration. A Search for $wb\bar{b}$ and wh Production in $p\bar{p}$ Collisions at $\sqrt{s} = 1.96$TeV. *hep-ex/0410062*, 2004.

[107] H. Dong and J. Hobbs. Search for SM Higgs Boson in $zh \rightarrow \mu\bar{\mu}b\bar{b}$ Channel $p\bar{p}$ Collisions at $\sqrt{s} = 1.96$TeV. *DØ Note 5107*, 2006.

[108] V. Veszpremi *et al.* Search for the SM Higgs Boson in the $\not{E}_T$ +b-jets Final State with 0.973fb^{-1} Run II data at CDF. *CDF Note CDF8442*, 2006.

[109] Y. Kusakabe *et al.* Search for Standard Model Higgs Boson Production in Association with W Boson at CDF with 1fb^{-1}. *CDF Note CDF8390*, 2006.

[110] Wade Fisher, On behalf of the Tevatron Higgs Sensitivity Group. Tevatron higgs sensitivity. Conference Proceedings, 2004.

[111] The DØ Collaboration. DØ Run II Publications. `http://www-d0.fnal.gov/www_buffer/pub/Run2_publications.html`.

[112] G. Bernardi *et al.* Limits on Standard Model Higgs Boson Production. *DØ Note 5056*, 2006.

“The traveller has reached the end of the journey!”

The Dhammapada, Buddha